学位論文(要約)

A numerical study of pyroclastic density currents by a two-layer shallow-water model

(二層浅水波モデルに基づく火砕流ダイナミクスの数値的研究)

平成29年12月博士(理学)申請

東京大学大学院理学系研究科

地球惑星科学専攻

志水　宏行

Abstract

During an explosive volcanic eruption, a hot mixture of volcanic particles and gas is continuously ejected from the volcanic vent and develops an eruption column. When the density of the mixture remains higher than that of the ambient air, the eruption column collapses to produce pyroclastic density currents (PDCs). PDCs are characterized by strong density stratification, whereby a dilute current (particle concentrations $\lesssim 1$ vol.%) overrides the dense basal current (particle concentrations ~ 10 vol.%). Each part is controlled by different physical processes due to the difference in the particle volume fraction: the dilute current is affected by air entrainment, thermal expansion of entrained air, frontal resistance of ambient air, and particle settling; the dense current is affected by particle supply from the dilute current, basal friction, and sedimentation. The relative magnitude of the effects of these physical processes depends on source conditions (e.g., mass eruption rate and temperature of erupted materials). As a result of these factors, the deposits of PDCs are extremely variable in distribution and lithofacies. There is a vast amount of field-based works related with the diversity of PDC deposits and experimental-analogue studies related with the physical processes underlying PDC dynamics. We aim to relate the underlying physical processes with the diversity of PDC deposits, by using numerical simulations.

The essential behavior of PDCs can be described by the depth-averaged shallow-water equations. In order to assess the effects of the above physical processes on PDC dynamics and the resulting PDC deposits, we have developed a new two-layer shallow-water model. Because the dilute layer is affected by strong density variation due to thermal expansion of entrained air and particle settling, it is simulated by solving six basic equations: particle mass, entrained air mass, bulk mass, momentum and energy conservation equations, and the equation of state. Because the basal dense layer is affected by the mass and momentum transfer processes due to basal friction, sedimentation and the particle supply from the dilute layer, it is simulated by solving two basic equations: mass and momentum conservation equations. These conservation equations are numerically solved by the finite volume method using the HLL scheme.

We calculated time evolution of two-layer PDCs generated by dilute mixtures from the collapsing column at a constant mass eruption rate. The dilute current, generated from the collapsing column, produces the basal dense current, and a deposit aggrades upward from the base. When the frontal region of the dilute current becomes lighter than ambient air to reverse buoyancy and liftoff, the front of the dilute current does not propagate further. When the mass flux of the dense current and the deposition rate at the base balance at the frontal region, the front of the dense current does not propagate further. Finally, each

layer converges to a steady state. We performed a parametric study by varying the mass eruption rates at source, $\dot{M}_0$, from 10^3 to 10^{11} kg/s, the temperature of erupted material, $T_{\rm in}$, from 300 to 1200 K, the particle settling velocity at the base of the dilute current, $W_{\rm s}$, from 0.3 to 3.0 m/s, and the deposition rate at the base of the dense current, D, from 3.0×10^{-5} to 3.0×10^{-2} m/s. As a result, on the basis of the runout disntances of the dilute and dense currents, the steady behaviors of the two-layer PDCs are classified into three flow regimes: Regime 1, Regime 2a, and Regime 2b. In Regime 1, the dense current does not develop, and the dilute current directly forms its deposits. In Regime 2a, the dense current develops, but the steady runout distance of the dilute current is longer than that of the dense current. In Regime 2b, the dense current develops, and the steady runout distance of the dense current is longer than that of the dilute current.

In order to systematically understand mechanisms that make the above classification possible, we have investigated the steady runout distances of the dilute and dense currents by the following three steps. First, we have investigated the basic equations to identify governing dimensionless parameters that control the steady runout distances (Step 1). Secondly, we have derived analytical solutions under the condition where air entrainment is not taken into account (Step 2). Finally, we have evaluated the effects of air entrainment on the steady runout distances on the basis of numerical simulations (Step 3).

In Step 1, as a result of the non-dimensionalization, we have identified four governing dimensionless parameters: $W_{\rm s}/(\mathcal{U}a_0)$, $D/W_{\rm s}$, $E|\bar{u}|/W_{\rm s}$, and $(C_{\rm pa}T_{\rm a})/(C_{\rm p0}T_0)$. The parameter $W_{\rm s}/\mathcal{U}$ represents the ratio of the particle settling velocity at the base of the dilute current to the horizontal velocity scale of the two-layer PDC. The velocity scale $\mathcal{U}$ depends on the mass eruption rate at source $\dot{M}_0$ (i.e., $\mathcal{U} \propto \dot{M}_0^{1/5}$). The parameter a_0 is the aspect ratio of the height scale of the dilute current to the length (or radius) of the collapsing column, which is imposed on a boundary condition. The parameter $D/W_{\rm s}$ represents the relative magnitude of the effect of deposition from the base of the dense current to that of particle supply from the dilute current. The parameter $E|\bar{u}|/W_{\rm s}$ represents the relative magnitude of the effect of air entrainment to that of particle settling. Here, $E|\bar{u}|$ is the entrainment velocity, where $\bar{u}$ is the local flow velocity and E is the entrainment coefficient. The parameter $(C_{\rm pa}T_{\rm a})/(C_{\rm p0}T_0)$, defined as the ratio of the enthalpy of the entrained air to the enthalpy scale of the dilute current, represents the degree of thermal expansion of air entrained into the dilute current, where $C_{\rm pa}$ and $C_{\rm p0}$ are the heat capacities at constant pressure of air and the dilute current at the collapsing column edge, respectively, and $T_{\rm a}$ and T_0 is the temperatures of ambient air and the dilute current at the collapsing column edge, respectively.

In Step 2, we have derived the analytical solution of the steady runout distances from the mass conservation equations of the two-layer PDCs for the case without air entrainment to understand the theoretical framework of the regime transition. The analytical solution shows that the steady runout distances of the dilute and dense currents primarily depend on the parameter $W_{\rm s}/(\mathcal{U}a_0)$, which in turn depends on the mass eruption rate at source $\dot{M}_0$. The analytical solution also suggests that the boundaries of regimes (i.e., Regimes 1, 2a and 2b) are mainly determined by the parameter $D/W_{\rm s}$, which is independent of the mass eruption rate at source $\dot{M}_0$.

In Step 3, we have compared the analytical solution derived in Step 2 with numerical results of the two-layer model where the effects of air entrainment are taken into consid-

eration. The numerical results show that the parameter $E|\bar{u}|/W_{\rm s}$ is mainly determined by the parameter $W_{\rm s}/\mathcal{U}$. Thus, the runout distance of the two-layer PDCs is strongly affected by air entrainment in the case of small $W_{\rm s}/(\mathcal{U}a_0)$ (i.e., large $\dot{M}_0$), whereas the effect of air entrainment is limited in the case of large $W_{\rm s}/(\mathcal{U}a_0)$ (i.e., small $\dot{M}_0$).

The numerical results show that the effects of thermal expansion of entrained air on the steady runout distances strongly depend on the parameter $(C_{\rm pa}T_{\rm a})/(C_{\rm p0}T_0)$. When the temperature of erupted material is high (i.e., small $(C_{\rm pa}T_{\rm a})/(C_{\rm p0}T_0)$), a large degree of thermal expansion of entrained air significantly enhance the liftoff; as a result, the steady runout distance of the dilute current decreases as the degree of air entrainment increases. In this case, the steady runout distance of the dense current also decreases because thermal expansion of entrained air leads to decreasing of the particle supply from the dilute current to the dense current. When the temperature of erupted material is low (i.e., large $(C_{\rm pa}T_{\rm a})/(C_{\rm p0}T_0)$), on the other hand, the entrainment of air results in thickening of the dilute current without enhancing liftoff; as a result, the steady runout distance does not decrease or can even increase as the degree of entrainment increases. Because thickening of the dilute current also leads to decreasing the particle settling from the dilute current to the dense current, the steady runout distance of the dense current decreases as the degree of entrainment increases for the large $(C_{\rm pa}T_{\rm a})/(C_{\rm p0}T_0)$ case, too.

The present results account for diverse features of PDC deposits (e.g., distributions and sedimentary structures). A wide range of distributions of PDC deposits can be accounted for by variable runout distances of PDCs, depending on the mass eruption rate at source, $\dot{M}_0$. Generally, a wide variety of sedimentary structures of PDC deposits (e.g., massive and/or stratified lithofacies) result from the flow-particle interaction inside the boundary layer at the bottom of PDCs. It is considered that some of the diversities of PDC deposits are explained by the difference in the flow-particle interaction in the bottom boundary layer between the dilute and dense currents. When stratified lithofacies are dominantly observed from proximal to distal areas, the PDC deposits are interpreted to be emplaced by PDCs of Regime 1. When massive lithofacies are dominantly observed from proximal to distal areas, the PDC deposits are interpreted to be emplaced by PDCs of Regime 2b. When distal lithofacies change from massive to stratified, the PDC deposits are interpreted to be emplaced by PDCs of Regime 2a. Our results that the region of Regime 2a expands in the regime diagram as the temperature of erupted material decreases are consistent with the observation that stratified surge deposits are commonly observed in the deposits of phreatomagmatic eruptions.

Contents

Chapter 1

Introduction

During an explosive volcanic eruption, a hot mixture of volcanic particles and gas is continuously ejected from the volcanic vent and develops an eruption column. When the density of the mixture remains higher than that of the ambient air, the eruption column collapses to produce pyroclastic density currents (PDCs; Figure 1.1a and b; e.g., Sparks et al., 1997). PDCs deposit an extremely diverse range of pyroclastic deposits (Fisher & Schmincke, 1984; Cas & Wright, 1987; Druitt, 1998; Branney & Kokelaar, 2002; Sulpizio et al., 2014; Brown & Andrews, 2015; Figure 1.1c and d). In this thesis, we develop a new two-layer shallow-water model for PDCs, and discuss the dynamics of PDCs and the diversity of their deposits on the basis of the new model. Although PDCs also originate from laterally inclined blasts or lava-dome collapses (e.g., Branney & Kokelaar, 2002), we focus on the PDCs generated by collapse of an eruption column.

In this chapter, we briefly summarize the outline of the diversity of the deposits of PDCs and the physical process on the PDCs (particularly the significance of vertical density stratification) to elucidate the whole view of the present problem.

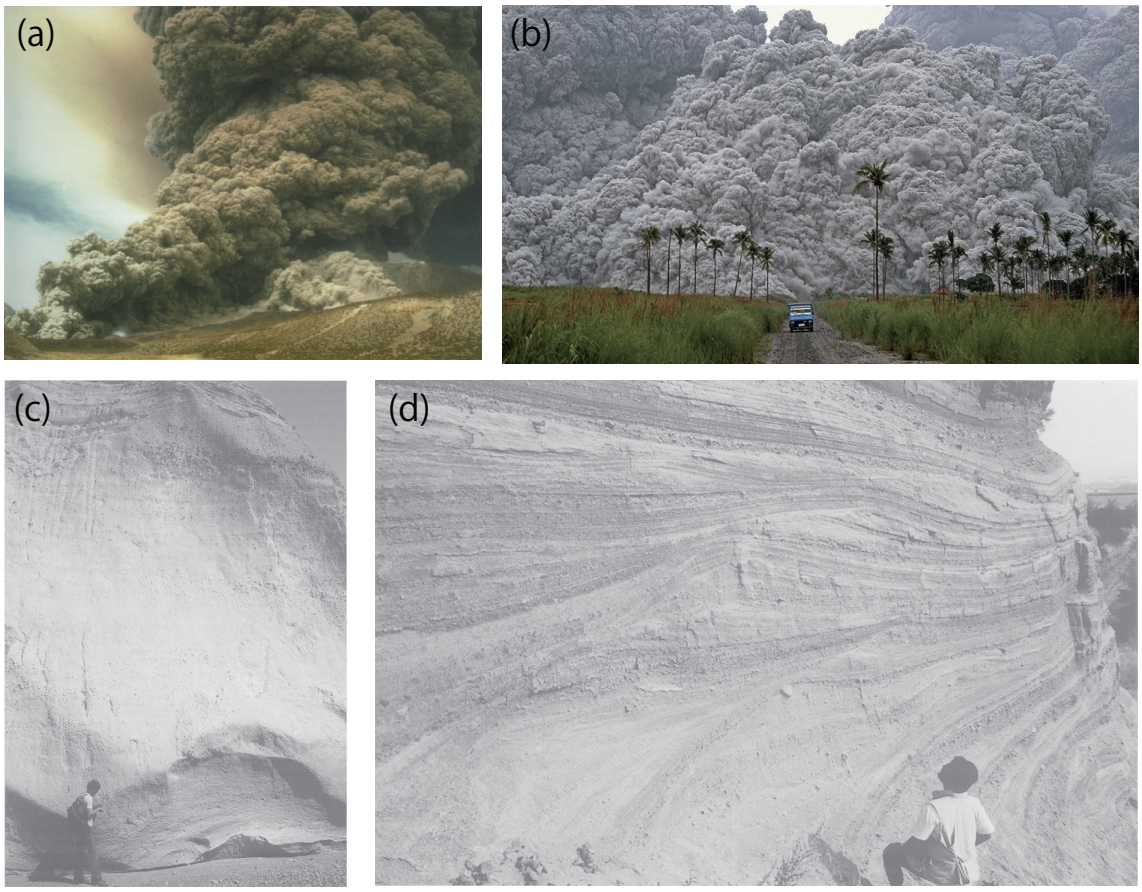

Figure 1.1: Pyroclastic density currents and their deposits. (a) Mount Lascar explodes, the 19 April 1993 (©Jacques Et Aicha Guarinos). (b) Mount Pinatubo explodes, the 17 June 1991 (©Alberto Garcia/Corbis). (c) Pyroclastic density current deposit from the 18 May 1980 eruption of Mount St. Hetens showing the typically massive lithofacies. Modified from Druitt (1998). (d) Pyroclastic density current deposit of the 11 ka Upper Laacher See Tuff (Germany) showing the well-developed sandwave stratified lithofacies. Modified from Druitt (1988).

1.1 Diversity of the deposits of pyroclastic density currents

1.1.1 First-order features

Generally the global features of the PDC deposits are characterized by distribution, volume, shape, aspect ratio, mass fraction of co-ignimbrite ash, and temperature of emplacement of PDC deposits. We call them the first-order features of the PDC deposits hereafter. The diversity of the first-order features of the PDC deposits are summarized as follows.

PDC deposits can cover areas from $1,000$ m^2 to $> 20,000$ km^2, be found at distances from 100 m to > 150 km from source (Miller & Smith, 1977; Fisher et al., 1993; Branney & Kokelaar, 2002). The volumes of PDC deposits vary from 0.001 to $> 1,000$ km^3 (Lindsay et al., 2001; Branney & Kokelaar, 2002; Cas et al., 2011; Brown & Andrews, 2015). The largest documented PDC deposits exceed $3,000$ km^3 (e.g., Toba caldera, Costa et al., 2014). When mapped, PDC deposits show a range of general shapes, from valley-confined deposits through to extensive near-circular sheets (Branney & Kokelaar, 2002; Brown & Branney, 2004; Brown & Branney, 2013). Valley-confined deposits are interpreted to be generated by currents that are confined within a canyon or valley, for example 1912 eruption of Valley of Ten Thousand Smokes (VTTS) ignimbrite, Alaska (e.g., Hildreth & Fierstein, 2012). Extensive near-circular sheets are interpreted to be generated by currents that traveled radially out from a volcano, for example the 28.5 ka Taupo ignimbrite, New Zealand (e.g., Wilson & Walker, 1985).

The aspect ratio of PDC deposits is thought to be one of the most important parameters which has been related to PDC dynamics and source conditions (Walker, 1983; Bursik & Woods, 1996; Giordano & Doronzo, 2017). The aspect ratios are determined by the ratios of the average thickness of the deposit to the diameter of a circle with the same surface area as the deposit, and they vary from 10^{-5} to 10^{-2} (Walker, 1983). High-aspect ratio PDC deposits, characterized by the aspect ratio of 10^{-2}–10^{-3}, are thick but not widely

spread (e.g., Katmai and Mount Pinatubo). On the other hand, low-aspect ratio PDC deposits, characterized by the aspect ratio of 10^{-4}–10^{-5}, are thin but widespread (e.g., Taupo). Most large volume PDC deposits are low-aspect ratio PDC deposits.

Buoyant plumes associated with PDCs are another important feature that characterizes the dynamics and deposits of PDCs. During a formation of a PDC, parts of the PDC can become lighter than ambient air to reverse buoyancy and liftoff. The liftoff of PDCs forms "co-ignimbrite ash plumes" (e.g., Woods & Kienle, 1994; Calder et al., 1997). This phenomenon implies that not all particles that initially contribute to PDCs are deposited within "PDC deposits." Indeed large fractions of particles are elutriated into buoyant co-ignimbrite plumes, whose deposits can amount to as much as 50% of the erupted mass (e.g., Machida & Arai, 1976, 1978; Sparks & Walker, 1977; Carey et al., 1990; Woods & Kienle, 1994; Koyaguchi & Ohno, 2001b). When inferring PDC behavior and eruption intensity (i.e., the mass eruption rate from source) from deposits, the fraction of tephra that enters co-ignimbrite ash plumes is important (e.g., Bursik & Woods, 1996; Koyaguchi & Ohno, 2001a and b; Andrews & Manga, 2012); however, it is difficult correctly to detect the fraction of co-ignimbrite ash from field observations, because the deposits of co-ignimbrite ash plumes are often areally extensive, very thin, and easily eroded (Sigurdsson & Carey, 1989; Fierstein & Nathenson, 1992; Calder et al., 1997; Branney & Kokelaar, 2002).

The temperature of emplacement of PDC deposits is also an important factor that controls the dynamics and the mode of emplacement of PDCs; it varies from < 100 to $1,000$ $^\circ$C depending on eruption style (e.g., Trolese et al., 2017). PDC deposits can be loose granular material or can be welding texture, because the onset of welding occurs at temperatures of the order of 600–750 $^\circ$C (Smith, 1960). The emplacement temperatures of PDCs are interpreted to depend on several factors, such as the starting magmatic temperature and the degree of interaction between the erupted materials and external influences such as air and/or water (McClelland & Druitt, 1989; Koyaguchi & Woods, 1996).

1.1.2 Second-order features

PDC deposits are extremely variable in not only the first-order features, but also sedimentary structures observed in single outcrops (i.e., lithofacies such as massive to stratified bedforms, ground layers, stratified topographic veneers, lateral levees, and steep front lobes). We call them the second-order features of the PDC deposits hereafter. The diversity of the second-order features of PDC deposits are summarized as follows.

PDC deposits commonly show poorly sorted massive (i.e., non-stratified) to stratified lithofacies, and multiple grading (i.e., normal and reverse grading, and density and size grading) (Fisher & Schmincke, 1984; Cas & Wright, 1987; Druitt, 1998; Branney & Kokelaar, 2002; Sulpizio et al., 2014; Brown & Andrews, 2015). There are two conceptual models for the deposition mechanisms of poorly sorted massive lithofacies: "*en masse* deposition" and "progressive aggradation" (Branney & Kokelaar, 2002; Roche, 2012). In *en masse* deposition, the current with high particle concentration freezes through its entire height (Sparks, 1976). In this model, the vertical structures of PDC deposits are considered to preserve the vertical flow structures (i.e., the paradigm of the standard ignimbrite flow-unit; Sparks et al., 1973; Sparks, 1976). In progressive aggradation, the deposit builds up by progressive accumulation of material (Fisher, 1966; Branney and Kokelaar, 1992). In this model, the vertical structures of PDC deposits reflect temporal variations of the conditions of the lower portion of the flow that undergo deposition (i.e., flow-boundary zone).

At bases of PDC deposits, a wide variety of thin, stratified and relatively sorted layers commonly occurs (e.g., Sparks & Walker, 1973; Walker et al., 1981a; Valentine et al., 1990; Fujii & Nakada, 1999). Such layers are called as "ground layer" (Sparks & Walker, 1973; Sparks, 1976). Ground layers may record the dynamics of PDC such as the initial advance of the current across the landscape, and/or the flow-boundary conditions near the flow front (Branney & Kokelaar, 2002).

Sedimentary structures of PDCs are also affected by local topography. Relatively thin

and stratified lithofacies of PDC deposits are common on topographic highs (e.g., Wohletz & Sheridan, 1979; Walker et al., 1981b). Such deposits are called as "stratified veneer." Stratified topographic veneers are inferred to derive from the "tail" or "skin" of a current with high particle concentration (Walker et al., 1980a; Wilson & Walker, 1982; Wilson, 1986) or from a current with low particle concentration (e.g., Fisher et al., 1980b).

In some (small volume) PDC deposits, there are structures like lateral levees and steep front lobes (e.g., Rowley et al., 1981; Lube et al., 2007). This morphology is formed by large clasts, and typically inferred to indicate segregation in concentrated flow at the flow front and margins (Gray & Kokelaar, 2010). The morphology is also inferred to be formed by the spatial and temporal variations of friction caused by interstitial gas pore pressure (Gueugneau et al., 2017).

Extremely diverse PDC deposits shown above are formed by transport and deposition processes (e.g., Branney & Kokelaar, 2002). In PDC deposits, there are both aspects of directly recording transport and deposition processes, such as *en masse* freezing (Sparks, 1976), and of not directly recording transport process, such as progressive aggradation (Fisher, 1966; Branney & Kokelaar, 1992). Thus, in order to account for the diversity of PDC deposits, not only the field-based work and experimental-analogue modeling of PDC behavior and sedimentation but also numerical studies that unify the large-scale field observation and individual physical processes are needed (e.g., Branney & Kokelaar, 2002; Roche et al., 2013b; Dufek et al., 2015; Dufek, 2016).

1.2 Physical processes

Generally physics of sedimentation is strongly dependent on volume fraction of suspended particles in a fluid (e.g., Allen, 1984). The above diversity of PDC deposits is considered to result mainly from a wide range of particle volume fraction in PDCs (Branney & Kokelaar, 2002). PDCs generally develop density stratification in which particle concentrations remarkably increase toward the base (Valentine, 1987; Branney & Koke-

laar, 2002; Burgisser & Bergantz, 2002; Breard et al., 2016). The density stratification mainly consists of a coupled voluminous dilute turbulent suspension flow and the basal thin dense flow (Figure 1.2a; e.g., Branney & Kokelaar, 2002; Roche et al., 2013b; Dufek et al., 2015; Dufek, 2016). Indeed, Hoblitt (1986) observed a basal dense current sometimes revealed beneath turbulent ash clouds for the 22 July and 7 August 1980 flows of Mount St. Helens.

The particle concentration is $\lesssim 1$ vol.% in the dilute current, and ~ 10 vol.% in the dense current (e.g., Breard et al., 2016). Because of such difference in particle volume fraction, mechanisms that determine the runout distance are qualitatively different between dilute and dense currents. Dilute currents can become lighter than ambient air to reverse buoyancy and liftoff (e.g., Andrews, 2014). The runout distance of the dilute current is, therefore, the distance between the liftoff position and source position (Figure 1.2a). The dense current can stop due to the basal friction and/or sedimentation (e.g., Roche, 2012). The runout distance of the dense current is the distance between the stop position and source position (Figure 1.2a). The relative magnitude of these runout distances governs the distribution of PDC deposits, and may also affect the lithofacies of PDC deposits. The runout distance of each part is controlled by different physical processes due to the difference in the particle volume fraction (Figure 1.2b; e.g., Roche et al., 2013b; Dufek et al., 2015; Dufek, 2016), which are summarized as follows.

1.2.1 Dilute part

The dynamics of dilute PDCs is mainly controlled by frontal resistance of ambient air, particle settling, entrainment air, and thermal expansion of entrained air. Each of these process has been studied on the basis of laboratory experiments.

Dilute PDCs share much in common with a simple gravity current generated by some laboratory experiments which have commonly taken the form of lock-exchange experiments (e.g., Huppert & Simpson, 1980; Rottman & Simpson, 1983; Marino et al., 2005).

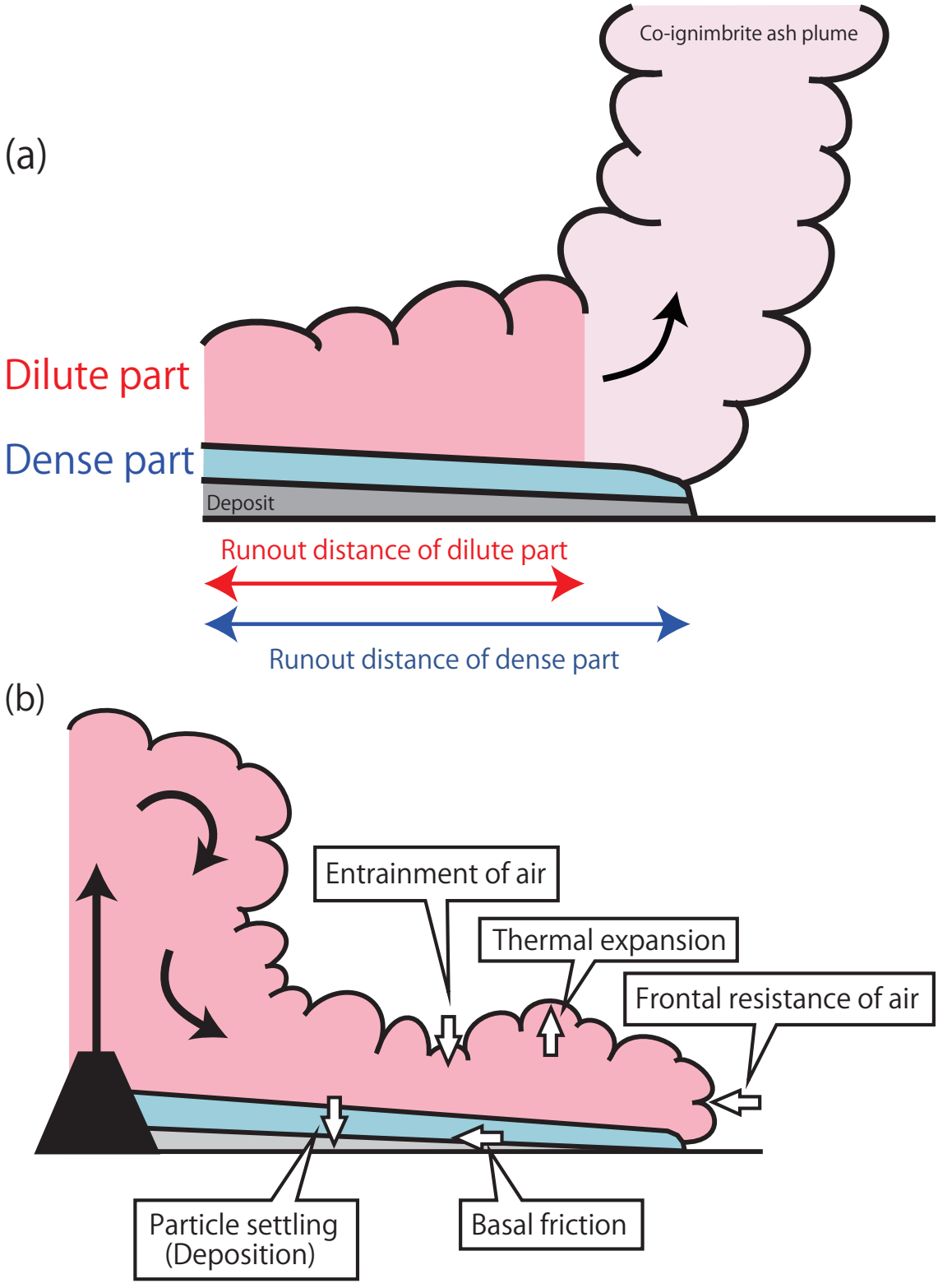

Figure 1.2: Schematic illustrations of pyroclastic density currents. (a) Vertical density stratification and runout distance. The vertical density stratification mainly consists of a voluminous dilute turbulent suspension (red region) and the basal thin dense part (blue region). (b) Physical processes underlying the dynamics of pyroclastic density currents.

Typically, the gravity current were generated by releasing a saline fluid into water where the density contrast between both fluids was small. Experiments and theoretical modeling have shown that the dynamics of the gravity currents are critically affected by a mechanical balance between the buoyancy pressure driving the current front and the resistance pressure caused by the acceleration of the ambient fluid around the front (e.g., Benjamin, 1968; Huppert & Simpson, 1980; Ungarish, 2007; Shimizu et al., 2017). This condition is known as the front condition (Ungarish, 2009). The momentum loss due to the resistance of the ambient fluid at the front leads to the morphology defined as comprising a head preceding a body.

Lock-exchange experiments and theoretical modeling for a particle-laden gravity current have also shown that the degree of particle settling from the base of the current can change the dynamics of the gravity current and the deposition pattern of the sediment (Bonnecaze et al., 1993). Further experiments were undertaken where the interstitial fluid in the gravity current was lighter than the ambient fluid (Sparks et al., 1993). In these experiments, when sufficient particles settled, the bulk density of the gravity current became less than that of the ambient fluid, and the gravity current rose as a plume.

When a current propagates rapidly, ambient air is entrained in the gravity currents owing to high shear conditions around the flow surface. From laboratory experiments, the role of entrainment of the ambient air into the gravity current has been quantified as a function of non-dimensional number, the Richardson number, which represents the ratio of the stabilizing stratification of the current to destabilizing velocity shear (Ellison & Turner, 1959; Parker et al., 1987). The empirical law derived from the experiments has been used in a wide range of numerical models of gravity currents (e.g., Bursik & Woods, 1996; Johnson & Hogg, 2013; Shimizu et al., 2017).

As mentioned above, when much ambient fluid is entrained and thermally expanded prior to the current sedimentation of much particles, some portions of the hot current undergo a buoyancy reversal, creating secondary plumes (Woods & Kienle, 1994; Bursik & Woods, 1996; Calder et al., 1997; Andrews & Manga, 2012; Andrews, 2014). This

general feature of spreading of hot dilute PDCs and generation of co-ignimbrite plumes have been reproduced in experiments for dilute turbulent suspension gravity currents at ambient and high temperatures (Andrews & Manga, 2012; Andrews, 2014).

1.2.2 Dense part

The dynamics of dense PDCs is mainly controlled by basal friction, deposition, and particle supply from the upper dilute current. Dense PDCs share much in common with a (fluidized) granular flow generated by an instantaneous release of an initially fluidized bed (e.g., Roche et al., 2008). The lock-release experiments on the initially fluidized granular flows showed that their dynamics depends on the diffusion timescale of the high-pore pressure developed initially (Roche et al., 2008; Roche, 2012). Because of the differences of the pore pressure, the initially fluidized granular flows can be either propagating as inertial flows having a high-mobility under a fluid-inertial regime or as dry granular flows under a granular-frictional regime (Roche, 2012). Once the pore-pressure has decreased by diffusion, the flow, which initially behaves as a inertial flow, enters the frictional regime and stopping phase (Roche, 2012; Gueugneau et al., 2017).

Experiments of granular flows on erodible ground bed indicate that erosion of the ground bed may play a role under some conditions. The initially fluidized granular flows generally consist of a sliding head preceding a body (Roche et al., 2010). The body is characterized by a flow with a no-slip boundary condition wherein the deposit is aggraded at a nearly constant rate (Gilorami et al., 2008, 2010, 2015). In the sliding head, on the other hand, slip-velocity develops at the base, which can cause erosion of the ground bed (Roche et al., 2013a). The deposition and erosion processes of the (fluidized) granular flows is not fully understood.

Finally, recent large scale experiments of PDCs with strong density stratification (Breard et al., 2016; Breard & Lube, 2017) indicate that the interaction between the dilute and dense parts is of importance. In these experiments, a significant particle mass flux from

the overriding dilute current into the basal dense current is observed, which controls the global dynamics of the dilute and dense currents.

1.3 Object of this study

We aim to relate the above diverse features of PDC deposits with the above underlying physical processes, by investigating PDC dynamics under the various supplied conditions. As shown above, there is a vast amount of field-based works related with the diversity of PDC deposits and experimental-analogue and numerical studies related with the physical processes underlying PDC dynamics. On the other hand, there are only few studies that unify the diversity of PDC deposits and the underlying physical processes (e.g., Bursik & Woods, 1996; Dade & Huppert, 1996; Doyle et al., 2008). Accordingly, a global relationship between the sedimentological features of PDC deposits, the underlying physical processes, and the PDC dynamics connecting them under various eruption conditions (e.g., the mass eruption rate, grain size distribution, and temperature) remains unsolved.

In order to assess the effects of the above physical processes on PDC dynamics and the resulting deposits, we will model PDC dynamics by the depth-averaged shallow-water equations. The essential behavior of density currents can be described by the depth-averaged shallow-water equations (e.g., Ungarish, 2009; Dufek, 2016). Since the underlying physical processes are described explicitly in the shallow-water equations, an extensive parametric analysis based on the shallow-water equations offers better prospects for assessing the effects of these physical processes on the global dynamics of gravity currents.

The depth-averaged shallow-water approach has been widely used to model PDCs (Table 1.1). Bursik & Woods (1996) developed a one-layer model for dilute turbulent suspension currents at steady state. In this model, particle settling from the base of the current and thermal expansion of air entrained from the upper surface of the current reduce the density of the current, eventually leading to buoyancy reversal and final runout of

the current. On the basis of this model, Bursik & Woods (1996) have explicitly shown that the runout distance of the dilute current is critically controlled by magma discharge rate of eruptions. This one-layer model for dilute currents, however, does not account for the effects of the dense current. As mentioned above, the strong density stratification develops in PDCs, and the dilute and dense parts are controlled by different physical processes (Figure 1.2b). Thus, we will take a two-layer approach as Doyle et al. (2008). Doyle et al. (2008, 2010, 2011) developed an unsteady two-layer model for PDCs with strong density stratification, in which dilute and dense layers evolve separately but are coupled through mass exchange as suspended particles in the dilute layer settles into the basal dense layer. In this model, particles settling from the dilute turbulent current form the basal dense current. Doyle et al. (2008) showed that the strong density stratification leads to qualitatively different regimes for determining the runout distance; however, their model does not provide a quantitative estimation of runout distance, because the effects of the thermal expansion of air entrained into the dilute current are not taken into consideration in their model.

To assess the effects of all the physical processes, including the effects of thermal expansion of entrained air and strong density stratification, on PDC dynamics and the resulting deposits, we develop a new unsteady two-layer model (Table 1.1). We previously showed that frontal resistance of air is especially important in behavior of the dilute layer (Shimizu et al., 2017), so that we also consider this effect correctly in our model.

Table 1.1: Physical processes taken into account in previous and our depth-averaged shallow-water models for the dynamics of pyroclastic density currents.

		Dilute layer			Dense layer
		Particle settling	Entrainment of air and thermal expansion	Frontal resistance	Particle supply, deposition, and basal friction
Bursik & Woods (1996)	Steady	✓	✓		
Doyle et al. (2008, 10, 11)	Unsteady	✓			✓
Our study	Unsteady	✓	✓	✓	✓

The two-layer approach that we will take can capture the essential natures of the dynamics of PDCs with strong density stratification. It may be difficult to distinguish the dilute and dense parts on the basis of the observations from outside. Clast concentrations in the density stratification of natural PDCs "gradually" increase toward the base. Moreover, a part of the dilute current may be derived by elutriation from the underlying dense parts. For example, when much particles are transported by the dilute current, the fluid dynamical feature can be approximated by the two-layer model where the dilute current travels more rapidly than the underlying dense layer (Figure 1.3a). On the other hand, when much particles are transported by the dense current, the fluid dynamical feature can be approximated by the two-layer model where the lower dense current travels more rapidly than the overlying dilute layer (Figure 1.3b). We, therefore, consider that the two-layer approach is very useful to relate such PDC dynamics with the diverse features of PDC deposits.

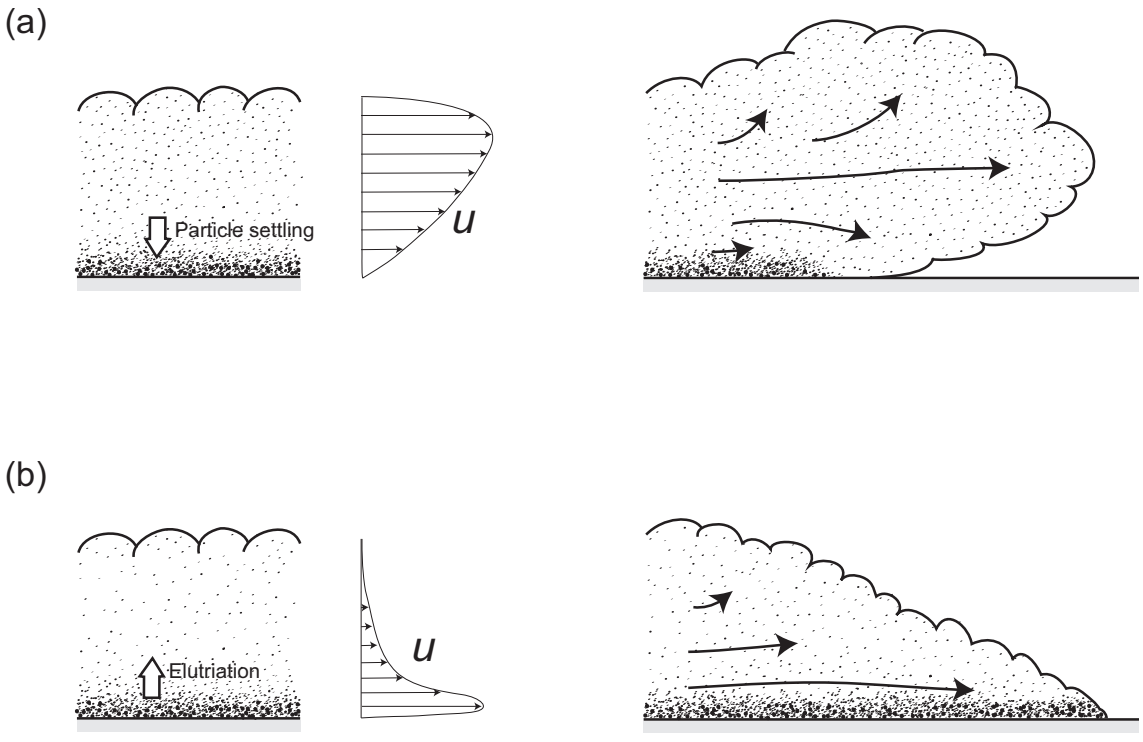

Figure 1.3: Schematic illustrations of the dynamics of pyroclastic density currents. u is horizontal velocity. Modified from Branney & Kokelaar (2002). (a) Much particles are transported by the upper dilute part. (b) Much particles are transported by the lower dense current.

The present thesis provides insights into the relationships between the diversity of PDC deposits and the physical processes dominating PDC dynamics, on the basis of numerical simulations of the new unsteady two-layer shallow-water model. The remainder of this thesis is organized as follows. Chapter 2 describes the formulation of the new unsteady two-layer shallow-water model. Chapter 3 describes numerical procedures of the model. Chapter 4 shows the representative numerical results of the model. Chapter 5 discusses the origin of the fluid dynamical feature of the numerical results, particularly mechanisms determining the runout distance of PDCs. Chapter 6 describes geological implications of the numerical study on the diversity of PDC deposits. Finally, Chapter 7 represents the conclusion of this thesis and future studies.

Chapter 2

Formulation

We formulate a new unsteady two-layer shallow-water model for the dynamics of pyroclastic density currents (PDCs). In general, PDCs are unsteady phenomena and are characterized by strong density stratification due to particle settling (e.g., Branney and Kokelaar, 2002), whereby a dilute gravity current (particle suspension flow) overrides the dense basal gravity current (fluidized granular flow) (Figure 1.2).

In previous unsteady two-layer models (Doyle et al., 2008, 2010, 2011; Kelfoun, 2017; Kelfoun et al., 2017), the mass and momentum conservation equations of each layer are solved, but the energy conservation equation of dilute layer is not solved. The dynamics of the dilute part of PDCs is strongly affected by the thermal expansion of entrained air (Bursik & Woods, 1996; Andrews & Manga, 2012). Although a steady energy conservation equation of the dilute layer is formulated in Bursik & Woods (1996), the unsteady energy conservation equation has not been formulated yet. Therefore, in this chapter, we derive a generalized unsteady one-layer shallow-water equations including the energy conservation equation (Section 2.1), and formulate a new unsteady two-layer PDC model on the basis of the generalized unsteady one-layer model (Section 2.2). The notations of variables shown in these models are summarized in Appendix A.

2.1 One-layer model of inviscid gravity currents

In this section, we derive a generalized unsteady one-layer shallow-water equations including the energy conservation equation from the inviscid Navier–Stokes equations. The basic methodology of deriving these equations is based on Chapter 2 in Ungarish (2009).

2.1.1 Inviscid Navier–Stokes equations

We consider an inviscid gravity current propagating into an ambient of density ρ_{a}, along a slope inclined at $\theta(=\text{ const})$ to the horizontal (where x is parallel to the slope and z perpendicular, Figure 2.1). The conservation equations of mass, x-direction momentum, z-direction momentum and total energy for the inviscid gravity current are (e.g., Toro, 2009)

$$\frac{\partial \rho}{\partial t} + \frac{\partial}{\partial x}(\rho u) + \frac{\partial}{\partial z}(\rho w) = 0, \tag{2.1}$$

$$\frac{\partial}{\partial t}(\rho u) + \frac{\partial}{\partial x}(\rho u^2 + p) + \frac{\partial}{\partial z}(\rho u w) = \rho g \sin\theta, \tag{2.2}$$

$$\frac{\partial}{\partial t}(\rho w) + \frac{\partial}{\partial x}(\rho u w) + \frac{\partial}{\partial z}(\rho w^2 + p) = -\rho g \cos\theta, \tag{2.3}$$

$$\frac{\partial}{\partial t}(\rho e_{\mathrm{tot}}) + \frac{\partial}{\partial x}((\rho e_{\mathrm{tot}} + p)u) + \frac{\partial}{\partial z}((\rho e_{\mathrm{tot}} + p)w) = 0. \tag{2.4}$$

This system is called the inviscid Navier–Stokes (i.e., Euler) equations. Here, t is the propagation time, $\rho(x, z, t)$ is the mass density, $u(x, z, t)$ is the x-component of velocity, $w(x, z, t)$ is the z-component of velocity, $p(x, z, t)$ is the thermodynamic pressure, $e_{\mathrm{tot}}(x, z, t)$ is the total energy per unit mass, and g is the acceleration due to gravity. The $e_{\mathrm{tot}}(x, z, t)$ is defined with

$$e_{\mathrm{tot}} \equiv e + \frac{1}{2}(u^2 + w^2) + g(z\cos\theta - x\sin\theta), \tag{2.5}$$

where e is the specific internal energy, $(u^2+w^2)/2$ is the specific kinetic energy, $g(z\cos\theta - x\sin\theta)$ is the specific potential energy.

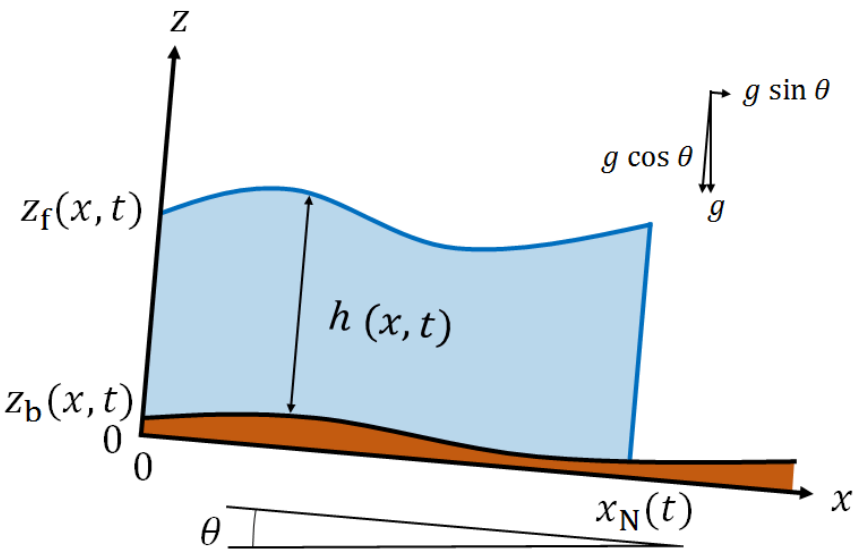

Figure 2.1: Schematic illustration of the inviscid gravity current of depth $h(x,t)$, propagating along a slope inclined at θ to the horizontal, with x parallel to the slope and z perpendicular. There are three interfaces, between the top of the current and the surrounding ambient fluid ($z = z_{\rm f}(x,t)$), between the front of the current and the ambient fluid ($x = x_{\rm N}(t)$), and between the bottom of the current and the local topography imposed on the slope ($z = z_{\rm b}(x,t)$).

For an ideal gas, thermodynamic variables (i.e., pressure p, density ρ and temperature T) can be related via the thermal equation of state

$$\frac{1}{\rho} = \frac{RT}{p}, \tag{2.6}$$

where R is a constant, which depends on the kind of gas. The temperature T can also be related to the internal energy e via a caloric equation of state

$$\mathrm{d}e = C_{\rm v}\mathrm{d}T \tag{2.7}$$

or

$$\mathrm{d}\left(e + \frac{p}{\rho}\right) = C_{\rm p}\mathrm{d}T, \tag{2.8}$$

where $C_{\rm v}$ (= const) is the heat capacity at constant volume and $C_{\rm p}$ (= const) is the heat

capacity at constant pressure. From Eqs. (2.6), (2.7) and (2.8),

$$R = C_{\mathrm{p}} - C_{\mathrm{v}} \tag{2.9}$$

is obtained.

2.1.2 Kinematic conditions

To derive the depth-averaged shallow-water equations from the Navier–Stokes equations (i.e., Eqs. (2.1)–(2.4)), we must integrate the Navier–Stokes equations across the depth of the current. Before integrating the Navier–Stokes equations, we introduce the kinematic condition, which is applied to determine the elevation of the free surface.

We consider the interface of the gravity current as a discontinuity of the density, and denote the locus of this discontinuity by using a function $\Sigma(x, z, t) = 0$ (e.g., Ungarish, 2009). The full differential of $\Sigma(x, z, t) = 0$ yields

$$\begin{aligned} & \mathrm{d}\Sigma = 0 \\ \therefore \quad & \frac{\partial \Sigma}{\partial t} + \frac{\mathrm{d}x}{\mathrm{d}t}\frac{\partial \Sigma}{\partial x} + \frac{\mathrm{d}z}{\mathrm{d}t}\frac{\partial \Sigma}{\partial z} = 0 \qquad (\because\ \mathrm{d}t \neq 0). \end{aligned} \tag{2.10}$$

The rates of displacement of the interface, $\mathrm{d}x/\mathrm{d}t$ and $\mathrm{d}z/\mathrm{d}t$, are the velocities of the fluid at the interface, so that the kinematic condition for the interface of the gravity current:

$$\frac{\partial \Sigma}{\partial t} + u\frac{\partial \Sigma}{\partial x} + w\frac{\partial \Sigma}{\partial z} = 0 \tag{2.11}$$

is obtained.

There are three interfaces, between the top of the current and the surrounding ambient fluid, between the front of the current and the ambient fluid, and between the bottom of the current and the local topography imposed on the slope (Figure 2.1). The interface between the top of the current and the ambient fluid is denoted by the subscript f, the

locus of which is given by $\Sigma_{\mathrm{f}} = z - z_{\mathrm{f}}(x,t) = 0$. Substituting this into Eq. (2.11), we obtain the kinematic condition at $z = z_{\mathrm{f}}(x,t)$:

$$\begin{aligned} & \frac{\partial}{\partial t}(z - z_{\mathrm{f}}(x,t)) + u_{\mathrm{f}}\frac{\partial}{\partial x}(z - z_{\mathrm{f}}(x,t)) + w_{\mathrm{f}}\frac{\partial}{\partial z}(z - z_{\mathrm{f}}(x,t)) = 0 \\ \therefore \quad & \frac{\partial z_{\mathrm{f}}}{\partial t} + u_{\mathrm{f}}\frac{\partial z_{\mathrm{f}}}{\partial x} - w_{\mathrm{f}} = 0, \end{aligned} \tag{2.12}$$

where u_{f} and w_{f} are the velocities of the fluid at $z = z_{\mathrm{f}}(x,t)$. The interface $z_{\mathrm{f}}(x,t)$ is related with the current depth $h(x,t)$ and the local topography $z_{\mathrm{b}}(x,t)$ via

$$z_{\mathrm{f}}(x,t) = h(x,t) + z_{\mathrm{b}}(x,t). \tag{2.13}$$

The interface between the bottom of the current and the local topography is denoted by the subscript b, the locus of which is given by $\Sigma_{\mathrm{b}} = z - z_{\mathrm{b}}(x,t) = 0$. Substituting this into Eq. (2.11), we obtain the kinematic condition at $z = z_{\mathrm{b}}(x,t)$:

$$\frac{\partial z_{\mathrm{b}}}{\partial t} + u_{\mathrm{b}}\frac{\partial z_{\mathrm{b}}}{\partial x} - w_{\mathrm{b}} = 0, \tag{2.14}$$

where u_{b} and w_{b} are the velocities of the fluid at $z = z_{\mathrm{b}}(x,t)$. The interface between the front of the current and the ambient fluid is denoted by the subscript N, the locus of which is given by $\Sigma_{\mathrm{N}} = x - x_{\mathrm{N}}(t) = 0$. Substituting this into Eq. (2.11), we obtain the kinematic condition at $x = x_{\mathrm{N}}(t)$:

$$\begin{aligned} & \frac{\partial}{\partial t}(x - x_{\mathrm{N}}(t)) + u_{\mathrm{N}}\frac{\partial}{\partial x}(x - x_{\mathrm{N}}(t)) + w_{\mathrm{N}}\frac{\partial}{\partial z}(x - x_{\mathrm{N}}(t)) = 0 \\ \therefore \quad & \frac{\mathrm{d}x_{\mathrm{N}}}{\mathrm{d}t} = u_{\mathrm{N}}, \end{aligned} \tag{2.15}$$

where u_{N} and w_{N} are the depth averaged velocities of the fluid at $x = x_{\mathrm{N}}(t)$.

2.1.3 Depth integrating

We integrate Eqs. (2.1)–(2.4) from $z = z_\mathrm{b}(x,t)$ to $z = z_\mathrm{f}(x,t)$. The kinematic conditions (2.12) and (2.14) are used in this integration. We give Leibniz's rule for differentiation of an integral for the following derivations:

$$\frac{\mathrm{d}}{\mathrm{d}\eta}\int_{a(\eta)}^{b(\eta)} f(z,\eta)\,\mathrm{d}z = \int_{a(\eta)}^{b(\eta)} \frac{\mathrm{d}}{\mathrm{d}\eta} f(z,\eta)\,\mathrm{d}z + f(b,\eta)\frac{\mathrm{d}b}{\mathrm{d}\eta} - f(a,\eta)\frac{\mathrm{d}a}{\mathrm{d}\eta}. \tag{2.16}$$

Mass conservation equation

The mass conservation Eq. (2.1) is integrated from $z = z_\mathrm{b}(x,t)$ to $z = z_\mathrm{f}(x,t)$ to yield

$$\int_{z_\mathrm{b}}^{z_\mathrm{f}} \frac{\partial \rho}{\partial t}\,\mathrm{d}z + \int_{z_\mathrm{b}}^{z_\mathrm{f}} \frac{\partial}{\partial x}(\rho u)\,\mathrm{d}z + \rho_\mathrm{f} w_\mathrm{f} - \rho_\mathrm{b} w_\mathrm{b} = 0. \tag{2.17}$$

Applying Leibniz's rule (2.16) to Eq. (2.17), we obtain

$$\begin{aligned} & \frac{\partial}{\partial t}\int_{z_\mathrm{b}}^{z_\mathrm{f}} \rho\,\mathrm{d}z - \rho_\mathrm{f}\frac{\partial z_\mathrm{f}}{\partial t} + \rho_\mathrm{b}\frac{\partial z_\mathrm{b}}{\partial t} + \frac{\partial}{\partial x}\int_{z_\mathrm{b}}^{z_\mathrm{f}} (\rho u)\,\mathrm{d}z - \rho_\mathrm{f} u_\mathrm{f}\frac{\partial z_\mathrm{f}}{\partial x} + \rho_\mathrm{b} u_\mathrm{b}\frac{\partial z_\mathrm{b}}{\partial x} \\ & \qquad + \rho_\mathrm{f} w_\mathrm{f} - \rho_\mathrm{b} w_\mathrm{b} = 0 \\ \therefore \quad & \frac{\partial}{\partial t}\int_{z_\mathrm{b}}^{z_\mathrm{f}} \rho\,\mathrm{d}z + \frac{\partial}{\partial x}\int_{z_\mathrm{b}}^{z_\mathrm{f}} (\rho u)\,\mathrm{d}z \\ & \qquad - \rho_\mathrm{f}\left(\frac{\partial z_\mathrm{f}}{\partial t} + u_\mathrm{f}\frac{\partial z_\mathrm{f}}{\partial x} - w_\mathrm{f}\right) + \rho_\mathrm{b}\left(\frac{\partial z_\mathrm{b}}{\partial t} + u_\mathrm{b}\frac{\partial z_\mathrm{b}}{\partial x} - w_\mathrm{b}\right) = 0. \end{aligned} \tag{2.18}$$

Using this formula and the kinematic conditions (2.12) and (2.14), we write

$$\frac{\partial}{\partial t}\int_{z_\mathrm{b}}^{z_\mathrm{f}} \rho\,\mathrm{d}z + \frac{\partial}{\partial x}\int_{z_\mathrm{b}}^{z_\mathrm{f}} (\rho u)\,\mathrm{d}z = 0. \tag{2.19}$$

We introduce the straightforward definitions of the depth-averaged density and mass flux:

$$\overline{\rho} \equiv \frac{1}{h}\int_{z_\mathrm{b}}^{z_\mathrm{f}} \rho\,\mathrm{d}z \quad , \qquad \overline{\rho u} \equiv \frac{1}{h}\int_{z_\mathrm{b}}^{z_\mathrm{f}} (\rho u)\,\mathrm{d}z. \tag{2.20}$$

Using these and Eq. (2.13), we rewrite Eq. (2.19) as

$$\frac{\partial}{\partial t}(\overline{\rho}h) + \frac{\partial}{\partial x}(\overline{\rho u}h) = 0. \tag{2.21}$$

Momentum conservation equation in the x direction

The x-momentum conservation Eq. (2.2) is integrated from $z = z_{\mathrm{b}}(x,t)$ to $z = z_{\mathrm{f}}(x,t)$ to yield

$$\int_{z_{\mathrm{b}}}^{z_{\mathrm{f}}} \frac{\partial}{\partial t}(\rho u)\,\mathrm{d}z + \int_{z_{\mathrm{b}}}^{z_{\mathrm{f}}} \frac{\partial}{\partial x}(\rho u^2 + p)\,\mathrm{d}z + \rho_{\mathrm{f}} u_{\mathrm{f}} w_{\mathrm{f}} - \rho_{\mathrm{b}} u_{\mathrm{b}} w_{\mathrm{b}} = g\sin\theta \int_{z_{\mathrm{b}}}^{z_{\mathrm{f}}} \rho\,\mathrm{d}z. \tag{2.22}$$

Applying Leibniz's rule (2.16) to Eq. (2.22), we obtain

$$\begin{aligned}
&\frac{\partial}{\partial t}\int_{z_{\mathrm{b}}}^{z_{\mathrm{f}}} (\rho u)\,\mathrm{d}z - \rho_{\mathrm{f}} u_{\mathrm{f}} \frac{\partial z_{\mathrm{f}}}{\partial t} + \rho_{\mathrm{b}} u_{\mathrm{b}} \frac{\partial z_{\mathrm{b}}}{\partial t} + \frac{\partial}{\partial x}\int_{z_{\mathrm{b}}}^{z_{\mathrm{f}}} (\rho u^2)\,\mathrm{d}z - \rho_{\mathrm{f}} u_{\mathrm{f}}^2 \frac{\partial z_{\mathrm{f}}}{\partial x} + \rho_{\mathrm{b}} u_{\mathrm{b}}^2 \frac{\partial z_{\mathrm{b}}}{\partial x} \\
&\qquad + \frac{\partial}{\partial x}\int_{z_{\mathrm{b}}}^{z_{\mathrm{f}}} p\,\mathrm{d}z - p_{\mathrm{f}} \frac{\partial z_{\mathrm{f}}}{\partial x} + p_{\mathrm{b}} \frac{\partial z_{\mathrm{b}}}{\partial x} + \rho_{\mathrm{f}} u_{\mathrm{f}} w_{\mathrm{f}} - \rho_{\mathrm{b}} u_{\mathrm{b}} w_{\mathrm{b}} = g\sin\theta \int_{z_{\mathrm{b}}}^{z_{\mathrm{f}}} \rho\,\mathrm{d}z \\
\therefore \quad &\frac{\partial}{\partial t}\int_{z_{\mathrm{b}}}^{z_{\mathrm{f}}} (\rho u)\,\mathrm{d}z + \frac{\partial}{\partial x}\int_{z_{\mathrm{b}}}^{z_{\mathrm{f}}} (\rho u^2)\,\mathrm{d}z + \frac{\partial}{\partial x}\int_{z_{\mathrm{b}}}^{z_{\mathrm{f}}} p\,\mathrm{d}z - p_{\mathrm{f}} \frac{\partial z_{\mathrm{f}}}{\partial x} + p_{\mathrm{b}} \frac{\partial z_{\mathrm{b}}}{\partial x} \\
&\qquad -\rho_{\mathrm{f}} u_{\mathrm{f}} \left(\frac{\partial z_{\mathrm{f}}}{\partial t} + u_{\mathrm{f}} \frac{\partial z_{\mathrm{f}}}{\partial x} - w_{\mathrm{f}} \right) + \rho_{\mathrm{b}} u_{\mathrm{b}} \left(\frac{\partial z_b}{\partial t} + u_{\mathrm{b}} \frac{\partial z_{\mathrm{b}}}{\partial x} - w_{\mathrm{b}} \right) = g\sin\theta \int_{z_{\mathrm{b}}}^{z_{\mathrm{f}}} \rho\,\mathrm{d}z.
\end{aligned} \tag{2.23}$$

Using this formula and the kinematic conditions (2.12) and (2.14), we write

$$\frac{\partial}{\partial t}\int_{z_{\mathrm{b}}}^{z_{\mathrm{f}}} (\rho u)\,\mathrm{d}z + \frac{\partial}{\partial x}\int_{z_{\mathrm{b}}}^{z_{\mathrm{f}}} (\rho u^2)\,\mathrm{d}z + \frac{\partial}{\partial x}\int_{z_{\mathrm{b}}}^{z_{\mathrm{f}}} p\,\mathrm{d}z - p_{\mathrm{f}} \frac{\partial z_{\mathrm{f}}}{\partial x} + p_{\mathrm{b}} \frac{\partial z_{\mathrm{b}}}{\partial x} = g\sin\theta \int_{z_{\mathrm{b}}}^{z_{\mathrm{f}}} \rho\,\mathrm{d}z. \tag{2.24}$$

We introduce the straightforward definitions of the depth-averaged x-momentum flux and thermodynamic pressure:

$$\overline{\rho u^2} \equiv \frac{1}{h}\int_{z_{\mathrm{b}}}^{z_{\mathrm{f}}} (\rho u^2)\,\mathrm{d}z \quad , \qquad \overline{p} \equiv \frac{1}{h}\int_{z_{\mathrm{b}}}^{z_{\mathrm{f}}} p\,\mathrm{d}z. \tag{2.25}$$

Using these and Eqs. (2.13) and (2.20), we rewrite Eq. (2.24) as

$$\frac{\partial}{\partial t}(\overline{\rho u}h) + \frac{\partial}{\partial x}(\overline{\rho u^2}h + \overline{p}h) - p_\mathrm{f}\frac{\partial z_\mathrm{f}}{\partial x} + p_\mathrm{b}\frac{\partial z_\mathrm{b}}{\partial x} = \overline{\rho}gh\sin\theta. \tag{2.26}$$

Momentum conservation equation in the z direction

The z-momentum conservation Eq. (2.3) is integrated from $z = z_\mathrm{b}(x,t)$ to $z = z_\mathrm{f}(x,t)$ to yield

$$\begin{aligned}\int_{z_\mathrm{b}}^{z_\mathrm{f}} \frac{\partial}{\partial t}(\rho w)\,\mathrm{d}z + \int_{z_\mathrm{b}}^{z_\mathrm{f}} \frac{\partial}{\partial x}(\rho u w)\,\mathrm{d}z \\ +\rho_\mathrm{f}w_\mathrm{f}^2 - \rho_\mathrm{b}w_\mathrm{b}^2 + p_\mathrm{f} - p_\mathrm{b} = -g\cos\theta\int_{z_\mathrm{b}}^{z_\mathrm{f}}\rho\,\mathrm{d}z.\end{aligned} \tag{2.27}$$

Applying Leibniz's rule (2.16) to Eq. (2.27), we obtain

$$\begin{aligned}&\frac{\partial}{\partial t}\int_{z_\mathrm{b}}^{z_\mathrm{f}}(\rho w)\,\mathrm{d}z - \rho_\mathrm{f}w_\mathrm{f}\frac{\partial z_\mathrm{f}}{\partial t} + \rho_\mathrm{b}w_\mathrm{b}\frac{\partial z_b}{\partial t} + \frac{\partial}{\partial x}\int_{z_\mathrm{b}}^{z_\mathrm{f}}(\rho u w)\,\mathrm{d}z - \rho_\mathrm{f}u_\mathrm{f}w_\mathrm{f}\frac{\partial z_\mathrm{f}}{\partial x} + \rho_\mathrm{b}u_\mathrm{b}w_\mathrm{b}\frac{\partial z_\mathrm{b}}{\partial x} \\ &\qquad +\rho_\mathrm{f}w_\mathrm{f}^2 - \rho_\mathrm{b}w_\mathrm{b}^2 + p_\mathrm{f} - p_\mathrm{b} = -g\cos\theta\int_{z_\mathrm{b}}^{z_\mathrm{f}}\rho\,\mathrm{d}z \\ \therefore\quad &\frac{\partial}{\partial t}\int_{z_\mathrm{b}}^{z_\mathrm{f}}(\rho w)\,\mathrm{d}z + \frac{\partial}{\partial x}\int_{z_\mathrm{b}}^{z_\mathrm{f}}(\rho u w)\,\mathrm{d}z - \rho_\mathrm{f}w_\mathrm{f}\left(\frac{\partial z_\mathrm{f}}{\partial t} + u_\mathrm{f}\frac{\partial z_\mathrm{f}}{\partial x} - w_\mathrm{f}\right) \\ &\qquad +\rho_\mathrm{b}w_\mathrm{b}\left(\frac{\partial z_b}{\partial t} + u_\mathrm{b}\frac{\partial z_\mathrm{b}}{\partial x} - w_\mathrm{b}\right) + p_\mathrm{f} - p_\mathrm{b} = -g\cos\theta\int_{z_\mathrm{b}}^{z_\mathrm{f}}\rho\,\mathrm{d}z.\end{aligned} \tag{2.28}$$

Using this formula and the kinematic conditions (2.12) and (2.14), we write

$$\frac{\partial}{\partial t}\int_{z_\mathrm{b}}^{z_\mathrm{f}}(\rho w)\,\mathrm{d}z + \frac{\partial}{\partial x}\int_{z_\mathrm{b}}^{z_\mathrm{f}}(\rho u w)\,\mathrm{d}z + p_\mathrm{f} - p_\mathrm{b} = -g\cos\theta\int_{z_\mathrm{b}}^{z_\mathrm{f}}\rho\,\mathrm{d}z. \tag{2.29}$$

We introduce the straightforward definitions of the depth-averaged z momentum and z-momentum flux:

$$\overline{\rho w} \equiv \frac{1}{h}\int_{z_\mathrm{b}}^{z_\mathrm{f}}(\rho w)\,\mathrm{d}z \quad , \qquad \overline{\rho u w} \equiv \frac{1}{h}\int_{z_\mathrm{b}}^{z_\mathrm{f}}(\rho u w)\,\mathrm{d}z. \tag{2.30}$$

Using these and Eqs. (2.13) and (2.20), we rewrite Eq. (2.29) as

$$\frac{\partial}{\partial t}(\overline{\rho w}h) + \frac{\partial}{\partial x}(\overline{\rho u w}h) + p_\mathrm{f} - p_\mathrm{b} = -\overline{\rho} g h \cos\theta. \tag{2.31}$$

Energy conservation equation

The energy conservation Eq. (2.4) is integrated from $z = z_\mathrm{b}(x,t)$ to $z = z_\mathrm{f}(x,t)$ to yield

$$\begin{aligned}\int_{z_\mathrm{b}}^{z_\mathrm{f}} \frac{\partial}{\partial t}(\rho e_\mathrm{tot})\,\mathrm{d}z + \int_{z_\mathrm{b}}^{z_\mathrm{f}} \frac{\partial}{\partial x}(\rho e_\mathrm{tot} u + pu)\,\mathrm{d}z \\ + \rho_\mathrm{f} e_{\mathrm{tot,f}} w_\mathrm{f} - \rho_\mathrm{b} e_{\mathrm{tot,b}} w_\mathrm{b} + p_\mathrm{f} w_\mathrm{f} - p_\mathrm{b} w_\mathrm{b} = 0.\end{aligned} \tag{2.32}$$

Applying Leibniz's rule (2.16) to Eq. (2.32), we obtain

$$\begin{aligned}&\frac{\partial}{\partial t}\int_{z_\mathrm{b}}^{z_\mathrm{f}} (\rho e_\mathrm{tot})\,\mathrm{d}z - \rho_\mathrm{f} e_{\mathrm{tot,f}} \frac{\partial z_\mathrm{f}}{\partial t} + \rho_\mathrm{b} e_{\mathrm{tot,b}} \frac{\partial z_\mathrm{b}}{\partial t} \\ &\quad + \frac{\partial}{\partial x}\int_{z_\mathrm{b}}^{z_\mathrm{f}} (\rho e_\mathrm{tot} u)\,\mathrm{d}z - \rho_\mathrm{f} e_{\mathrm{tot,f}} u_\mathrm{f} \frac{\partial z_\mathrm{f}}{\partial x} + \rho_\mathrm{b} e_{\mathrm{tot,b}} u_\mathrm{b} \frac{\partial z_\mathrm{b}}{\partial x} \\ &\quad + \frac{\partial}{\partial x}\int_{z_\mathrm{b}}^{z_\mathrm{f}} (pu)\,\mathrm{d}z - p_\mathrm{f} u_\mathrm{f} \frac{\partial z_\mathrm{f}}{\partial x} + p_\mathrm{b} u_\mathrm{b} \frac{\partial z_\mathrm{b}}{\partial x} \\ &\quad + \rho_\mathrm{f} e_{\mathrm{tot,f}} w_\mathrm{f} - \rho_\mathrm{b} e_{\mathrm{tot,b}} w_\mathrm{b} + p_\mathrm{f} w_\mathrm{f} - p_\mathrm{b} w_\mathrm{b} = 0 \\ \therefore\quad &\frac{\partial}{\partial t}\int_{z_\mathrm{b}}^{z_\mathrm{f}} (\rho e_\mathrm{tot})\,\mathrm{d}z + \frac{\partial}{\partial x}\int_{z_\mathrm{b}}^{z_\mathrm{f}} (\rho e_\mathrm{tot} u)\,\mathrm{d}z + \frac{\partial}{\partial x}\int_{z_\mathrm{b}}^{z_\mathrm{f}} (pu)\,\mathrm{d}z \\ &\quad - \rho_\mathrm{f} e_{\mathrm{tot,f}} \left(\frac{\partial z_\mathrm{f}}{\partial t} + u_\mathrm{f}\frac{\partial z_\mathrm{f}}{\partial x} - w_\mathrm{f}\right) + \rho_\mathrm{b} e_{\mathrm{tot,b}} \left(\frac{\partial z_\mathrm{b}}{\partial t} + u_\mathrm{b}\frac{\partial z_\mathrm{b}}{\partial x} - w_\mathrm{b}\right) \\ &\quad - p_\mathrm{f}\left(u_\mathrm{f}\frac{\partial z_\mathrm{f}}{\partial x} - w_\mathrm{f}\right) + p_\mathrm{b}\left(u_\mathrm{b}\frac{\partial z_\mathrm{b}}{\partial x} - w_\mathrm{b}\right) = 0.\end{aligned} \tag{2.33}$$

Using this formula and the kinematic conditions (2.12) and (2.14), we write

$$\frac{\partial}{\partial t}\int_{z_\mathrm{b}}^{z_\mathrm{f}} (\rho e_\mathrm{tot})\,\mathrm{d}z + \frac{\partial}{\partial x}\int_{z_\mathrm{b}}^{z_\mathrm{f}} (\rho e_\mathrm{tot} u)\,\mathrm{d}z + \frac{\partial}{\partial x}\int_{z_\mathrm{b}}^{z_\mathrm{f}} (pu)\,\mathrm{d}z + p_\mathrm{f}\frac{\partial z_\mathrm{f}}{\partial t} - p_\mathrm{b}\frac{\partial z_\mathrm{b}}{\partial t} = 0. \tag{2.34}$$

We introduce the straightforward definitions of the depth-averaged total energy and total energy fluxes:

$$\overline{\rho e_{\rm tot}} \equiv \frac{1}{h}\int_{z_{\rm b}}^{z_{\rm f}} (\rho e_{\rm tot})\,{\rm d}z, \quad \overline{\rho e_{\rm tot} u} \equiv \frac{1}{h}\int_{z_{\rm b}}^{z_{\rm f}} (\rho e_{\rm tot} u)\,{\rm d}z, \quad \overline{pu} \equiv \frac{1}{h}\int_{z_{\rm b}}^{z_{\rm f}} (pu)\,{\rm d}z. \tag{2.35}$$

Using these and Eqs. (2.13), we rewrite Eq. (2.34) as

$$\frac{\partial}{\partial t}(\overline{\rho e_{\rm tot}} h) + \frac{\partial}{\partial x}(\overline{\rho e_{\rm tot} u} h) + \frac{\partial}{\partial x}(\overline{pu} h) + p_{\rm f}\frac{\partial z_{\rm f}}{\partial t} - p_{\rm b}\frac{\partial z_{\rm b}}{\partial t} = 0. \tag{2.36}$$

By using Eq. (2.5), I divide the depth-averaged total energy $\overline{\rho e_{\rm tot}}$ and total energy flux $\overline{\rho e_{\rm tot} u}$ in Eq. (2.36) into three components, associated with the internal energy, the kinetic energy, and the potential energy. The product of the total energy $e_{\rm tot}$ in Eq. (2.5) and the density $\rho(x,z,t)$ is integrated from $z = z_{\rm b}(x,t)$ to $z = z_{\rm f}(x,t)$ to yield

$$\begin{aligned}\int_{z_{\rm b}}^{z_{\rm f}} (\rho e_{\rm tot})\,{\rm d}z &= \int_{z_{\rm b}}^{z_{\rm f}} (\rho e)\,{\rm d}z + \frac{1}{2}\int_{z_{\rm b}}^{z_{\rm f}} \left(\rho(u^2+w^2)\right)\,{\rm d}z \\ &\quad + g\cos\theta \int_{z_{\rm b}}^{z_{\rm f}} (\rho z)\,{\rm d}z - gx\sin\theta\int_{z_{\rm b}}^{z_{\rm f}} \rho\,{\rm d}z. \end{aligned} \tag{2.37}$$

The product of the total energy $e_{\rm tot}$, the density $\rho(x,z,t)$ and the velocity $u(x,z,t)$ is integrated from $z = z_{\rm b}(x,t)$ to $z = z_{\rm f}(x,t)$ to yield

$$\begin{aligned}\int_{z_{\rm b}}^{z_{\rm f}} (\rho e_{\rm tot} u)\,{\rm d}z &= \int_{z_{\rm b}}^{z_{\rm f}} (\rho e u)\,{\rm d}z + \frac{1}{2}\int_{z_{\rm b}}^{z_{\rm f}} \left(\rho(u^2+w^2)u\right)\,{\rm d}z \\ &\quad + g\cos\theta \int_{z_{\rm b}}^{z_{\rm f}} (\rho z u)\,{\rm d}z - gx\sin\theta\int_{z_{\rm b}}^{z_{\rm f}} (\rho u)\,{\rm d}z. \end{aligned} \tag{2.38}$$

We introduce the straightforward definitions of the depth-averaged values:

$$\begin{aligned}
&\overline{\rho e} \equiv \frac{1}{h}\int_{z_\mathrm{b}}^{z_\mathrm{f}} (\rho e)\,\mathrm{d}z\ , \quad \overline{\rho e u} \equiv \frac{1}{h}\int_{z_\mathrm{b}}^{z_\mathrm{f}} (\rho e u)\,\mathrm{d}z\ , \\
&\overline{\rho w^2} \equiv \frac{1}{h}\int_{z_\mathrm{b}}^{z_\mathrm{f}} (\rho w^2)\,\mathrm{d}z\ , \quad \overline{\rho u^3} \equiv \frac{1}{h}\int_{z_\mathrm{b}}^{z_\mathrm{f}} (\rho u^3)\,\mathrm{d}z\ , \quad \overline{\rho u w^2} \equiv \frac{1}{h}\int_{z_\mathrm{b}}^{z_\mathrm{f}} (\rho u w^2)\,\mathrm{d}z\ , \\
&\overline{\rho z} \equiv \frac{1}{h}\int_{z_\mathrm{b}}^{z_\mathrm{f}} (\rho z)\,\mathrm{d}z\ , \quad \overline{\rho z u} \equiv \frac{1}{h}\int_{z_\mathrm{b}}^{z_\mathrm{f}} (\rho z u)\,\mathrm{d}z.
\end{aligned} \tag{2.39}$$

Using these and Eqs. (2.13), (2.20), (2.25) and (2.35), we rewrite Eqs. (2.37) and (2.38) as

$$\overline{\rho e_\mathrm{tot}} = \overline{\rho e} + \frac{1}{2}(\overline{\rho u^2} + \overline{\rho w^2}) + \overline{\rho z} g\cos\theta - \overline{\rho} x g \sin\theta \tag{2.40}$$

and

$$\overline{\rho e_\mathrm{tot} u} = \overline{\rho e u} + \frac{1}{2}(\overline{\rho u^3} + \overline{\rho u w^2}) + \overline{\rho z u} g\cos\theta - \overline{\rho u} x g \sin\theta, \tag{2.41}$$

respectively. Substituting Eqs. (2.40) and (2.41) into Eq. (2.36), we obtain

$$\begin{aligned}
&\frac{\partial}{\partial t}\left(\overline{\rho e}h + \frac{1}{2}\overline{\rho u^2}h + \frac{1}{2}\overline{\rho w^2}h + \overline{\rho z} g h\cos\theta - \overline{\rho} x g h \sin\theta\right) \\
&\quad + \frac{\partial}{\partial x}\left(\overline{\rho e u}h + \frac{1}{2}\overline{\rho u^3}h + \frac{1}{2}\overline{\rho u w^2}h + \overline{\rho z u} g h\cos\theta - \overline{\rho u} x g h \sin\theta\right) \\
&\quad + \frac{\partial}{\partial x}(\overline{p u}h) + p_\mathrm{f}\frac{\partial z_\mathrm{f}}{\partial t} - p_\mathrm{b}\frac{\partial z_\mathrm{b}}{\partial t} = 0.
\end{aligned} \tag{2.42}$$

2.1.4 Shallow-water assumption

By applying the shallow-water assumption that the z component of acceleration is negligible to the depth-integrated z-momentum conservation Eq. (2.31), we derive the depth-averaged hydrostatic pressure and the associated expressions. Subsequently, we apply these to the depth-integrated x-momentum conservation Eq. (2.26) and the depth-integrated energy conservation Eq. (2.42) to derive the system of the shallow-water equations.

We introduce the shallow-water assumption that the z component of acceleration is negligible (i.e., $\frac{\partial}{\partial t}(\overline{\rho w}h) + \frac{\partial}{\partial x}(\overline{\rho u w}h) = 0$). Insertion of this condition into the depth-integrated z-momentum conservation Eq. (2.31) gives

$$p_{\mathrm{f}} - p_{\mathrm{b}} = -\overline{\rho} g h \cos\theta. \tag{2.43}$$

This is the same as the depth integration of

$$\frac{\partial p}{\partial z} = -\rho g \cos\theta, \tag{2.44}$$

which is obtained from the z-momentum conservation Eq. (2.3) with the shallow-water assumption (i.e., $\frac{\partial}{\partial t}(\rho w) + \frac{\partial}{\partial x}(\rho u w) + \frac{\partial}{\partial z}(\rho w^2) = 0$).

By using Eqs. (2.43) and (2.44), we derive the depth-averaged hydrostatic pressure and the associated expressions. The depth-averaged thermodynamic pressure $\overline{p}$ in Eq. (2.25) can be rewritten as

$$\begin{aligned}
\overline{p} &\equiv \frac{1}{h}\int_{z_{\mathrm{b}}}^{z_{\mathrm{f}}} p \, \mathrm{d}z \\
&= \frac{1}{h}\int_{z_{\mathrm{b}}}^{z_{\mathrm{f}}} \left(p \frac{\mathrm{d}z}{\mathrm{d}z} \right) \, \mathrm{d}z \\
&= \frac{1}{h}\left(z_{\mathrm{f}} p_{\mathrm{f}} - z_{\mathrm{b}} p_{\mathrm{b}} - \int_{z_{\mathrm{b}}}^{z_{\mathrm{f}}} \left(z \frac{\partial p}{\partial z} \right) \, \mathrm{d}z \right).
\end{aligned} \tag{2.45}$$

Applying Eq. (2.44) to Eq. (2.45), we obtain

$$\begin{aligned}
\overline{p} &= \frac{1}{h}\left(z_{\mathrm{f}} p_{\mathrm{f}} - z_{\mathrm{b}} p_{\mathrm{b}} + \int_{z_{\mathrm{b}}}^{z_{\mathrm{f}}} (\rho g z \cos\theta) \, \mathrm{d}z \right) \\
&= \frac{1}{h}\left(z_{\mathrm{f}} p_{\mathrm{f}} - z_{\mathrm{b}} p_{\mathrm{b}} + g\cos\theta \int_{z_{\mathrm{b}}}^{z_{\mathrm{f}}} (\rho z) \, \mathrm{d}z \right).
\end{aligned} \tag{2.46}$$

Using Eq. (2.39), we rewrite Eq. (2.46) as

$$\overline{p} = \frac{1}{h}\left(z_{\mathrm{f}} p_{\mathrm{f}} - z_{\mathrm{b}} p_{\mathrm{b}} + \overline{\rho z} g h \cos\theta \right). \tag{2.47}$$

We use Eq. (2.43) to eliminate p_{b} from Eq. (2.47) and obtain

$$\begin{aligned}\overline{p} &= \frac{1}{h}\left(p_{\mathrm{f}}h + (\overline{\rho z} - \overline{\rho} z_{\mathrm{b}})gh\cos\theta\right) \\ &= p_{\mathrm{f}} + (\overline{\rho z} - \overline{\rho} z_{\mathrm{b}})g\cos\theta. \end{aligned} \tag{2.48}$$

Considering $\overline{\rho z} = \bar{\rho}\bar{z}$, we obtain

$$\bar{p} = p_{\mathrm{f}} + \bar{\rho}(\bar{z} - z_{\mathrm{b}})g\cos\theta. \tag{2.49}$$

Introducing the straightforward definitions of the depth-averaged height:

$$\overline{z} \equiv \frac{1}{h}\int_{z_{\mathrm{b}}}^{z_{\mathrm{f}}} z\,\mathrm{d}z = \frac{1}{h}\left[\frac{z^2}{2}\right]_{z_{\mathrm{b}}}^{z_{\mathrm{f}}} = \frac{1}{h}\frac{z_{\mathrm{f}}^2 - z_{\mathrm{b}}^2}{2} = \frac{h}{2} + z_{\mathrm{b}} \quad (\because \text{ Eq. (2.13)}), \tag{2.50}$$

we rewrite Eq. (2.49) as

$$\bar{p} = p_{\mathrm{f}} + \frac{1}{2}\bar{\rho}gh\cos\theta. \tag{2.51}$$

Considering that the density of the ambient fluid is the constant ρ_{a}, we can write the hydrostatic pressure of the ambient fluid p_{a} as

$$p_{\mathrm{a}}(x, z) = p_{\mathrm{a0}} + \rho_{\mathrm{a}}gx\sin\theta - \rho_{\mathrm{a}}gz\cos\theta, \tag{2.52}$$

where p_{a0} is a constant hydrostatic pressure of the ambient fluid at the reference point ($x = 0, z = 0$); see Figure 2.2. Using Eq. (2.52), p_{f} in Eq. (2.51) is represented as

$$\begin{aligned} p_{\mathrm{f}} &\equiv p_{\mathrm{a}}(x, z = z_{\mathrm{f}}) + \Delta p_{\mathrm{f}} \\ &= p_{\mathrm{a0}} + \rho_{\mathrm{a}}gx\sin\theta - \rho_{\mathrm{a}}gz_{\mathrm{f}}\cos\theta + \Delta p_{\mathrm{f}} \quad (\because \text{ Eq. (2.52)}) \\ &= p_{\mathrm{a0}} + \rho_{\mathrm{a}}gx\sin\theta - \rho_{\mathrm{a}}g(h + z_{\mathrm{b}})\cos\theta + \Delta p_{\mathrm{f}} \quad (\because \text{ Eq. (2.13)}), \end{aligned} \tag{2.53}$$

where Δp_f is the pressure difference at $z = z_\mathrm{f}$ between the current and the ambient fluid; in general, $\Delta p_\mathrm{f} = 0$ (Figure 2.2).

In the following, the above expressions with the shallow-water assumption are applied to the depth-integrated x-momentum conservation Eq. (2.26) and the depth-integrated energy conservation Eq. (2.42) to derive the system of the shallow-water equations.

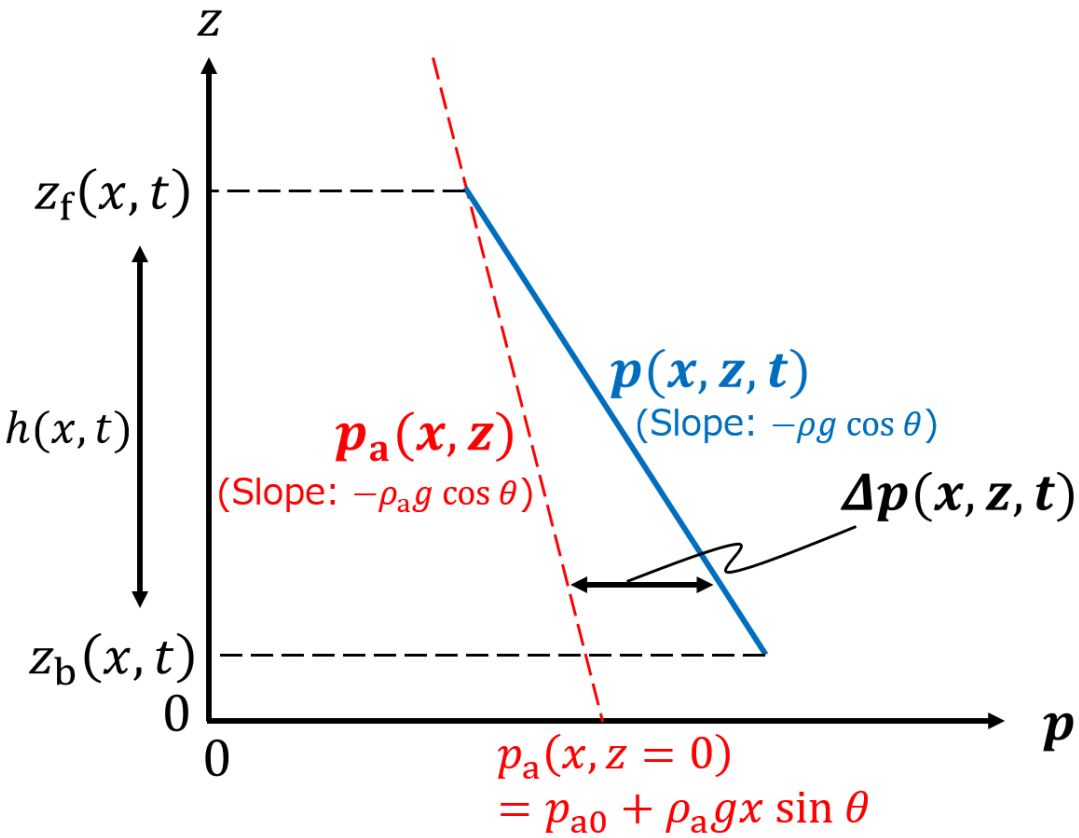

Figure 2.2: Schematic illustration of the current hydrostatic pressure $p(x,z,t)$, the ambient hydrostatic pressure $p_\mathrm{a}(x,z)$, and the pressure difference $\Delta p(x,z,t)$, under the shallow-water assumption.

Momentum conservation equation in the x direction

We use Eq. (2.43) to eliminate p_b from the depth-integrated x-momentum conservation Eq. (2.26) and obtain

$$\begin{aligned}
&\frac{\partial}{\partial t}(\overline{\rho u}h) + \frac{\partial}{\partial x}(\overline{\rho u^2}h + \overline{p}h) - p_\mathrm{f}\frac{\partial z_\mathrm{f}}{\partial x} + (p_\mathrm{f} + \overline{\rho}gh\cos\theta)\frac{\partial z_\mathrm{b}}{\partial x} = \overline{\rho}gh\sin\theta \\
\therefore\quad &\frac{\partial}{\partial t}(\overline{\rho u}h) + \frac{\partial}{\partial x}(\overline{\rho u^2}h + \overline{p}h) - p_\mathrm{f}\frac{\partial h}{\partial x} + \overline{\rho}gh\cos\theta\frac{\partial z_\mathrm{b}}{\partial x} = \overline{\rho}gh\sin\theta. \qquad (2.54)
\end{aligned}$$

We substitute Eq. (2.51) into Eq. (2.54) to eliminate $\overline{p}$ and obtain

$$\begin{aligned}
&\frac{\partial}{\partial t}(\bar{\rho}\bar{u}h) + \frac{\partial}{\partial x}\left(\bar{\rho}\bar{u}^2h + \left(p_\mathrm{f} + \frac{1}{2}\bar{\rho}gh\cos\theta\right)h\right) - p_\mathrm{f}\frac{\partial h}{\partial x} + \bar{\rho}gh\cos\theta\frac{\partial z_\mathrm{b}}{\partial x} = \bar{\rho}gh\sin\theta \\
\therefore\quad &\frac{\partial}{\partial t}(\bar{\rho}\bar{u}h) + \frac{\partial}{\partial x}\left(\bar{\rho}\bar{u}^2h + \frac{1}{2}\bar{\rho}gh^2\cos\theta\right) + h\frac{\partial p_\mathrm{f}}{\partial x} + \bar{\rho}gh\cos\theta\frac{\partial z_\mathrm{b}}{\partial x} = \bar{\rho}gh\sin\theta. \qquad (2.55)
\end{aligned}$$

Furthermore, we substitute Eq. (2.53) into Eq. (2.55) to eliminate p_f and obtain

$$\begin{aligned}
&\frac{\partial}{\partial t}(\bar{\rho}\bar{u}h) + \frac{\partial}{\partial x}\left(\bar{\rho}\bar{u}^2h + \frac{1}{2}\bar{\rho}gh^2\cos\theta\right) \\
&\qquad + h\frac{\partial}{\partial x}\left(p_{\mathrm{a}0} + \rho_\mathrm{a}gx\sin\theta - \rho_\mathrm{a}g(h + z_\mathrm{b})\cos\theta + \Delta p_\mathrm{f}\right) \\
&\qquad + \bar{\rho}gh\cos\theta\frac{\partial z_\mathrm{b}}{\partial x} = \bar{\rho}gh\sin\theta \\
\therefore\quad &\frac{\partial}{\partial t}(\bar{\rho}\bar{u}h) + \frac{\partial}{\partial x}\left(\bar{\rho}\bar{u}^2h + \frac{1}{2}(\bar{\rho} - \rho_\mathrm{a})gh^2\cos\theta\right) \\
&\qquad = (\bar{\rho} - \rho_\mathrm{a})gh\sin\theta - (\bar{\rho} - \rho_\mathrm{a})gh\cos\theta\frac{\partial z_\mathrm{b}}{\partial x} - h\frac{\partial}{\partial x}(\Delta p_\mathrm{f}), \qquad (2.56)
\end{aligned}$$

where $\Delta p_\mathrm{f} = 0$ in general (Figure 2.2).

Energy conservation equation

We substitute Eq. (2.43) into the depth-integrated energy conservation Eq. (2.42) to obtain

$$\begin{aligned}
&\frac{\partial}{\partial t}\left(\overline{\rho e}h+\frac{1}{2}\overline{\rho u^2}h+\overline{\rho z}gh\cos\theta-\overline{\rho}xgh\sin\theta\right)\\
&\quad+\frac{\partial}{\partial x}\left(\overline{\rho e u}h+\frac{1}{2}\overline{\rho u^3}h+\overline{\rho z u}gh\cos\theta-\overline{\rho u}xgh\sin\theta\right)\\
&\quad+\frac{\partial}{\partial x}(\overline{p u}h)+p_{\mathrm{f}}\frac{\partial z_{\mathrm{f}}}{\partial t}-(p_{\mathrm{f}}+\overline{\rho}gh\cos\theta)\frac{\partial z_{\mathrm{b}}}{\partial t}=0\\
\therefore\quad&\frac{\partial}{\partial t}\left(\overline{\rho e}h+\frac{1}{2}\overline{\rho u^2}h+\overline{\rho z}gh\cos\theta-\overline{\rho}xgh\sin\theta\right)\\
&\quad+\frac{\partial}{\partial x}\left(\overline{\rho e u}h+\frac{1}{2}\overline{\rho u^3}h+\overline{\rho z u}gh\cos\theta-\overline{\rho u}xgh\sin\theta\right)\\
&\quad+\frac{\partial}{\partial x}(\overline{p u}h)+p_{\mathrm{f}}\frac{\partial h}{\partial t}-\overline{\rho}gh\cos\theta\frac{\partial z_{\mathrm{b}}}{\partial t}=0,
\end{aligned}\tag{2.57}$$

where the z component of kinetic energy is negligible (i.e., $\frac{\partial}{\partial t}(\frac{1}{2}\overline{\rho w}^2h)+\frac{\partial}{\partial x}(\frac{1}{2}\overline{\rho u w^2}h)=0$). We substitute Eq. (2.51) into Eq. (2.57) to eliminate p_{f} and obtain

$$\begin{aligned}
&\frac{\partial}{\partial t}\left(\bar{\rho}\bar{e}h+\frac{1}{2}\bar{\rho}\bar{u}^2h+\bar{\rho}\bar{z}gh\cos\theta-\bar{\rho}xgh\sin\theta\right)\\
&\quad+\frac{\partial}{\partial x}\left(\bar{\rho}\bar{e}\bar{u}h+\frac{1}{2}\bar{\rho}\bar{u}^3h+\bar{\rho}\bar{z}\bar{u}gh\cos\theta-\bar{\rho}\bar{u}xgh\sin\theta\right)\\
&\quad+\frac{\partial}{\partial x}(\bar{p}\bar{u}h)+\left(\bar{p}-\frac{1}{2}\bar{\rho}gh\cos\theta\right)\frac{\partial h}{\partial t}-\bar{\rho}gh\cos\theta\frac{\partial z_{\mathrm{b}}}{\partial t}=0.
\end{aligned}\tag{2.58}$$

Using Eq. (2.50), we can rewrite Eq. (2.58) as

$$\begin{aligned}
&\frac{\partial}{\partial t}\left(\bar{\rho}\bar{e}h+\frac{1}{2}\bar{\rho}\bar{u}^2h+\bar{\rho}\left(\frac{h}{2}+z_{\mathrm{b}}\right)gh\cos\theta-\bar{\rho}xgh\sin\theta\right)\\
&\quad+\frac{\partial}{\partial x}\left(\bar{\rho}\bar{e}\bar{u}h+\frac{1}{2}\bar{\rho}\bar{u}^3h+\bar{\rho}\left(\frac{h}{2}+z_{\mathrm{b}}\right)\bar{u}gh\cos\theta-\bar{\rho}\bar{u}xgh\sin\theta\right)\\
&\quad+\frac{\partial}{\partial x}(\bar{p}\bar{u}h)+\left(\bar{p}-\frac{1}{2}\bar{\rho}gh\cos\theta\right)\frac{\partial h}{\partial t}-\bar{\rho}gh\cos\theta\frac{\partial z_{\mathrm{b}}}{\partial t}=0.
\end{aligned}\tag{2.59}$$

2.1.5 Treatment of the depth-averaged thermodynamic pressure $\bar{p}$

In the derivation processes of the momentum and energy conservation Eqs. (2.56) and (2.59), the depth-averaged thermodynamic pressure in the current, $\bar{p}$, is a function depending on variables such as $h(x,t)$ (i.e., Eqs. (2.51) and (2.53)). On the other hand, Bursik & Woods (1996) assume that $\bar{p}$ is a constant atmospheric pressure only in the equations of energy and state. In this subsection, we investigate how the system of the shallow-water equations is affected by this difference for the treatment of $\bar{p}$ (while, in the next section, $\bar{p}$ in the two-layer PDC model will be fixed at a constant atmospheric pressure, in the same way as Bursik & Woods' formula).

We consider a simple case where $\theta = 0$ and $z_{\rm b} = 0$, in this subsection. Then, the momentum conservation Eq. (2.56) is reduced to

$$\frac{\partial}{\partial t}(\bar{\rho}\bar{u}h) + \frac{\partial}{\partial x}\left(\bar{\rho}\bar{u}^2 h + \frac{\bar{\rho}-\rho_{\rm a}}{2}gh^2\right) = 0. \tag{2.60}$$

The energy conservation Eq. (2.59) is also reduced to

$$\begin{aligned}\frac{\partial}{\partial t}\left(\bar{\rho}C_{\rm v}\bar{T}h + \frac{1}{2}\bar{\rho}\bar{u}^2 h + \frac{1}{2}\bar{\rho}gh^2\right) + \frac{\partial}{\partial x}\left(\bar{\rho}C_{\rm v}\bar{T}\bar{u}h + \frac{1}{2}\bar{\rho}\bar{u}^3 h + \frac{1}{2}\bar{\rho}\bar{u}gh^2 + \bar{p}\bar{u}h\right) \\ + \left(\bar{p} - \frac{1}{2}\bar{\rho}gh\right)\frac{\partial h}{\partial t} = 0,\end{aligned} \tag{2.61}$$

where $\bar{e} = C_{\rm v}\bar{T}$ from Eq. (2.7) since the heat capacity at constant volume $C_{\rm v}$ is constant. Use of the momentum conservation Eq. (2.60) and the mass conservation Eq. (2.21) and some algebra rewrite the energy conservation Eq. (2.61) as

$$\frac{\partial}{\partial t}\left(\bar{\rho}C_{\rm v}\bar{T}h\right) + \frac{\partial}{\partial x}\left(\bar{\rho}C_{\rm v}\bar{T}\bar{u}h\right) + \bar{p}\left(\frac{\partial h}{\partial t} + \frac{\partial}{\partial x}(\bar{u}h)\right) = 0 \tag{2.62}$$

(see Subsection 2.1.7 for the details of the algebra). Furthermore, we substitute the ther-

mal equation of state (2.6) into Eq. (2.62) to obtain

$$\begin{aligned} & \frac{\partial}{\partial t}\left(C_{\mathrm{v}}\frac{\bar{p}}{R}h\right)+\frac{\partial}{\partial x}\left(C_{\mathrm{v}}\frac{\bar{p}}{R}\bar{u}h\right)+\bar{p}\left(\frac{\partial h}{\partial t}+\frac{\partial}{\partial x}(\bar{u}h)\right)=0 \\ \therefore \quad & \frac{\partial}{\partial t}\left(\frac{\bar{p}}{\gamma-1}h\right)+\frac{\partial}{\partial x}\left(\frac{\bar{p}}{\gamma-1}\bar{u}h\right)+\bar{p}\left(\frac{\partial h}{\partial t}+\frac{\partial}{\partial x}(\bar{u}h)\right)=0 \qquad (\because \text{ Eq. (2.9)}), \end{aligned} \tag{2.63}$$

where $\gamma(\equiv C_{\mathrm{p}}/C_{\mathrm{v}})$ is the ratio of the specific heats. We consider the two cases for the treatment of the depth-averaged thermodynamic pressure $\bar{p}$:

$$\bar{p}=\begin{cases} p_{\mathrm{a}0}-\rho_{\mathrm{a}}gh+\frac{1}{2}\bar{\rho}gh \\ p_{\mathrm{a}0}(=\text{const}), \end{cases} \tag{2.64}$$

where $p_{\mathrm{a}0}$ is a constant hydrostatic pressure of the ambient fluid at the reference point ($x=0, z=0$); see Figure 2.2. The variable-type $\bar{p}$ (i.e., the first expression in Eq. (2.64)) is obtained in the derivation processes of the momentum and energy conservation Eqs. (2.56) and (2.59). The constant-type $\bar{p}$ (i.e., the second expression in Eq. (2.64)) is a simplified version of the variable-type $\bar{p}$. Thus, we have the four Eqs. (2.21), (2.60), (2.63) and (2.64) for the four unknowns (h, $\bar{\rho}$, $\bar{u}$ and $\bar{p}$).

Firstly, we consider the case using the constant-type $\bar{p}$ (i.e., the second expression in Eq. (2.64)). In this case, Eq. (2.63) is reduced to

$$\begin{aligned} & \frac{\partial}{\partial t}\left(\frac{\gamma\bar{p}}{\gamma-1}h\right)+\frac{\partial}{\partial x}\left(\frac{\gamma\bar{p}}{\gamma-1}\bar{u}h\right)=0 \\ \therefore \quad & \frac{\partial h}{\partial t}+\frac{\partial}{\partial x}\left(\bar{u}h\right)=0. \end{aligned} \tag{2.65}$$

Use of this and the mass conservation Eq. (2.21) gives $\bar{\rho}(x,t)=$ const if $\bar{\rho}(x,t=0)=$ const. On the other hand, in the case using the variable-type $\bar{p}$ (i.e., the first expression in Eq. (2.64)), $\bar{\rho}(x,t)\neq$ const even if $\bar{\rho}(x,t=0)=$ const. Thus, using the variable-type $\bar{p}$ makes the system of shallow-water equations complicated. We note that the variable-type

$\bar{p}$ can be approximated by the constant-type $\bar{p}$ when $h \ll p_{\mathrm{a}0}/(|\bar{\rho}/2 - \rho_{\mathrm{a}}|g)$.

2.1.6 Front condition

At the flow front $x = x_{\mathrm{N}}(t)$ (see Figure 2.1), the kinematic condition (2.15): $\mathrm{d}x_{\mathrm{N}}/\mathrm{d}t = u_{\mathrm{N}}$ and the mass, momentum and energy conservation equations should be taken into account. In addition, to describe realistic gravity current dynamics, we must consider a quasi-steady balance between the buoyancy pressure driving the current front ($\sim (\bar{\rho}_{\mathrm{N}} - \rho_{\mathrm{a}})gh_{\mathrm{N}}\cos\theta$) and the resistance pressure caused by the acceleration of the ambient fluid around the front ($\sim \rho_{\mathrm{a}}\bar{u}_{\mathrm{N}}^2$), because the flow front is affected by the resistance of the ambient fluid. This condition is known as the front condition, and can be written as follows (e.g., Ungarish 2007):

$$\frac{\rho_{\mathrm{a}}\bar{u}_{\mathrm{N}}^2}{(\bar{\rho}_{\mathrm{N}} - \rho_{\mathrm{a}})gh_{\mathrm{N}}\cos\theta} = Fr_{\mathrm{N}0}^2$$
$$\therefore \quad \bar{u}_{\mathrm{N}} = Fr_{\mathrm{N}0}\sqrt{\frac{\bar{\rho}_{\mathrm{N}}}{\rho_{\mathrm{a}}}}\sqrt{\frac{\bar{\rho}_{\mathrm{N}} - \rho_{\mathrm{a}}}{\bar{\rho}_{\mathrm{N}}}gh_{\mathrm{N}}\cos\theta} \tag{2.66}$$

where $Fr_{\mathrm{N}0}$, which is an imposed frontal Froude number in a Boussinesq system (i.e., $\bar{\rho}_{\mathrm{N}}/\rho_{\mathrm{a}} \approx 10^0$), is assumed to be a constant of order 10^0. Inviscid theory suggests $Fr_{\mathrm{N}0} = \sqrt{2}$ (Benjamin, 1968). On the other hand, $Fr_{\mathrm{N}0}$ was experimentally evaluated by Huppert & Simpson (1980) to be 1.19 and by Marino et al. (2005) to be 0.87.

2.1.7 Summary of Section 2.1

We summarize the system of the generalized one-layer shallow-water equations derived in Section 2.1. There are six unknown variables (depth h, density $\bar{\rho}$, velocity $\bar{u}$, internal energy $\bar{e}$, temperature $\bar{T}$, and thermodynamic pressure $\bar{p}$) in the six equations (the mass, momentum and energy conservation equations, the thermal equation of state, the caloric equation of state, and the equation associated with the thermodynamic pressure). At the flow front, the front condition is solved to describe realistic gravity current dynamics.

Mass conservation equation

Form Eq. (2.21), the mass conservation equation is written as

$$\frac{\partial}{\partial t}(\bar{\rho}h) + \frac{\partial}{\partial x}(\bar{\rho}\bar{u}h) = \dot{M}_a, \tag{2.67}$$

where $\dot{M}_a$ is the rate of change of the mass due to physical processes such as entrainment of ambient fluid.

Momentum conservation equation

From Eq. (2.56), the momentum conservation equation is written as

$$\begin{aligned}\frac{\partial}{\partial t}(\bar{\rho}\bar{u}h) + \frac{\partial}{\partial x}\left(\bar{\rho}\bar{u}^2 h + \frac{\bar{\rho}-\rho_{\mathrm{a}}}{2}gh^2\cos\theta\right)& \\ -(\bar{\rho}-\rho_{\mathrm{a}})gh\sin\theta + (\bar{\rho}-\rho_{\mathrm{a}})gh\cos\theta\frac{\partial z_{\mathrm{b}}}{\partial x} + h\frac{\partial}{\partial x}(\Delta p_{\mathrm{f}}) = \dot{M}_o,&\end{aligned} \tag{2.68}$$

where $\dot{M}_o$ is the rate of change of the momentum due to physical processes such as basal drag. Δp_{f} is 0 in general (Figure 2.2).

Energy conservation equation

From Eq. (2.59), the energy conservation equation is written as

$$\begin{aligned}&\frac{\partial}{\partial t}\left(\bar{\rho}\bar{e}h + \frac{1}{2}\bar{\rho}\bar{u}^2 h + \bar{\rho}\left(\frac{h}{2}+z_{\mathrm{b}}\right)gh\cos\theta - \bar{\rho}xgh\sin\theta\right) \\ &\quad+\frac{\partial}{\partial x}\left(\bar{\rho}\bar{e}\bar{u}h + \frac{1}{2}\bar{\rho}\bar{u}^3 h + \bar{\rho}\left(\frac{h}{2}+z_{\mathrm{b}}\right)\bar{u}gh\cos\theta - \bar{\rho}\bar{u}xgh\sin\theta\right) \\ &\quad+\frac{\partial}{\partial x}(\bar{p}\bar{u}h) + \left(\bar{p}-\frac{1}{2}\bar{\rho}gh\cos\theta\right)\frac{\partial h}{\partial t} - \bar{\rho}gh\cos\theta\frac{\partial z_{\mathrm{b}}}{\partial t} \\ &\quad= \dot{M}_e + \dot{Q},\end{aligned} \tag{2.69}$$

where $\dot{M}_e$ is the rate of exchange of mechanical energy between the inside and outside of the system, and $\dot{Q}$ is the rate of exchange of heat between the inside and outside of the

system. Instead of solving Eq. (2.69), we also can solve the internal energy conservation equation:

$$\frac{\partial}{\partial t}\left(\bar{\rho}\bar{e}h\right)+\frac{\partial}{\partial x}\left(\bar{\rho}\bar{e}\bar{u}h\right)+\bar{p}\left(\frac{\partial h}{\partial t}+\frac{\partial}{\partial x}(\bar{u}h)\right) = \dot{Q}+\dot{M}_e-\left(\dot{M}_o\bar{u}-\dot{M}_a\frac{\bar{u}^2}{2}+\dot{M}_a g(\bar{z}\cos\theta-x\sin\theta)\right), \tag{2.70}$$

which is derived by substituting the mass and momentum conservation Eqs. (2.67) and (2.68) into the energy conservation Eq. (2.69); see Appendix B for the details of the algebra.

The thermal equation of state

From Eq. (2.6), the thermal equation of state is written as

$$\frac{1}{\bar{\rho}}=\frac{\bar{R}\bar{T}}{\bar{p}}, \tag{2.71}$$

where $\bar{R}$ is the gas constant, which may vary due to physical processes as entrainment of ambient fluid into the current.

The caloric equation of state

The caloric equation of state is written as

$$\frac{\partial\bar{T}}{\partial t}+\bar{u}\frac{\partial\bar{T}}{\partial x}=\frac{1}{\bar{C}_{\mathrm{v}}}\left(\frac{\partial\bar{e}}{\partial t}+\bar{u}\frac{\partial\bar{e}}{\partial x}\right) \tag{2.72}$$

from Eq. (2.7) or as

$$\frac{\partial\bar{T}}{\partial t}+\bar{u}\frac{\partial\bar{T}}{\partial x}=\frac{1}{\bar{C}_{\mathrm{p}}}\left(\frac{\partial}{\partial t}\left(\bar{e}+\frac{\bar{p}}{\bar{\rho}}\right)+\bar{u}\frac{\partial}{\partial x}\left(\bar{e}+\frac{\bar{p}}{\bar{\rho}}\right)\right) \tag{2.73}$$

from Eq. (2.8), where the heat capacity at constant volume $\bar{C}_{\mathrm{v}}$ and that at constant pressure $\bar{C}_{\mathrm{p}}$ may vary due to physical processes such as entrainment of ambient fluid into the

current.

The equation associated with the thermodynamic pressure $\bar{p}$

In the derivation processes of the momentum and energy conservation Eqs. (2.68) and (2.69), the thermodynamic pressure $\bar{p}$ is Eq. (2.51) with Eq. (2.53):

$$\begin{cases} \bar{p} = p_{\rm f} + \frac{1}{2}\bar{\rho} g h \cos\theta \\ p_{\rm f} = p_{\rm a0} + \rho_{\rm a} g x \sin\theta - \rho_{\rm a} g (h + z_{\rm b}) \cos\theta + \Delta p_{\rm f}, \end{cases} \tag{2.74}$$

where $p_{\rm a0}$ is a constant hydrostatic pressure of the ambient fluid at the reference point ($x = 0, z = 0$); see Figure 2.2. Instead of solving Eq. (2.74), we may be able to use the simplified version of Eq. (2.74):

$$\bar{p} = p_{\rm a0} \quad (= \text{const}). \tag{2.75}$$

Front condition

The front condition, which represents a quasi-steady balance between the buoyancy pressure driving the current front and the resistance pressure caused by the acceleration of the ambient fluid around the front, is written as Eq. (2.66):

$$\bar{u}_{\rm N} = Fr_{\rm N0} \sqrt{\frac{\bar{\rho}_{\rm N}}{\rho_{\rm a}}} \sqrt{\frac{\bar{\rho}_{\rm N} - \rho_{\rm a}}{\bar{\rho}_{\rm N}} g h_{\rm N} \cos\theta} \qquad \text{at} \quad x = x_{\rm N}(t), \tag{2.76}$$

where $Fr_{\rm N0}$, which is an imposed frontal Froude number in a Boussinesq system (i.e., $\bar{\rho}_{\rm N}/\rho_{\rm a} \approx 10^0$), is assumed to be a constant of order 10^0.

2.2 Two-layer model of pyroclastic density currents

We formulate a new unsteady two-layer PDC model, on the basis of the generalized unsteady one-layer shallow-water model derived in Section 2.1. Many PDCs spread ra-

dially from a volcanic vent, although some PDCs are confined within a canyon or valley. Thus, we formulate the dynamics of two-layer PDCs spreading both radially and restricted within one-dimensional channel. Since the one-layer model derived in Section 2.1 describes the behavior of one-dimensional channelized currents, we firstly formulate a one-dimensional channelized two-layer PDC model (Subsections 2.2.1–2.2.3), subsequently formulate a radially spreading two-layer PDC model (Subsection 2.2.4).

The two-layer model consists of a dilute layer and the underlying dense basal layer (Figure 2.3). The two layers evolve separately, but are coupled through physical processes as suspended volcanic ash particles in the dilute layer settle into the basal dense layer. Deposits are produced by the dilute and/or dense layers. The interface between the dilute layer and the surrounding ambient air ($z = z_{\mathrm{f}}(x,t)$) and the interface between the dilute and dense layers ($z = z_{\mathrm{m}}(x,t)$) are written as

$$z_{\mathrm{f}} = h + z_{\mathrm{m}} \tag{2.77}$$

$$z_{\mathrm{m}} = h_{\mathrm{H}} + z_{\mathrm{b}}, \tag{2.78}$$

using the local topography or the height of deposits formed by the current ($z_{\mathrm{b}}(x,t)$), the depth of the dilute layer ($h(x,t)$), and the depth of the dense layer ($h_{\mathrm{H}}(x,t)$), where the subscript H denotes the dense layer.

2.2.1 Dilute layer

We model the dilute current as a highly turbulent, well-mixed, particle-laden suspension flow. The dynamics of the dilute current is controlled by particle settling (e.g., Bonnecaze et al., 1993; Sparks et al., 1993), entrainment of ambient air (e.g., Bursik & Woods, 1996; Johnson & Hogg, 2013), basal drag (e.g., Hogg & Pritchard, 2004), and frontal resistance of ambient air (e.g., Ungarish, 2007; Shimizu et al., 2017). The entrainment of ambient air causes the thermal expansion of the dilute current (e.g., Bursik & Woods, 1996; Andrews & Manga, 2012). It is composed of the solid particles, volcanic gas, and the air entrained

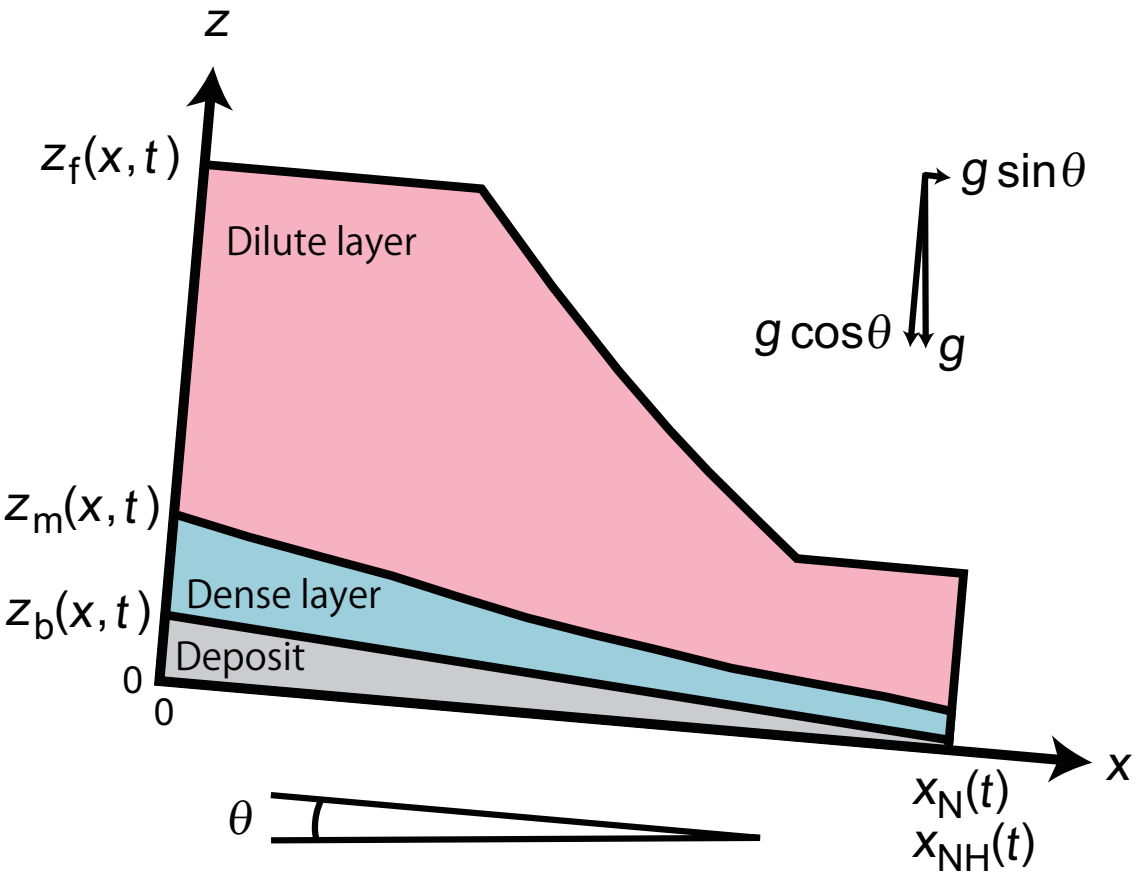

Figure 2.3: Schematic illustration of the two-layer PDC model, propagating along a slope inclined at θ to the horizontal, with x parallel to the slope and z perpendicular. There are three interfaces, between the top of the dilute layer and the surrounding ambient air ($z = z_{\rm f}(x,t)$), between the dilute and dense layers ($z = z_{\rm m}(x,t)$), and between the bottom of the current and the local topography imposed on the slope ($z = z_{\rm b}(x,t)$).

from ambient, so that the mass fractions ($\bar{n}$) obey

$$\bar{n}_{\rm s} + \bar{n}_{\rm a} + \bar{n}_{\rm g} = 1, \tag{2.79}$$

where the subscripts $\rm s$, $\rm g$, and $\rm a$ denote solid particles, volcanic gas, and air, respectively. There are seven main unknown variables (bulk density $\bar{\rho}$, depth h, velocity $\bar{u}$, internal energy $\bar{e}$, temperature $\bar{T}$, the mass fraction of the entrained air $\bar{n}_{\rm a}$, and the mass fraction of solid particles $\bar{n}_{\rm s}$) in the following seven equations (i.e., Eqs. (2.80), (2.81), (2.82), (2.85), (2.89), (2.90) and (2.91)). At the flow front of the dilute current, the front condition (2.93) is solved to describe realistic gravity current dynamics (e.g., Shimizu et al., 2017).

Mass conservation equations

On the basis of Eq. (2.67), the mass conservation equations for the entrained air, the particles in the current, and the bulk can be written as

$$\frac{\partial}{\partial t}(\bar{n}_{\rm a}\bar{\rho}h) + \frac{\partial}{\partial x}(\bar{n}_{\rm a}\bar{\rho}\bar{u}h) = \rho_{\rm a}E|\bar{u}|, \tag{2.80}$$

$$\frac{\partial}{\partial t}(\bar{n}_{\rm s}\bar{\rho}h) + \frac{\partial}{\partial x}(\bar{n}_{\rm s}\bar{\rho}\bar{u}h) = -\bar{n}_{\rm s}\bar{\rho}W_{\rm s}\cos\theta, \tag{2.81}$$

$$\frac{\partial}{\partial t}(\bar{\rho}h) + \frac{\partial}{\partial x}(\bar{\rho}\bar{u}h) = \rho_{\rm a}E|\bar{u}| - \frac{\bar{n}_{\rm s}}{n_{\rm sH}}\bar{\rho}W_{\rm s}\cos\theta, \tag{2.82}$$

respectively. Here, $\rho_{\rm a}$ is a constant density of ambient air, E is the entrainment coefficient, $W_{\rm s}$ is the settling velocity of the particles from the base of the dilute layer, and $n_{\rm sH}(=$ const) is the mass fraction of solid particles in the dense layer (see Subsection 2.2.2 for the details).

The entrainment of ambient air into the dilute layer is taken into account in the the right-hand side in Eq. (2.80) and the first term of the right-hand side in Eq. (2.82). Air entrainment is assumed to occur on the upper surface of the dilute layer (e.g., Bursik & Woods, 1996; Johnson & Hogg, 2013). In the same way as Bursik & Woods (1996), we

adopt the entrainment coefficient proposed by Parker et al. (1987):

$$E = \frac{0.075}{(1 + 718Ri^{2.4})^{0.5}}, \tag{2.83}$$

where the Richardson number: $Ri \equiv ((\bar{\rho} - \rho_{\rm a})gh\cos\theta)/(\bar{\rho}\bar{u}^2)$; see Figure 2.4.

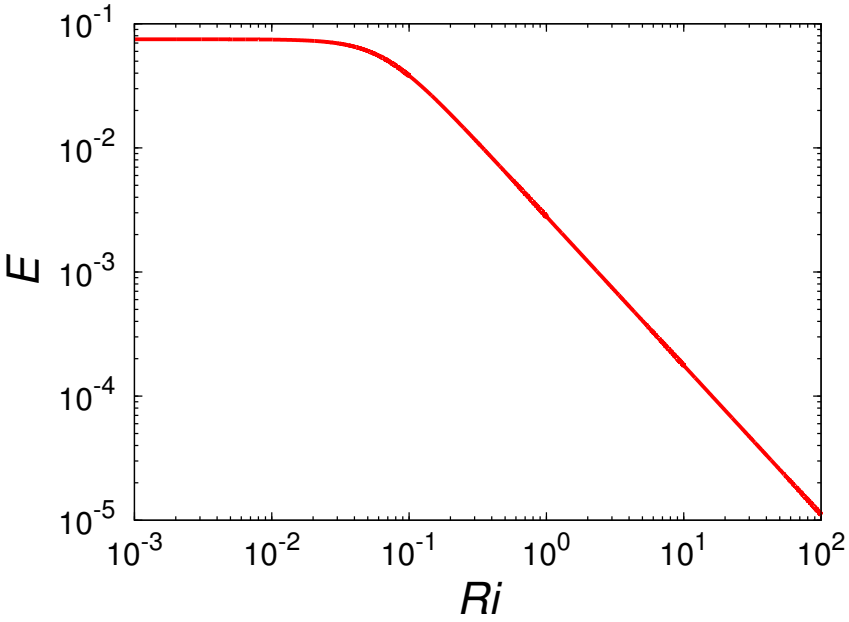

Figure 2.4: The entrainment coefficient E proposed by Parker et al. (1987) vs. the Richardson number Ri (Eq. (2.83)).

Particle settling from the dilute layer to the dense layer or the deposit is taken into account in the right-hand side in Eq. (2.81) and the second term of the right-hand side in Eq. (2.82). Note that, in the second term of the right-hand side in Eq. (2.82), the mass transfer of the particles and the volcanic gas is taken into account. $W_{\rm s}$ is given by (e.g., Sparks et al., 1997; Dellino et al., 2005):

$$W_{\rm s} = \sqrt{\frac{4(\rho_{\rm s} - \bar{\rho}_{\rm g\&a})gd}{3C_{\rm ds}\bar{\rho}_{\rm g\&a}}}, \tag{2.84}$$

where $\rho_{\rm s}$ is the density of particles, d is their diameter, $\bar{\rho}_{\rm g\&a}$ is the density of the gas phase composed of volcanic gas and entrained air, and a drag coefficient $C_{\rm ds}$ is herein set to 1

(cf. Woods & Bursik, 1991); see Figure 2.5.

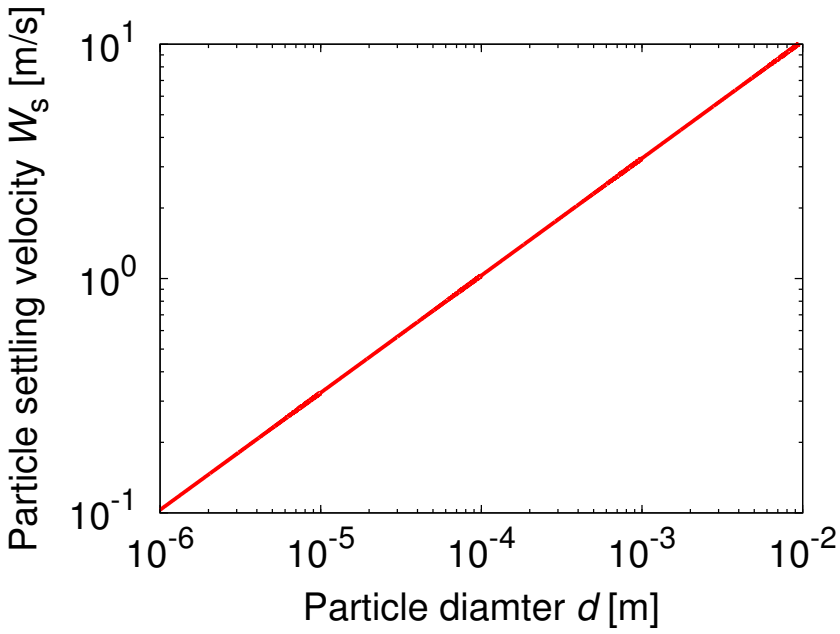

Figure 2.5: Particle settling velocity $W_{\rm s}$ vs. solid particle diameter d (Eq. (2.84)). Here, solid particle density $\rho_{\rm s}$ is assumed to be 1000 kg/m^3, and gas phase density $\bar{\rho}_{\rm g\&a}$ is assumed to ambient air density $\rho_{\rm a} (= 1.23$ kg/m$^3)$.

Momentum conservation equation

On the basis of Eq. (2.68), the momentum conservation equation can be written as

$$\frac{\partial}{\partial t}(\bar{\rho}\bar{u}h) + \frac{\partial}{\partial x}\left(\bar{\rho}\bar{u}^2 h + \frac{\bar{\rho}-\rho_{\rm a}}{2} g h^2 \cos\theta\right) = (\bar{\rho}-\rho_{\rm a}) g h \sin\theta - (\bar{\rho}-\rho_{\rm a}) g h \cos\theta \frac{\partial z_{\rm m}}{\partial x} - \frac{\bar{n}_{\rm s}}{n_{\rm sH}} \bar{\rho}\bar{u} W_{\rm s} \cos\theta - \tau_{\rm m}, \quad (2.85)$$

where $\tau_{\rm m}$ is the interfacial drag between the dilute layer and the dense layer or the deposit. Note that the friction on the side wall of the channel is neglected. The terms of the right-hand side of this momentum conservation equation represent the downslope and topographic acceleration, the momentum lost from the dilute current owing to the particle settling, and the interfacial drag. We model the interfacial drag as a Chézy-type drag (e.g.,

Doyle et al., 2008, 2010, 2011):

$$\tau_{\mathrm{m}} = C_{\mathrm{dm}}\bar{\rho}(\bar{u} - \bar{u}_{\mathrm{H}})|\bar{u} - \bar{u}_{\mathrm{H}}|, \tag{2.86}$$

where $\bar{u}_{\mathrm{H}}$ is the velocity of the dense layer, and C_{dm} is a Chézy drag coefficient. We estimate the drag coefficient C_{dm} using the empirical formula proposed by Hager (1988) and given by

$$C_{\mathrm{dm}} = 0.025 Re_0^{-0.2}, \tag{2.87}$$

where Re_0 is a characteristic Reynolds number of the dilute current (see Figure 2.6; cf. Hogg & Pritchard, 2004).

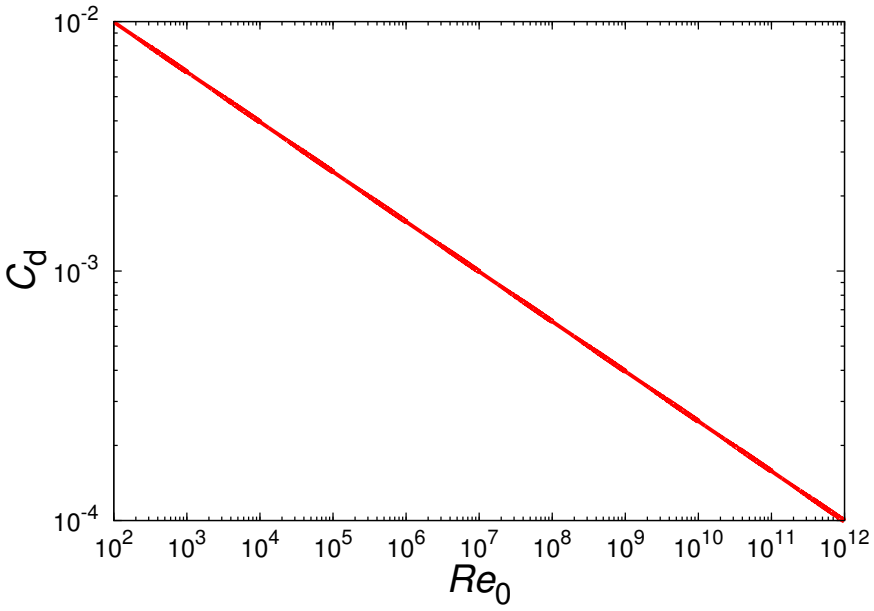

Figure 2.6: The drag coefficient C_{d} proposed by Hager (1988) vs. a characteristic Reynolds number Re_0 (Eq. (2.87)).

Energy conservation equation

On the basis of Eq. (2.69), the energy conservation equation can be written as

$$\begin{aligned}
&\frac{\partial}{\partial t}\left(\bar{\rho}\bar{e}h+\frac{1}{2}\bar{\rho}\bar{u}^2h+\bar{\rho}\left(\frac{h}{2}+z_{\mathrm{m}}\right)gh\cos\theta-\bar{\rho}xgh\sin\theta\right)\\
&\quad+\frac{\partial}{\partial x}\left(\bar{\rho}\bar{e}\bar{u}h+\frac{1}{2}\bar{\rho}\bar{u}^3h+\bar{\rho}\left(\frac{h}{2}+z_{\mathrm{m}}\right)\bar{u}gh\cos\theta-\bar{\rho}\bar{u}xgh\sin\theta+\bar{p}\bar{u}h\right)\\
&\quad+\left(\bar{p}-\frac{1}{2}\bar{\rho}gh\cos\theta\right)\frac{\partial h}{\partial t}-\bar{\rho}gh\cos\theta\frac{\partial z_{\mathrm{m}}}{\partial t}\\
&=\rho_{\mathrm{a}}E|\bar{u}|g\left((h+z_{\mathrm{m}})\cos\theta-x\sin\theta\right)-\frac{\bar{n}_{\mathrm{s}}}{n_{\mathrm{sH}}}\bar{\rho}W_{\mathrm{s}}\cos\theta\left(z_{\mathrm{m}}\cos\theta-x\sin\theta\right)\\
&\quad-\frac{1}{2}\frac{\bar{n}_{\mathrm{s}}}{n_{\mathrm{sH}}}\bar{\rho}\bar{u}^2W_{\mathrm{s}}\cos\theta-\tau_{\mathrm{m}}\bar{u}\\
&\quad+\rho_{\mathrm{a}}E|\bar{u}|C_{\mathrm{pa}}T_{\mathrm{a}}-\bar{n}_{\mathrm{s}}\bar{\rho}W_{\mathrm{s}}\cos\theta\;C_{\mathrm{s}}\bar{T}-\frac{1-n_{\mathrm{sH}}}{n_{\mathrm{sH}}}\bar{n}_{\mathrm{s}}\bar{\rho}W_{\mathrm{s}}\cos\theta\;C_{\mathrm{pg}}\bar{T},
\end{aligned}\tag{2.88}$$

where $\bar{p}$ is the thermodynamic pressure of the dilute current, C_{s} is the specific heat of the solid particles, C_{pg} is the specific heat of volcanic gas at constant pressure, C_{pa} is the specific heat of air at constant pressure, and T_{a} is a constant temperature of ambient air. The terms of the right-hand side of this total energy conservation equation represent the potential energy gained or lost from the dilute current owing to the entrainment of ambient air and the particle settling, the kinetic energy lost from the dilute current owing to the particle settling and the interfacial drag, and the thermal energy gained or lost from the dilute current owing to the entrainment of ambient air and the particle settling.

By using the mass and momentum conservation Eqs. (2.82) and (2.85), we can rewrite the total energy conservation Eq. (2.88) as

$$\begin{aligned}
&\frac{\partial}{\partial t}\left(\bar{\rho}\bar{e}h\right)+\frac{\partial}{\partial x}\left(\bar{\rho}\bar{e}\bar{u}h\right)+\bar{p}\left(\frac{\partial h}{\partial t}+\frac{\partial}{\partial x}\left(\bar{u}h\right)\right)\\
&\quad=\rho_{\mathrm{a}}E|\bar{u}|C_{\mathrm{pa}}T_{\mathrm{a}}-\bar{n}_{\mathrm{s}}\bar{\rho}W_{\mathrm{s}}\cos\theta\;C_{\mathrm{s}}\bar{T}-\frac{1-n_{\mathrm{sH}}}{n_{\mathrm{sH}}}\bar{n}_{\mathrm{s}}\bar{\rho}W_{\mathrm{s}}\cos\theta\;C_{\mathrm{pg}}\bar{T}\\
&\quad+\frac{\bar{u}^2}{2}\rho_{\mathrm{a}}E|\bar{u}|+\frac{gh\cos\theta}{2}\left(\rho_{\mathrm{a}}E|\bar{u}|+\frac{\bar{n}_{\mathrm{s}}}{n_{\mathrm{sH}}}\bar{\rho}W_{\mathrm{s}}\cos\theta\right);
\end{aligned}\tag{2.89}$$

see Eq. (2.70). The fourth term of the right-hand side of Eq. (2.89) represents the rate at

which kinetic energy is transferred to the entrained air. The fifth and sixth terms of the right-hand side of Eq. (2.89) represents the rate at which potential energy is converted to heat. Instead of Eq. (2.88), we use Eq. (2.89) with the constant thermodynamic pressure $\bar{p} = p_{\mathrm{a}0} (\equiv \rho_{\mathrm{a}} R_{\mathrm{a}} T_{\mathrm{a}} = \text{const})$, where R_{a} is the gas constant of air.

Thermal equation of state

On the basis of Eq. (2.71), the thermal equation of state can be written as

$$\frac{1}{\bar{\rho}} = \frac{\bar{n}_{\mathrm{s}}}{\rho_{\mathrm{s}}} + \frac{\bar{T}}{\bar{p}} (\bar{n}_{\mathrm{a}} R_{\mathrm{a}} + \bar{n}_{\mathrm{g}} R_{\mathrm{g}}). \tag{2.90}$$

Here, R_{g} is the gas constant of volcanic gas. In Eq. (2.90) as well as the energy conservation Eq. (2.89), the thermodynamic pressure is treated as a constant atmospheric pressure $\bar{p} = p_{\mathrm{a}0} (\equiv \rho_{\mathrm{a}} R_{\mathrm{a}} T_{\mathrm{a}} = \text{const})$.

Caloric equation of state

In the same way as Bursik & Woods (1996), we use the simplified version of the caloric equation of state (2.73):

$$\bar{e} + \frac{\bar{p}}{\bar{\rho}} = \bar{C}_{\mathrm{p}} \bar{T}. \tag{2.91}$$

Here, $\bar{C}_{\mathrm{p}}$ is the mass averaged specific heat at constant pressure of the current, given by

$$\bar{C}_{\mathrm{p}} = \bar{n}_{\mathrm{s}} C_{\mathrm{s}} + \bar{n}_{\mathrm{a}} C_{\mathrm{pa}} + \bar{n}_{\mathrm{g}} C_{\mathrm{pg}}. \tag{2.92}$$

In Eq. (2.91) as well as the energy conservation Eq. (2.89) and the thermal equation of state (2.90), the thermodynamic pressure is treated as a constant atmospheric pressure $\bar{p} = p_{\mathrm{a}0} (\equiv \rho_{\mathrm{a}} R_{\mathrm{a}} T_{\mathrm{a}} = \text{const})$.

Front condition

On the basis of Eq. (2.76), the front condition of the dilute current can be written as

$$\bar{u}_{\mathrm{N}} = Fr_{\mathrm{N0}}\sqrt{\frac{\bar{\rho}_{\mathrm{N}}}{\rho_{\mathrm{a}}}}\sqrt{\frac{\bar{\rho}_{\mathrm{N}}-\rho_{\mathrm{a}}}{\bar{\rho}_{\mathrm{N}}}gh_{\mathrm{N}}\cos\theta} \qquad \text{at} \quad x = x_{\mathrm{N}}(t), \tag{2.93}$$

where the subscript N denotes the front of the dilute current.

2.2.2 Dense layer

We model the dense current as a fluidized granular flow. The dynamics of the dense current is controlled by basal drag (e.g., Hogg & Pritchard, 2004; Roche et al., 2008; Gueugneau et al., 2017), progressive sedimentation (e.g., Doyle et al., 2007; Girolami et al., 2008, 2010; 2015; Doyle et al., 2010), and particle supplying from the overlying dilute current (e.g., Doyle et al., 2011; Breard et al., 2016; Kelfoun, 2017). The dense current, consisting of solid particles and volcanic gas, is assumed to have a constant bulk density

$$\rho_{\mathrm{H}} = \left(\frac{n_{\mathrm{sH}}}{\rho_{\mathrm{s}}} + \frac{1-n_{\mathrm{sH}}}{\rho_{\mathrm{gH}}}\right)^{-1} = \rho_{\mathrm{s}}\phi_{\mathrm{sH}} + \rho_{\mathrm{gH}}(1-\phi_{\mathrm{sH}}) = \text{const}, \tag{2.94}$$

where ρ_{gH} is a constant density of volcanic gas, and ϕ_{sH} is a constant volume fraction of solid particles in the dense layer. The constant mass fraction of solid particles in the dense layer is given by $n_{\mathrm{sH}} = \phi_{\mathrm{sH}}\rho_{\mathrm{s}}/\rho_{\mathrm{H}}$. There are two main unknown variables (depth h_{H} and velocity $\bar{u}_{\mathrm{H}}$) in the following two equations (i.e., Eqs. (2.95) and (2.97)).

Mass conservation equation

On the basis of Eq. (2.67), the mass conservation equation can be written as

$$\rho_{\mathrm{H}}\frac{\partial h_{\mathrm{H}}}{\partial t} + \rho_{\mathrm{H}}\frac{\partial}{\partial x}(\bar{u}_{\mathrm{H}}h_{\mathrm{H}}) = \frac{\bar{n}_{\mathrm{s}}}{n_{\mathrm{sH}}}\bar{\rho}W_{\mathrm{s}}\cos\theta - \rho_{\mathrm{H}}D, \tag{2.95}$$

where D is a deposition rate. The terms of the right-hand side of this mass conservation equation represent the particle supply from the dilute layer and the progressive sedimentation.

Although the deposition and erosion processes, determining the value of D, is not fully understood, the deposition rate D is assumed to be a hindered particle settling velocity in previous models of debris flows and fluvial flows (e.g., Cao, 2004; Li et al., 2017). We assume that the deposition rate D can be modeled as the hindered settling velocity to estimate the value of D using the empirical formula proposed by Richardson & Zaki (1954) and given by

$$D = (1 - \phi_{\mathrm{sH}})^m W_{\mathrm{sH}}, \tag{2.96}$$

where W_{sH} is the terminal velocity of a single particle at $\phi_{\mathrm{sH}} \approx 0$, and m is an empirical exponent that can vary from approximately 7 to 12 (see Figure 2.7; Druitt et al., 2007). W_{sH} is given by $\sqrt{4(\rho_{\mathrm{s}} - \rho_{\mathrm{gH}})gd/(3C_{\mathrm{ds}}\rho_{\mathrm{gH}})}$ in the same manner as W_{s} (Eq. (2.84)). Because typical range of particle volume fraction ϕ_{sH} is 0.4–0.5 (e.g., Breard et al., 2016), D/W_{sH} is the order of 10^{-3}–10^{-2} (Figure 2.7).

Momentum conservation equation

On the basis of Eq. (2.68), the momentum conservation equation can be written as

$$\begin{aligned}
&\rho_{\mathrm{H}} \frac{\partial}{\partial t}(\bar{u}_{\mathrm{H}} h_{\mathrm{H}}) + \rho_{\mathrm{H}} \frac{\partial}{\partial x}\left(\bar{u}_{\mathrm{H}}^2 h_{\mathrm{H}} + \frac{1}{2}\frac{\rho_{\mathrm{H}} - \rho_{\mathrm{a}}}{\rho_{\mathrm{H}}} g h_{\mathrm{H}}^2 \cos\theta \right) \\
&\quad = (\rho_{\mathrm{H}} - \rho_{\mathrm{a}}) g h_{\mathrm{H}} \sin\theta - (\rho_{\mathrm{H}} - \rho_{\mathrm{a}}) g h_{\mathrm{H}} \cos\theta \frac{\partial z_{\mathrm{b}}}{\partial x} - h_{\mathrm{H}} \frac{\partial}{\partial x}\left((\bar{\rho} - \rho_{\mathrm{a}}) g h \cos\theta \right) \\
&\qquad + \frac{\bar{n}_{\mathrm{s}}}{n_{\mathrm{sH}}} \bar{\rho} \bar{u} W_{\mathrm{s}} \cos\theta - \rho_{\mathrm{H}} \bar{u}_{\mathrm{H}} D + \tau_{\mathrm{m}} - \tau_{\mathrm{b}},
\end{aligned} \tag{2.97}$$

where τ_{b} is the basal drag. The terms of the right-hand side of this momentum conservation equation represent the downslope and topographic acceleration, the pressure gradient on the basal layer exerted by variations in the height of the overlying dilute layer, the

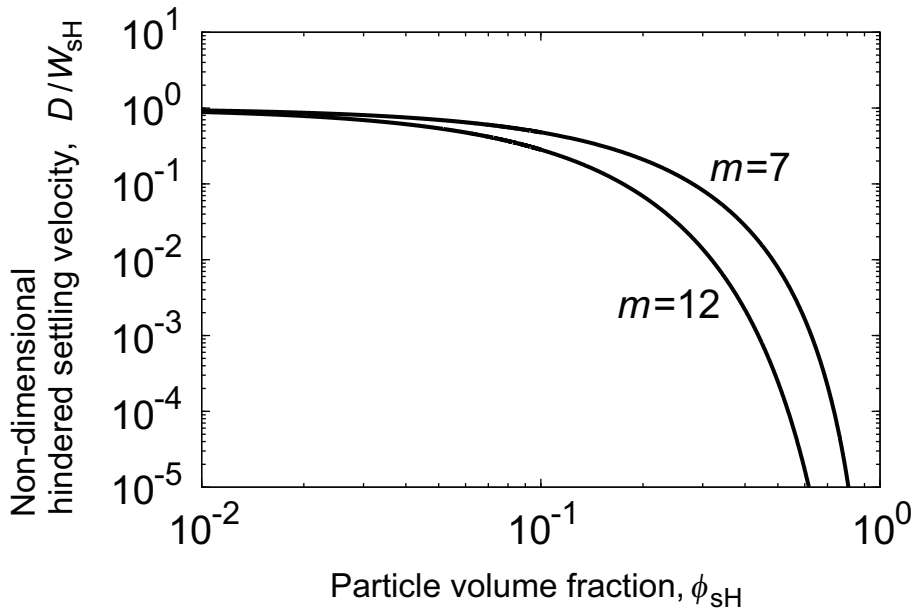

Figure 2.7: The non-dimensional deposition rate $D/W_{\rm sH}$ vs. volumetric fraction of solid particles $\phi_{\rm sH}$. The deposition rate D is estimated by the hindered particle settling velocity proposed by Richardson & Zaki (1954) (i.e., Eq. (2.96)).

momentum gained from the overlying dilute layer owing to the particle settling, the interfacial drag between the dense layer and the overlying dilute layer, and the basal drag.

The basal drag $\tau_{\rm b}$ is determined by the rheology of the dense current. According to experimental studies for an initially fluidized granular flow (e.g., Roche et al., 2008, 2010), the dense current initially has a fluid-inertial behavior (this stage is referred to as fluid-inertial regime; cf. Roche, 2012). This behavior is caused by the reduction of interparticle friction due to high internal gas pore pressure. Finally, the dense current decelerates and eventually stops because the pore pressure diffuses out and the interparticle friction increases (this stage is referred to as granular-frictional regime; cf. Roche, 2012). The basal drag of some dense PDC models is modeled as a Coulomb-type drag: $\tau_{\rm b} = \tan\delta(\rho_{\rm H} - \rho_{\rm a})gh_{\rm H}\cos\theta\bar{u}_{\rm H}/|\bar{u}_{\rm H}|$, where δ is a dynamic basal friction angle (e.g., Kelfoun & Druitt, 2005; Patra et al., 2005; Doyle et al., 2008, 2010, 2011; Kelfoun et al., 2009; Kelfoun, 2017). The Coulomb-type drag reproduces the granular-frictional behavior, but does not reproduce the fluid-inertial behavior (Roche et al., 2008; Shimizu et al.,

2017). On the other hand, a Chézy-type drag, which is often used to describe the basal drag of inviscid fluids (e.g., Hogg & Pritchard, 2004), reproduces the fluid-inertial behavior, but does not reproduce the granular-frictional behavior (Roche et al., 2008; Shimizu et al., 2017).

A significant part of the emplacement of the dense current is though to be the fluid-inertial regime. Thus, in order to reproduce the fluid-inertial behavior, we model the basal drag as a Chézy-type drag:

$$\tau_{\rm b} = C_{\rm db}\rho_{\rm H}\bar{u}_{\rm H}|\bar{u}_{\rm H}| \tag{2.98}$$

where $C_{\rm db}$ is a Chézy drag coefficient. We estimate the drag coefficient $C_{\rm db}$ using the empirical formula proposed by Hager (1988) and given by

$$C_{\rm db} = 0.025 Re_{\rm H0}^{-0.2} \tag{2.99}$$

where $Re_{\rm H0}$ is a characteristic Reynolds number of the dense current (see Figure 2.6; cf. Hogg & Pritchard, 2004).

Front condition

On the basis of Eq. (2.76), the front condition of the dense current can be written as

$$\bar{u}_{\rm NH} = Fr_{\rm N0}\sqrt{\frac{\rho_{\rm H}}{\rho_{\rm a}}}\sqrt{\frac{\rho_{\rm H}-\rho_{\rm a}}{\rho_{\rm H}}gh_{\rm NH}\cos\theta} \qquad \text{at} \quad x = x_{\rm NH}(t), \tag{2.100}$$

where the subscript $\rm NH$ denotes the front of the dense current.

2.2.3 Deposit

Assuming that the deposit is not erodible and has the same bulk density as the dense current, we may define the aggradation rate of material in the depositional system as

$$\frac{\partial z_{\mathrm{b}}}{\partial t} = \begin{cases} \dfrac{\bar{n}_{\mathrm{s}}}{n_{\mathrm{sH}}} \dfrac{\bar{\rho}}{\rho_{\mathrm{H}}} W_{\mathrm{s}} \cos\theta & \text{(Sedimentation from the dilute current)} \\ D & \text{(Sedimentation from the dense current)} \end{cases} \tag{2.101}$$

The mass conservation equation of the dense current (2.95) determines which of the two layers forms the deposit.

2.2.4 Radially spreading case

The dynamics of the radially spreading dilute and dense layers can be formulated, in the same way as the one-dimensional channelized case. The distance (i.e., radius) from the volcanic vent is represented by r. The conservation equations of the dilute layer can be

written as

Conservation of entrained air mass:

$$\frac{\partial}{\partial t}(\bar{n}_{\mathrm{a}}\bar{\rho}h)+\frac{1}{r}\frac{\partial}{\partial r}(\bar{n}_{\mathrm{a}}\bar{\rho}\bar{u}hr)=\rho_{\mathrm{a}}E|\bar{u}|, \tag{2.102}$$

Conservation of solid particle mass:

$$\frac{\partial}{\partial t}(\bar{n}_{\mathrm{s}}\bar{\rho}h)+\frac{1}{r}\frac{\partial}{\partial r}(\bar{n}_{\mathrm{s}}\bar{\rho}\bar{u}hr)=-\bar{n}_{\mathrm{s}}\bar{\rho}W_{\mathrm{s}}\cos\theta, \tag{2.103}$$

Conservation of bulk mass:

$$\frac{\partial}{\partial t}(\bar{\rho}h)+\frac{1}{r}\frac{\partial}{\partial r}(\bar{\rho}\bar{u}hr)=\rho_{\mathrm{a}}E|\bar{u}|-\frac{\bar{n}_{\mathrm{s}}}{n_{\mathrm{sH}}}\bar{\rho}W_{\mathrm{s}}\cos\theta, \tag{2.104}$$

Momentum conservation:

$$\begin{aligned}&\frac{\partial}{\partial t}(\bar{\rho}\bar{u}h)+\frac{1}{r}\frac{\partial}{\partial r}\left(\bar{\rho}\bar{u}^2hr\right)+\frac{\partial}{\partial r}\left(\frac{\bar{\rho}-\rho_{\mathrm{a}}}{2}gh^2\cos\theta\right)\\&\quad=(\bar{\rho}-\rho_{\mathrm{a}})gh\sin\theta-(\bar{\rho}-\rho_{\mathrm{a}})gh\cos\theta\frac{\partial z_{\mathrm{m}}}{\partial r}-\frac{\bar{n}_{\mathrm{s}}}{n_{\mathrm{sH}}}\bar{\rho}\bar{u}W_{\mathrm{s}}\cos\theta-\tau_{\mathrm{m}},\end{aligned} \tag{2.105}$$

Energy conservation:

$$\begin{aligned}&\frac{\partial}{\partial t}\left(\bar{\rho}\bar{e}h\right)+\frac{1}{r}\frac{\partial}{\partial r}\left(\bar{\rho}\bar{e}\bar{u}hr\right)+\bar{p}\left(\frac{\partial h}{\partial t}+\frac{1}{r}\frac{\partial}{\partial r}\left(\bar{u}hr\right)\right)\\&\quad=\rho_{\mathrm{a}}E|\bar{u}|C_{\mathrm{pa}}T_{\mathrm{a}}-\bar{n}_{\mathrm{s}}\bar{\rho}W_{\mathrm{s}}\cos\theta\,C_{\mathrm{s}}\bar{T}-\frac{1-n_{\mathrm{sH}}}{n_{\mathrm{sH}}}\bar{n}_{\mathrm{s}}\bar{\rho}W_{\mathrm{s}}\cos\theta\,C_{\mathrm{pg}}\bar{T}\\&\qquad+\frac{\bar{u}^2}{2}\rho_{\mathrm{a}}E|\bar{u}|+\frac{gh\cos\theta}{2}\left(\rho_{\mathrm{a}}E|\bar{u}|+\frac{\bar{n}_{\mathrm{s}}}{n_{\mathrm{sH}}}\bar{\rho}W_{\mathrm{s}}\cos\theta\right).\end{aligned} \tag{2.106}$$

The conservation equations of the dense layer can be written as

Mass conservation:

$$\rho_{\mathrm{H}}\frac{\partial h_{\mathrm{H}}}{\partial t}+\rho_{\mathrm{H}}\frac{1}{r}\frac{\partial}{\partial r}(\bar{u}_{\mathrm{H}}h_{\mathrm{H}}r)=\frac{\bar{n}_{\mathrm{s}}}{n_{\mathrm{sH}}}\bar{\rho}W_{\mathrm{s}}\cos\theta-\rho_{\mathrm{H}}D, \tag{2.107}$$

Momentum conservation:

$$\begin{aligned}&\rho_{\mathrm{H}}\frac{\partial}{\partial t}(\bar{u}_{\mathrm{H}}h_{\mathrm{H}})+\rho_{\mathrm{H}}\frac{1}{r}\frac{\partial}{\partial r}\left(\bar{u}_{\mathrm{H}}^2h_{\mathrm{H}}r\right)+\frac{\partial}{\partial r}\left(\frac{1}{2}\frac{\rho_{\mathrm{H}}-\rho_{\mathrm{a}}}{\rho_{\mathrm{H}}}gh_{\mathrm{H}}^2\cos\theta\right)\\&\quad=(\rho_{\mathrm{H}}-\rho_{\mathrm{a}})gh_{\mathrm{H}}\sin\theta-(\rho_{\mathrm{H}}-\rho_{\mathrm{a}})gh_{\mathrm{H}}\cos\theta\frac{\partial z_{\mathrm{b}}}{\partial r}-h_{\mathrm{H}}\frac{\partial}{\partial r}\left((\bar{\rho}-\rho_{\mathrm{a}})gh\cos\theta\right)\\&\qquad+\frac{\bar{n}_{\mathrm{s}}}{n_{\mathrm{sH}}}\bar{\rho}\bar{u}W_{\mathrm{s}}\cos\theta-\rho_{\mathrm{H}}\bar{u}_{\mathrm{H}}D+\tau_{\mathrm{m}}-\tau_{\mathrm{b}}.\end{aligned} \tag{2.108}$$

The other equations are the same as the one-dimensional channelized case.

Chapter 3

Numerical treatment

In Section 2.2, we have formulated a new unsteady two-layer PDC model. In this chapter, we describe numerical treatments of the model.

3.1 Finite volume method

As the system (2.77)–(2.101) are nonlinear and hyperbolic, shocks may develop in the currents. Consequently, we use a finite volume method with shock-capturing capability (e.g., LeVeque, 2002; Toro, 2001). Since the conservation equations in the system are not homogeneous equations (i.e., the terms of the right-hand sides of the conservation equations are non-zero), we use a fractional-step method (e.g., LeVeque, 2002) to solve the conservation equations with source terms (i.e., the terms of the right-hand sides of the equations) numerically, that is, the conservation equations with source terms:

$$\frac{\partial}{\partial t}\boldsymbol{q} + \frac{\partial}{\partial x}\boldsymbol{f}(\boldsymbol{q}) = \boldsymbol{s}(\boldsymbol{q}) \tag{3.1}$$

are split into two subproblems that can be solved independently:

$$\begin{cases} \frac{\partial}{\partial t}\boldsymbol{q} + \frac{\partial}{\partial x}\boldsymbol{f}(\boldsymbol{q}) = \boldsymbol{0} \\ \frac{\partial}{\partial t}\boldsymbol{q} = \boldsymbol{s}(\boldsymbol{q}), \end{cases} \tag{3.2}$$

where $\boldsymbol{q}$, $\boldsymbol{f}$ and $\boldsymbol{s}$ are the vectors of the conserved variables, fluxes and sources, respectively. Thus, we update a piecewise constant function $\boldsymbol{Q}_i^n$ that approximates the average value of the solution $\boldsymbol{q}$ in each grid cell i at time step n (i.e., $\boldsymbol{Q}_i^n \equiv \frac{1}{\Delta x}\int_{x_{i-1/2}}^{x_{i+1/2}} \boldsymbol{q}(x,t^n)\mathrm{d}x$), using the expression

$$\begin{cases} \text{1st step:} & \boldsymbol{Q}_i^* = \boldsymbol{Q}_i^n - \frac{\Delta t}{\Delta x}\left(\boldsymbol{F}_{i+1/2} - \boldsymbol{F}_{i-1/2}\right) \\ \text{2nd step:} & \boldsymbol{Q}_i^{n+1} = \boldsymbol{Q}_i^* + \Delta t\ \boldsymbol{S}(\boldsymbol{Q}_i^*), \end{cases} \tag{3.3}$$

where $\Delta x (= x_{i+1/2} - x_{i-1/2})$ is the constant cell length and $\Delta t (= t^{n+1} - t^n)$ is the time interval. The time interval Δt is limited by the Courant-Friedrichs-Lewy condition (e.g., LeVeque, 2002; Toro, 2001). The intercell flux between cells i and $i+1$, $\boldsymbol{F}_{i+1/2} (\equiv \frac{1}{\Delta t}\int_{t^n}^{t^{n+1}} \boldsymbol{f}(\boldsymbol{q}(x_{i+1/2},t))\mathrm{d}t)$, is obtained by using an approximate Riemann solver, such as the HLL scheme (e.g., Toro, 2001):

$$\boldsymbol{F}_{i+1/2} \approx \begin{cases} \boldsymbol{F}_i & \text{if} \quad S_i \geq 0, \\ \boldsymbol{F}^{\mathrm{hll}} \equiv \frac{S_{i+1}\boldsymbol{F}_i - S_i\boldsymbol{F}_{i+1} + S_{i+1}S_i(\boldsymbol{Q}_{i+1} - \boldsymbol{Q}_i)}{S_{i+1} - S_i} & \text{if} \quad S_i < 0 < S_{i+1}, \\ \boldsymbol{F}_{i+1} & \text{if} \quad S_{i+1} \leq 0. \end{cases} \tag{3.4}$$

For the case of the dilute current, the wave speed estimates S_i and S_{i+1} are given by

$$S_i = \bar{u}_i - a_i q_i, \qquad S_{i+1} = \bar{u}_{i+1} + a_{i+1} q_{i+1}, \tag{3.5}$$

where a_K ($K = i, i+1$) is given by

$$a_K = \sqrt{\frac{\bar{\rho}_K - \rho_{\mathrm{a}}}{\bar{\rho}_K} g h_K \cos\theta} \tag{3.6}$$

and q_K ($K = i, i+1$) is given by

$$q_K = \begin{cases} \sqrt{\frac{1}{2}\left[\frac{(h_* + h_K)h_*}{h_K^2}\right]} & \text{if} \quad h_* > h_K, \\ 1 & \text{if} \quad h_* \leq h_K. \end{cases} \tag{3.7}$$

Here, h_* is an estimate for the exact solution for h in "star region", given by

$$h_* = \frac{1}{2}(h_i + h_{i+1}) - \frac{1}{4}(\bar{u}_{i+1} - \bar{u}_i)(h_i + h_{i+1})/(a_i + a_{i+1}). \tag{3.8}$$

For the case of the dense current, the wave speed estimates S_i and S_{i+1} are given in the same way as the case of the dilute current.

3.2 Flow front

An mentioned above, PDCs are characterized by strong density stratification due to particle settling (e.g., Branney & Kokelaar, 2002), whereby a dilute current with $\bar{\rho}/\rho_{\rm a} = 10^0$–$10^1$ overrides the dense basal current with $\rho_{\rm H}/\rho_{\rm a} = 10^2$–$10^3$. if we are to capture the effects of the density ratio (i.e., $\bar{\rho}/\rho_{\rm a}$ and $\rho_{\rm H}/\rho_{\rm a}$), it is important to calculate the front condition (i.e., Eqs. (2.93) and (2.100)) correctly (Ungarish, 2007). Previously, two types of numerical models have been proposed to calculate the front condition. In one, the front condition is calculated as a boundary condition at each time step (e.g., Ungarish, 2009). We refer to this model as the Boundary Condition (BC) model (Figure 3.1a). In the other, the front condition is calculated by setting a thin artificial bed ahead of the front (e.g., Toro, 2001). We refer to this as the Artificial Bed (AB) model (Figure 3.1b). In the AB model, the resistance of the ambient fluid at the flow front is modeled by the reaction of the force pushing the artificial bed at the flow front. We assessed the BC and AB models by comparing their numerical results with the analytical results (see Appendix C for the details). The results from the BC model agree well with the analytical results when the density ratio $\lesssim 10^2$. In contrast, the AB model generates good approximations of

the analytical results for the density ratio $\gtrsim 10^2$. On the basis of these results, we use the BC model for the overlying dilute layer ($\bar{\rho}/\rho_{\rm a} = 10^0$–$10^1$) and the AB model for the underlying dense layer ($\rho_{\rm H}/\rho_{\rm a} = 10^2$–$10^3$).

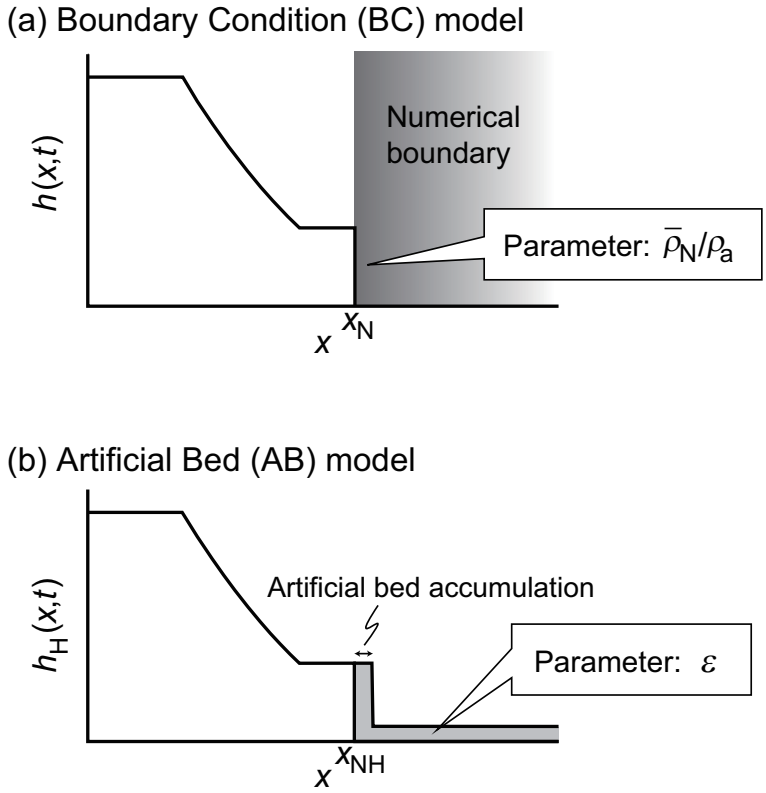

Figure 3.1: Schematic illustration of the numerical models used to calculate the front condition. (a) Boundary Condition (BC) model. (b) Artificial Bed (AB) model.

3.2.1 Boundary Condition (BC) model

In the BC model, the physical values at the flow front (the conserved variables and $x_{\rm N}$) are calculated as boundary conditions of the current from the front condition and the conservation equations at each time step. In the present numerical method, because we apply a fixed spatial coordinate with constant Δx, the front position $x = x_{\rm N}(t)$ generally does not coincide with the margins of the grid cells. We therefore define the cell that includes the front as the front cell ($i = FC(t)$, where $FC(t)$ is an integer), and the width of the region that the current occupies in the front cell as $\Delta x_{\rm FC}(t)$ ($0 \leq \Delta x_{\rm FC}(t) < \Delta x$;

see Figure 3.2). Using $FC(t)$ and $\Delta x_{\mathrm{FC}}(t)$, we can write the front position as

$$x_{\mathrm{N}}(t) = (FC(t) - 1)\Delta x + \Delta x_{\mathrm{FC}}(t). \tag{3.9}$$

Thus, in the conservation equations at the flow front, the kinematic condition ($\mathrm{d}x_{\mathrm{N}}/\mathrm{d}t = \bar{u}_{\mathrm{N}}$) should be taken into account.

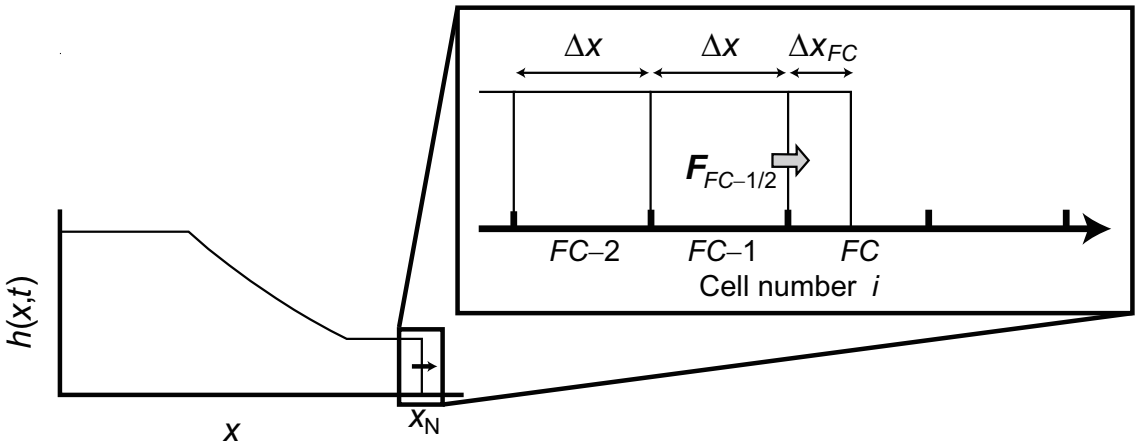

Figure 3.2: Schematic illustration of the computational domain of the Boundary Condition (BC) model.

3.2.2 Artificial Bed (AB) model

In the AB model, the conservation equations are numerically solved using a shock-capturing method for not only the interior, but also the outside of the current by *a priori* setting a thin artificial bed ahead of the front. Through this numerical procedure, the flow front is generated as the flow following a shock formed ahead of the front without any additional calculation. We give a sufficiently small value 10^{-10} to the non-dimensional thickness of the artificial bed, ε (Figure 3.1b; see Appendix C for the details).

3.3 Liftoff of dilute current

The dilute current is initially denser than ambient air. But, as it settles particles and thermally expands the entrained air, parts of it can become lighter than ambient air to reverse buoyancy. In natural pyroclastic density currents, this part can liftoff into air to produce a buoyant plume. In our numerical model, this part is not calculated after liftoff.

Chapter 4

Results

本章については、5 年以内に雑誌等で刊行予定のため、非公開。

Chapter 5

Discussion

本章については、5 年以内に雑誌等で刊行予定のため、非公開。

Chapter 6

Geological implication

本章については、5 年以内に雑誌等で刊行予定のため、非公開。

Chapter 7

Conclusion

In this thesis, a new two-layer model of pyroclastic density currents (PDCs) has been developed by using the unsteady shallow-water equations. The two-layer model, which is composed of a basal dense current and an overlying dilute current, captures the essential features of the dynamics of PDCs with strong vertical density stratification. The dynamics of the dilute current is controlled by frontal resistance of ambient air, air entrainment, thermal expansion of entrained air and particle settling. In the dense current, on the other hand, basal friction, progressive sedimentation and particle supply from the upper dilute current govern its dynamics. To understand the origin of diversity of PDC deposits, a series of numerical simulations of radially spreading or one-dimensional channelized PDCs were performed, involving a wide range of the mass eruption rates at source (i.e., the collapsing column edge) $\dot{M}_0$, the temperatures of erupted material $T_{\rm in}$, the particle settling velocities at the base of the dilute current $W_{\rm s}$, and the deposition rates at the base of the dense current D. We focused on time evolution of two-layer PDCs generated by initially dilute mixtures from collapsing eruption columns.

Numerical results show that a dilute PDC, generated from the collapsing column, produces a basal dense current (i.e., a two-layer PDC) as it flows, and a deposit aggrades upward from the base. When the frontal region of the dilute current becomes lighter than ambient air to reverse buoyancy and liftoff, the front of the dilute current does not

propagate further. When the mass flux of the dense current and the deposition rate at the base balance at the frontal region, the front of the dense current does not propagate further. Consequently, each layer converges to a steady state. These results provide a global view of the dyanamics and deposition of PDCs with strong density stratification. Since the dilute current is about 10^0 km thick, it may surmount topographic barriers to emplace its deposits on the topographic barriers. On the other hand, since the dense current is about 10^0 m thich, it may travel as valley-confined tongues being affected by local topography. The combination of the dilute and dense currents exhibits diverse features of dynamics depending on local topography, and hence, diverse features of deposits.

On the basis of the steady runout distances of the dilute and dense currents, the behaviors of the two-layer PDCs are classified into three regimes: Regime 1, Regime 2a, and Regime 2b (Chapter 4). In Regime 1, the dense current does not develop, and the dilute current directly forms its deposits. In Regime 2a, the dense current develops, but the steady runout distance of the dilute current is longer than that of the dense current. In Regime 2b, the dense current develops, and the steady runout distance of the dense current is longer than that of the dilute current (Figure **??**). We have systematically clarified the mechanisms which lead to the above classification of the flow regime through the following three steps.

First, we have identified governing dimensionless parameters: $W_{\rm s}/(\mathcal{U}a_0)$, $D/W_{\rm s}$, $E|\bar{u}|/W_{\rm s}$, and $(C_{\rm pa}T_{\rm a})/(C_{\rm p0}T_0)$ (Step 1; Section **??**). The parameter $W_{\rm s}/\mathcal{U}$ represents the ratio of the particle settling velocity at the base of the dilute current to the horizontal velocity scale of the two-layer PDC. The velocity scale $\mathcal{U}$ depends on the mass eruption rate at source $\dot{M}_0$ (i.e., $\mathcal{U} \propto \dot{M}_0^{1/5}$). The parameter a_0 is the aspect ratio of the height scale of the dilute current to the length (or radius) of the collapsing column, which is imposed on a boundary condition. The parameter $D/W_{\rm s}$ represents the relative magnitude of the effect of deposition from the base of the dense current to that of particle supply from the dilute current. The parameter $E|\bar{u}|/W_{\rm s}$ represents the relative magnitude of the effect of air entrainment to that of particle settling. Here, $E|\bar{u}|$ is the entrainment velocity,

where $\bar{u}$ is the local flow velocity and E is the entrainment coefficient. The parameter $(C_{\rm pa}T_{\rm a})/(C_{\rm p0}T_0)$, defined as the ratio of the enthalpy of the entrained air to that of the dilute current, represents the degree of thermal expansion of air entrained into the dilute current. Here, $C_{\rm pa}$ and $C_{\rm p0}$ are the heat capacities at constant pressure of air and the dilute current at the collapsing column edge, respectively, and $T_{\rm a}$ and T_0 is the temperatures of ambient air and the dilute current at the collapsing column edge, respectively.

Secondly, we have derived the analytical solution of the steady runout distances from the mass conservation equations of the two-layer PDCs for the case without air entrainment to understand the theoretical framework of the regime transition (Step 2; Section **??**). The analytical solution shows that the steady runout distances of the dilute and dense currents primarily depend on the parameter $W_{\rm s}/(\mathcal{U}a_0)$, which in turn depends on the mass eruption rate at source $\dot{M}_0$. The analytical solution also suggests that the boundaries of regimes (i.e., Regimes 1, 2a and 2b) are mainly determined by the parameter $D/W_{\rm s}$, which is independent of the mass eruption rate at source $\dot{M}_0$.

Finally, we have compared the analytical solution with numerical results of the two-layer model where the effects of air entrainment are taken into consideration (Step 3; Subsection **??**). The numerical results show that the runout distance of the two-layer PDCs is strongly affected by air entrainment in the case of small $W_{\rm s}/(\mathcal{U}a_0)$ (i.e., large $\dot{M}_0$), whereas the effect of air entrainment is limited in the case of large $W_{\rm s}/(\mathcal{U}a_0)$ (i.e., small $\dot{M}_0$).

The numerical results also show that the effects of thermal expansion of entrained air on the steady runout distances strongly depend on the temperature of erupted material (i.e., the parameter $(C_{\rm pa}T_{\rm a})/(C_{\rm p0}T_0)$) (Subsection **??**). When the temperature of erupted material is high (i.e., small $(C_{\rm pa}T_{\rm a})/(C_{\rm p0}T_0)$), a large degree of thermal expansion of entrained air significantly enhances the liftoff; as a result, the steady runout distance of the dilute current decreases as the degree of air entrainment increases. In this case, the steady runout distance of the dense current also decreases because thermal expansion of entrained air in the overlying dilute current leads to decreasing of the particle supply

from the dilute current to the dense current. When the temperature of erupted material is low (i.e., large $(C_{\mathrm{pa}}T_{\mathrm{a}})/(C_{\mathrm{p0}}T_0)$), on the other hand, the entrainment of air results in thickening of the dilute current without enhancing liftoff; as a result, the steady runout distance does not decrease or can even increase as the degree of entrainment increases. Because thickening of the dilute current also leads to decreasing the particle settling from the dilute current to the dense current, the steady runout distance of the dense current decreases as the degree of entrainment increases for the large $(C_{\mathrm{pa}}T_{\mathrm{a}})/(C_{\mathrm{p0}}T_0)$ case, too.

Through the above discussions, we have established a diagram showing the transitions of the flow regimes (i.e., Regimes 1, 2a and 2b) in the parameter space of D/W_{s} vs. $W_{\mathrm{s}}/(\mathcal{U}a_0)$ (Section **??**). The analytical solution shows that the transition condition between Regimes 1 and 2a is dependent on the parameter D/W_{s} but is independent of the other parameters. The analytical solution indicates that the transition between Regimes 2a and 2b is also dependent on the parameter D/W_{s} alone under the condition without air entrainment. However, when the effect of air entrainment is considered, the transition between Regimes 2a and 2b depends on the temperature of erupted material; the region of Regime 2a expands in the regime diagram as $W_{\mathrm{s}}/(\mathcal{U}a_0)$ decreases, in the case of low temperature.

In the numerical results of our unsteady model using the shallow-water equations, we commonly observe "overshoot": namely, the maximum runout distance of the transitional state exceeds the steady runout distance (Section **??**). The overshoot of the dilute current results from the formation of head, which in turn is caused by the frontal resistance of ambient air. Because the head is thicker than the body, the particle settling rate in the head is lower than that in the body, so that the head can flow further than the body, the rear of which roughly corresponds to the steady runout distance. The overshoot of the dense current, on the other hand, results from two types of mechanisms. One is that the overshoot of the dense current results from formation of the dense current head (Figure **??**a). Because the head of the dense current is thicker than the body of the dense current, the head can flow further than the body, the rear of which roughly corresponds to the

steady runout distance of the dense current. The other mechanism is that the overshoot of the dense current is directly formed by the dilute current flowing further than the steady runout distance of the dense current (Figure **??**b).

In this study, we have discussed not only radially spreading (axisymmetric) PDCs, but also one-dimensional (1D) channelized currents (Section **??**). Although the results of 1D channelized currents show basically similar tendencies to those of the radially spreading case, there are some different features between two cases as follows; (1) the runout distance of the 1D channelized currents is much longer than that of the radially spreading currents, (2) the effect of air entrainment to that of particle settling is less remarkable in the 1D channelized currents than that of the radially spreading currents. These features are explained by the fact that the 1D channelized currents are thicker than the radially spreading currents (Figure **??**).

We consider that the present model has improved the results of existing models of PDCs in several aspects (Section **??**). In the one-layer dilute PDC models of Bursik & Woods (1996), Dade & Huppert (1996) and Dade (2003), the strong vertical density stratification is not taken into account. Although the runout distances predicted by these models are qualitatively consistent with that of the present model for Regimes 1 and 2a, they substantially underestimate the runout distance of PDCs for Regime 2b. In the models of Dade & Huppert (1996) and Dade (2003) and the unsteady two-layer PDC models of Doyle et al. (2008, 2010, 2011) and Kelfoun (2017), air entrainment is not taken into account. As a result, these previous models significantly overestimate the runout distances of the dilute current with high temperature and the dense current, and underestimate the runout distances of the dilute current with low temperature, particularly when the relative magnitude of the effect of air entrainment to that of particle settling is large (i.e., small $W_{\mathrm{s}}/(\mathcal{U}a_0)$).

The present results account for diverse features of PDC deposits (e.g., distributions and sedimentary structures) (Chapter 6). A wide range of distributions of PDC deposits can be accounted for by variable runout distances of PDCs, depending on the mass erup-

tion rate at source, $\dot{M}_0$. Generally, a wide variety of sedimentary structures of PDC deposits (e.g., massive and/or stratified lithofacies) result from the flow-particle interaction inside the boundary layer at the bottom of PDCs (Branney & Kokelaar, 2002). Because the flow-particle interaction in the bottom boundary layer is significantly different between the dilute and dense currents, it is considered that some of the diversities of PDC deposits are explained by the difference in the flow-particle interaction in the bottom boundary layer between the dilute and dense currents. When stratified lithofacies are predominantly observed from proximal to distal areas, the PDC deposits are interpreted to be emplaced by PDCs of Regime 1. When massive lithofacies are predominantly observed from proximal to distal areas, the PDC deposits are interpreted to be emplaced by PDCs of Regime 2b. When distal lithofacies change from massive to stratified, the PDC deposits are interpreted to be emplaced by PDCs of Regime 2a. Our results that the region of Regime 2a expands as the temperature of erupted material decreases in the regime diagram are consistent with the observation that stratified surge deposits are commonly observed in the deposits of phreatomagmatic eruptions (e.g., base surge deposits; see Cas & Wright, 1987).

Although we believe that the conclusions derived in this thesis are robust and provide new insights into the dynamics of PDCs and the diversity of PDC deposits, we should bear in mind the limitations of the present model. We suggest some future works as follows.

- The deposition rate at the base of the dense current, D, must be accurately modeled, because D critically affects the transitions of the above regimes. In the present study, we tentatively modeled the value of D on the basis of the hindered settling velocity; however, the values of D is considered to be determined by combinations of the deposition and erosion processes in the dense currents. Some experimental studies of an initially fluidized granular flows are in progress (e.g., Roche et al., 2010; Girolami et al., 2010, 2015; Roche, 2012), but the deposition and erosion processes are not yet fully understood.

- The elutriation process from the dense current may play an important role in PDC dynamics and PDC deposits. In the present model, we assumed that the upper dilute current is formed by the collapsing eruption column edge; however, field observations of natural PDCs indicate that dilute ash clouds are also formed by elutriation from the dense current (Branney & Kokelaar, 2002). It is also suggested that the dilute current derived by the elutriation may proceed the parent dense current (e.g., Kelfoun, 2017; Kelfoun et al., 2017).

- A gradual density stratification develops in the upper dilute part of natural PDCs (e.g., Dufek, 2016; Breard et al., 2016), whereas the present two-layer PDC model is depth-averaged within each layer. To quantitatively reproduce PDC dynamics and PDC deposits, the vertical profiles of the density stratification within the dilute current should be taken into consideration.

- The pore-pressure diffusion in the dense current causes an increase of friction (e.g., Gueugneau et al., 2017). In the present model, although this effect is not directly considered, the effects of stopping of the dense current due to the the friction are indirectly taken into account in the deposition process with the (effective) deposition speed D. To quantitatively reproduce PDC dynamics and PDC deposits, the effects of the pore-pressure diffusion in the dense current should be fully taken into account.

A more sophisticated model that takes the above effects into account needs to be developed to reproduce quantitative features of field observations.

Appendix A

Summary of notations

a_0	Aspect ratio of $\mathcal{H}$ to r_0 (or x_0)
b_0	Aspect ratio of y_0 to r_0 (or x_0)
C_d	Drag coefficient
C_p	Heat capacity at constant pressure
C_s	Heat capacity of solid particle
C_v	Heat capacity at constant volume
D	Deposition rate at the base of dense current [m/s]
d	Diameter of solid particle [m]
E	Entrainment coefficient
e	Internal energy per unit mass [m^2/s^2]
e_tot	Total energy per unit mass [m^2/s^2]
Fr	Froude number of current
Fr_N0	Imposed frontal Froude number
g	Gravitational body force [m/s^2]
h	Thickness of current [m]
$\mathcal{H}$	Characteristic height scale of current [m]
$\dot{M}_0$	Mass eruption rate at the collapsing eruption column edge [kg/s]
n	Mass fraction (or time step)

p	Pressure [Pa]
R	Gas constant [J/(kg·K)]
r	Radius (distance) from volcanic vent (in radially spreading cases) [m]
Re	Reynolds number of current
Ri	Richardson number of current
T	Temperature [K]
t	Time [s]
$\mathcal{T}$	Characteristic time scale [s]
u	Velocity component in x (or r) direction [m/s]
$\mathcal{U}$	Characteristic velocity scale [m/s]
w	Velocity component in z direction [m/s]
W_{s}	Particle settling velocity at the base of (dilute) current [m/s]
x	Distance from volcanic vent (in one-dimensional channelized cases) [m]
y_0	Width of the one-dimensional channel [m]
z	Coordinate in the direction perpendicular to ground surface [m]

Subscript

a	Air
ave	Used to emphasize a horizontally averaged variable
b	Upper surface of ground or deposit (i.e., base of (dense) current)
base	Base of current
c	Current
f	Upper surface of dilute current
FC	Front cell of Boundary Condition model
g	Volcanic gas
g&a	Gas phase (i.e., volcanic gas and air)
H	Dense (i.e., high particle concentration) current

in Volcanic vent

m Upper surface of dense current

N Nose (i.e., front) of current

s Solid particle

0 Collapsing eruption column edge or other reference point

∞ Steady runout distance of current

Upper- and over-script

* Used to emphasize a non-dimensional variable
(a dimensional variable only in Appendix C.4)

– Used to emphasize a depth-averaged (i.e., z-averaged) variable

Greek

γ Ratio of specific heats $C_{\mathrm{p}}/C_{\mathrm{v}}$

Γ Riemann Invariants

Δp Pressure difference $p - p_{\mathrm{a}}$ [Pa]

δ Dynamic basal friction angle [°]

ε Non-dimensional thickness of artificial bed in Artificial Bed model

η Viscosity [Pa·s]

τ Drag at the base of current [kg/(m·s^2)]

θ Angle between the x (or r) axis and the horizontal axis [°]

ρ Mass density [kg/m^3]

ϕ Volume fraction

Appendix B

Derivation of the internal energy conservation Eq. (2.70)

The energy conservation Eq. (2.69) can be rewritten as

$$\begin{aligned}
&\frac{\partial}{\partial t}(\bar{\rho}\bar{e}h) + \frac{\partial}{\partial x}(\bar{\rho}\bar{e}\bar{u}h) \\
&\quad = -\frac{\partial}{\partial t}\left(\frac{1}{2}\bar{\rho}\bar{u}^2 h\right) - \frac{\partial}{\partial x}\left(\frac{1}{2}\bar{\rho}\bar{u}^3 h\right) \\
&\qquad -\frac{\partial}{\partial t}\left(\bar{\rho}gh\left(\bar{z}\cos\theta - x\sin\theta\right)\right) - \frac{\partial}{\partial x}\left(\bar{\rho}\bar{u}gh\left(\bar{z}\cos\theta - x\sin\theta\right)\right) \\
&\qquad -\frac{\partial}{\partial x}\left(\bar{p}\bar{u}h\right) - \left(\bar{p} - \frac{1}{2}\bar{\rho}gh\cos\theta\right)\frac{\partial h}{\partial t} + \bar{\rho}gh\cos\theta\frac{\partial z_{\mathrm{b}}}{\partial t} \\
&\qquad +\dot{Q} + \dot{M}_e. \qquad \text{(B.1)}
\end{aligned}$$

In this chapter, by using the mass and momentum conservation Eqs. (2.67) and (2.68), we transform the right-hand side of Eq. (B.1) to derive the internal energy conservation Eq. (2.70).

Using the mass conservation Eq. (2.67), we can obtain

$$\begin{aligned}
&\frac{\partial}{\partial t}\left(\bar{\rho}gh(\bar{z}\cos\theta - x\sin\theta)\right) + \frac{\partial}{\partial x}\left(\bar{\rho}g\bar{u}h(\bar{z}\cos\theta - x\sin\theta)\right) \\
&\quad = \bar{\rho}gh\cos\theta\left(\frac{\partial\bar{z}}{\partial t} + \bar{u}\frac{\partial\bar{z}}{\partial x}\right) - \bar{\rho}g\bar{u}h\sin\theta \\
&\qquad + g(\bar{z}\cos\theta - x\sin\theta)\dot{M}_a. \qquad \text{(B.2)}
\end{aligned}$$

We substitute Eq. (B.2) into Eq. (B.1) to obtain

$$\begin{aligned}
&\frac{\partial}{\partial t}(\bar{\rho}\bar{e}h) + \frac{\partial}{\partial x}(\bar{\rho}\bar{e}\bar{u}h) \\
&\quad = -\frac{\partial}{\partial t}\left(\frac{1}{2}\bar{\rho}\bar{u}^2h\right) - \frac{\partial}{\partial x}\left(\frac{1}{2}\bar{\rho}\bar{u}^3h\right) \\
&\qquad -\bar{\rho}gh\cos\theta\left(\frac{\partial\bar{z}}{\partial t} + \bar{u}\frac{\partial\bar{z}}{\partial x}\right) + \bar{\rho}g\bar{u}h\sin\theta \\
&\qquad -\frac{\partial}{\partial x}\left(\bar{p}\bar{u}h\right) - \left(\bar{p} - \frac{1}{2}\bar{\rho}gh\cos\theta\right)\frac{\partial h}{\partial t} + \bar{\rho}gh\cos\theta\frac{\partial z_{\mathrm{b}}}{\partial t} \\
&\qquad +\dot{Q} + \dot{M}_e - g(\bar{z}\cos\theta - x\sin\theta)\dot{M}_a \\
&\quad = -\frac{\partial}{\partial t}\left(\frac{1}{2}\bar{\rho}\bar{u}^2h\right) - \frac{\partial}{\partial x}\left(\frac{1}{2}\bar{\rho}\bar{u}^3h\right) \\
&\qquad -\bar{\rho}g\bar{u}h\cos\theta\frac{\partial\bar{z}}{\partial x} + \bar{\rho}g\bar{u}h\sin\theta \\
&\qquad -\frac{\partial}{\partial x}\left(\bar{p}\bar{u}h\right) - \bar{p}\frac{\partial h}{\partial t} \\
&\qquad +\dot{Q} + \dot{M}_e - g(\bar{z}\cos\theta - x\sin\theta)\dot{M}_a \qquad (\because \text{ Eq. (2.50)}). \qquad \text{(B.3)}
\end{aligned}$$

We can rewrite the momentum conservation Eq. (2.68) as

$$
\begin{aligned}
&\frac{\partial}{\partial t}(\bar{\rho}\bar{u}h) + \frac{\partial}{\partial x}\left(\bar{\rho}\bar{u}^2 h\right) + \frac{\partial}{\partial x}\left(\frac{1}{2}\bar{\rho}gh^2\cos\theta\right) \\
&\qquad + h\frac{\partial p_{\mathrm{f}}}{\partial x} - \bar{\rho}gh\sin\theta + \bar{\rho}gh\cos\theta\frac{\partial z_{\mathrm{b}}}{\partial x} = \dot{M}_o \qquad (\because \text{ Eq. (2.74)}) \\
\therefore \quad &\frac{\partial}{\partial t}(\bar{\rho}\bar{u}h) + \frac{\partial}{\partial x}\left(\bar{\rho}\bar{u}^2 h\right) + \frac{\partial}{\partial x}\left(\left(p_{\mathrm{f}} + \frac{1}{2}\bar{\rho}gh\cos\theta\right)h\right) \\
&\qquad - p_{\mathrm{f}}\frac{\partial h}{\partial x} - \bar{\rho}gh\sin\theta + \bar{\rho}gh\cos\theta\frac{\partial z_{\mathrm{b}}}{\partial x} = \dot{M}_o \\
\therefore \quad &\frac{\partial}{\partial t}(\bar{\rho}\bar{u}h) + \frac{\partial}{\partial x}\left(\bar{\rho}\bar{u}^2 h\right) + \frac{\partial}{\partial x}\left(\bar{p}h\right) \\
&\qquad - p_{\mathrm{f}}\frac{\partial h}{\partial x} + \bar{\rho}gh\cos\theta\frac{\partial z_{\mathrm{b}}}{\partial x} - \bar{\rho}gh\sin\theta = \dot{M}_o \qquad (\because \text{ Eq. (2.74)}).
\end{aligned} \tag{B.4}
$$

Using the expressions

$$
\begin{aligned}
\bar{u}\frac{\partial}{\partial t}(\bar{\rho}\bar{u}h) &= \frac{\partial}{\partial t}(\bar{\rho}\bar{u}^2 h) - \bar{\rho}\bar{u}h\frac{\partial \bar{u}}{\partial t} \\
&= \frac{1}{2}\frac{\partial}{\partial t}(\bar{\rho}\bar{u}^2 h) + \frac{1}{2}\frac{\partial}{\partial t}(\bar{\rho}\bar{u}^2 h) - \bar{\rho}\bar{u}h\frac{\partial \bar{u}}{\partial t} \\
&= \frac{1}{2}\frac{\partial}{\partial t}(\bar{\rho}\bar{u}^2 h) + \frac{\bar{u}^2}{2}\frac{\partial}{\partial t}(\bar{\rho}h) + \bar{\rho}h\frac{\partial}{\partial t}\left(\frac{\bar{u}^2}{2}\right) - \bar{\rho}\bar{u}h\frac{\partial \bar{u}}{\partial t} \\
&= \frac{1}{2}\frac{\partial}{\partial t}(\bar{\rho}\bar{u}^2 h) + \frac{\bar{u}^2}{2}\frac{\partial}{\partial t}(\bar{\rho}h)
\end{aligned} \tag{B.5}
$$

and

$$
\begin{aligned}
\bar{u}\frac{\partial}{\partial x}(\bar{\rho}\bar{u}^2 h) &= \frac{\partial}{\partial x}(\bar{\rho}\bar{u}^3 h) - \bar{\rho}\bar{u}^2 h\frac{\partial \bar{u}}{\partial x} \\
&= \frac{1}{2}\frac{\partial}{\partial x}(\bar{\rho}\bar{u}^3 h) + \frac{1}{2}\frac{\partial}{\partial x}(\bar{\rho}\bar{u}^3 h) - \bar{\rho}\bar{u}^2 h\frac{\partial \bar{u}}{\partial x} \\
&= \frac{1}{2}\frac{\partial}{\partial x}(\bar{\rho}\bar{u}^3 h) + \frac{\bar{u}^2}{2}\frac{\partial}{\partial x}(\bar{\rho}\bar{u}h) + \bar{\rho}\bar{u}h\frac{\partial}{\partial x}\left(\frac{\bar{u}^2}{2}\right) - \bar{\rho}\bar{u}^2 h\frac{\partial \bar{u}}{\partial x} \\
&= \frac{1}{2}\frac{\partial}{\partial x}(\bar{\rho}\bar{u}^3 h) + \frac{\bar{u}^2}{2}\frac{\partial}{\partial x}(\bar{\rho}\bar{u}h),
\end{aligned} \tag{B.6}
$$

we can rewrite Eq. (B.4) as

$$\begin{aligned}
&\frac{\partial}{\partial t}\left(\frac{1}{2}\bar{\rho}\bar{u}^2 h\right) + \frac{\partial}{\partial x}\left(\frac{1}{2}\bar{\rho}\bar{u}^3 h\right) \\
&\quad = -\bar{u}\frac{\partial}{\partial x}(\bar{p}h) + p_{\mathrm{f}}\bar{u}\frac{\partial h}{\partial x} - \bar{\rho}gh\bar{u}\cos\theta\frac{\partial z_{\mathrm{b}}}{\partial x} + \bar{\rho}gh\bar{u}\sin\theta \\
&\qquad +\bar{u}\dot{M}_o - \frac{\bar{u}^2}{2}\left(\frac{\partial}{\partial t}(\bar{\rho}h) + \frac{\partial}{\partial x}(\bar{\rho}\bar{u}h)\right) \\
&\quad = -\bar{u}\frac{\partial}{\partial x}(\bar{p}h) + p_{\mathrm{f}}\bar{u}\frac{\partial h}{\partial x} - \bar{\rho}gh\bar{u}\cos\theta\frac{\partial z_{\mathrm{b}}}{\partial x} + \bar{\rho}gh\bar{u}\sin\theta \\
&\qquad +\bar{u}\dot{M}_o - \frac{\bar{u}^2}{2}\dot{M}_a \qquad (\because \text{ Eq. (2.67)}).
\end{aligned} \tag{B.7}$$

We substitute Eq. (B.7) into Eq. (B.3) to obtain

$$\begin{aligned}
&\frac{\partial}{\partial t}(\bar{\rho}\bar{e}h) + \frac{\partial}{\partial x}(\bar{\rho}\bar{e}\bar{u}h) \\
&\quad = \bar{u}\frac{\partial}{\partial x}(\bar{p}h) - p_{\mathrm{f}}\bar{u}\frac{\partial h}{\partial x} + \bar{\rho}gh\bar{u}\cos\theta\frac{\partial z_{\mathrm{b}}}{\partial x} - \bar{\rho}g\bar{u}h\cos\theta\frac{\partial \bar{z}}{\partial x} \\
&\qquad -\frac{\partial}{\partial x}(\bar{p}\bar{u}h) - \bar{p}\frac{\partial h}{\partial t} \\
&\qquad +\dot{Q} + \dot{M}_e - \bar{u}\dot{M}_o + \frac{\bar{u}^2}{2}\dot{M}_a - g(\bar{z}\cos\theta - x\sin\theta)\dot{M}_a \\
&\quad = \bar{u}\frac{\partial}{\partial x}(\bar{p}h) - p_{\mathrm{f}}\bar{u}\frac{\partial h}{\partial x} - \frac{1}{2}\bar{\rho}gh\bar{u}\cos\theta\frac{\partial h}{\partial x} \\
&\qquad -\frac{\partial}{\partial x}(\bar{p}\bar{u}h) - \bar{p}\frac{\partial h}{\partial t} \\
&\qquad +\dot{Q} + \dot{M}_e - \bar{u}\dot{M}_o + \frac{\bar{u}^2}{2}\dot{M}_a - g(\bar{z}\cos\theta - x\sin\theta)\dot{M}_a \qquad (\because \text{ Eq. (2.50)}) \\
&\quad = \bar{u}\frac{\partial}{\partial x}(\bar{p}h) - \bar{p}\bar{u}\frac{\partial h}{\partial x} \\
&\qquad -\frac{\partial}{\partial x}(\bar{p}\bar{u}h) - \bar{p}\frac{\partial h}{\partial t} \\
&\qquad +\dot{Q} + \dot{M}_e - \bar{u}\dot{M}_o + \frac{\bar{u}^2}{2}\dot{M}_a - g(\bar{z}\cos\theta - x\sin\theta)\dot{M}_a \qquad (\because \text{ Eq. (2.74)}) \\
\therefore \quad &\frac{\partial}{\partial t}(\bar{\rho}\bar{e}h) + \frac{\partial}{\partial x}(\bar{\rho}\bar{e}\bar{u}h) + \bar{p}\left(\frac{\partial h}{\partial t} + \frac{\partial}{\partial x}(\bar{u}h)\right) \\
&\quad = \dot{Q} + \dot{M}_e - \bar{u}\dot{M}_o + \frac{\bar{u}^2}{2}\dot{M}_a - g(\bar{z}\cos\theta - x\sin\theta)\dot{M}_a.
\end{aligned} \tag{B.8}$$

Appendix C

Applicability of numerical models for the front condition

This Chapter is based on a paper published in Progress in Earth and Planetary Science (Shimizu et al., 2017).

As mentioned in Chapter 1, PDCs are characterized by strong density stratification due to particle settling (e.g., Branney & Kokelaar, 2002), whereby a dilute gravity current (particle suspension flow) overrides the dense basal gravity current (fluidized granular flow). The ratio of the density of the dilute current, $\bar{\rho}$, to the ambient air, ρ_{a}, is on the order 10^0–10^1. And, the ratio of the density of the basal dense current, ρ_{H}, to ρ_{a} is on the order 10^2–10^3. If we are to capture the effects of the density ratio (i.e., $\bar{\rho}/\rho_{\mathrm{a}}$ and $\rho_{\mathrm{H}}/\rho_{\mathrm{a}}$), it is important to calculate the front condition (i.e., Eqs. (2.93) and (2.100)) correctly (Ungarish, 2007). In this chapter, we present a numerical method for the front condition for a wide range of the density ratio. In the following sections, we formulate the mathematical problem and show that the numerical treatment of the front condition is key to correctly solving the dynamics of gravity currents for a wide range of the density ratio within the framework of the shallow-water model. We also assess previous numerical methods that have been used to calculate the behavior of the flow front by comparing numerical and analytical results, and we propose a numerical method to simulate the dynamics of gravity

currents for a wide range of the density ratio under various geophysical conditions.

C.1 Formulation

We consider a planar, inviscid, incompressible, immiscible gravity current of density $\rho_{\rm c}$ in a thick ambient fluid of density $\rho_{\rm a}$, as shown in Figure C.1. The current propagates along a smooth horizontal bottom in the positive x^* direction in time t^*, and gravitational acceleration g acts in the negative z^* direction, where asterisks denote dimensional variables although asterisks denote non-dimensional variables in other chapters. The propagating current is initially stationary in a reservoir of length x_0 and height h_0, and propagation occurs after a dam at $x^* = x_0$ is rapidly removed at $t^* = 0$. The boundary at $x^* = 0$ is a rigid wall. The flow front at $x^* = x^*_{\rm N}(t^*)$ is affected by the resistance of the ambient fluid, where $\rm N$ denotes the front. This problem is referred to as the "dam-break problem" (e.g., Ungarish, 2009), and is a simple geophysical scenario.

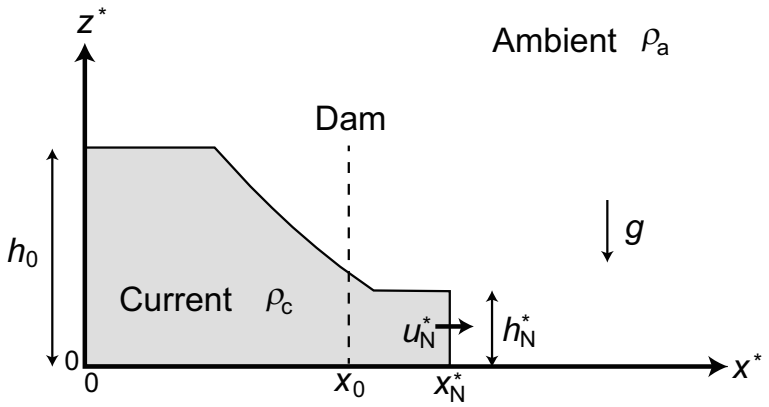

Figure C.1: Schematic of the gravity current released from a dam in a thick ambient fluid. Although asterisks denote non-dimensional variables in other chapters, asterisks denote dimensional variables in this chapter.

We assume that the current is shallow, with $h_0/x_0 \ll 1$, and is in hydrostatic equilibrium in the vertical direction (i.e., the shallow-water approximation). In the shallow-water approximation, we can obtain the vertically averaged conservation equations of mass and

momentum for the flow interior $x^* < x^*_{\rm N}$ (e.g., Ungarish, 2007) as follows:

$$\frac{\partial h^*}{\partial t^*} + \frac{\partial}{\partial x^*}(u^* h^*) = 0, \tag{C.1}$$

$$\frac{\partial}{\partial t^*}(u^* h^*) + \frac{\partial}{\partial x^*}\left(u^{*2} h^* + \frac{1}{2}\frac{\rho_{\rm c} - \rho_{\rm a}}{\rho_{\rm c}} g h^{*2}\right) = 0, \tag{C.2}$$

where $h(x,t)$ is the local height and $u(x,t)$ is the local horizontal velocity.

At the flow front $x^* = x^*_{\rm N}(t^*)$, the kinematic condition ($\mathrm{d}x^*_{\rm N}/\mathrm{d}t^* = u^*_{\rm N}$) and the mass and momentum equations should be taken into account. In addition, to describe realistic gravity current dynamics, we must consider a quasi-steady balance between the buoyancy pressure driving the current front ($\sim (\rho_{\rm c} - \rho_{\rm a}) g h^*_{\rm N}$) and the resistance pressure caused by the acceleration of the ambient fluid around the front ($\sim \rho_{\rm a} u^{*2}_{\rm N}$). This condition is known as the front condition, and can be written as follows (e.g., Ungarish, 2007):

$$u^*_{\rm N} = Fr_{\rm N0}\sqrt{\frac{\rho_{\rm c} - \rho_{\rm a}}{\rho_{\rm a}} g h^*_{\rm N}} \qquad \text{at} \quad x^* = x^*_{\rm N}(t^*), \tag{C.3}$$

where $Fr_{\rm N0}$, which is an imposed frontal Froude number, is assumed to be a constant of order 10^0 (e.g., $\sqrt{2}$; Benjamin, 1968).

Here, using x_0 as the length scale and h_0 as the height scale, we rewrite all dimensional variables to dimensionless variables as follows:

$$x = x^*/x_0, \quad h = h^*/h_0, \quad u = u^*/U, \quad t = t^*/T, \tag{C.4}$$

with

$$U = \sqrt{\frac{\rho_{\rm c} - \rho_{\rm a}}{\rho_{\rm c}} g h_0}, \quad T = x_0/U. \tag{C.5}$$

Applying this scaling to Eqs. (C.1)–(C.3), we obtain

$$\frac{\partial}{\partial t}\boldsymbol{q} + \frac{\partial}{\partial x}\boldsymbol{f} = \boldsymbol{0} \tag{C.6}$$

$$u_{\mathrm{N}} = Fr_{\mathrm{N0}}\sqrt{\rho_{\mathrm{c}}/\rho_{\mathrm{a}}}\sqrt{h_{\mathrm{N}}} \qquad \text{at} \quad x = x_{\mathrm{N}}(t) \tag{C.7}$$

with

$$\boldsymbol{q} = \begin{pmatrix} h \\ uh \end{pmatrix}; \quad \boldsymbol{f} = \begin{pmatrix} uh \\ u^2h + \frac{1}{2}h^2 \end{pmatrix}. \tag{C.8}$$

Note that the density ratio $\rho_{\mathrm{c}}/\rho_{\mathrm{a}}$ is included only in the front condition (C.7). Hence, to capture the effects of $\rho_{\mathrm{c}}/\rho_{\mathrm{a}}$, it is important to calculate the front condition correctly (Ungarish, 2007).

The behavior of the analytical solutions for the above equations depends on $\rho_{\mathrm{c}}/\rho_{\mathrm{a}}$ (Figure C.2; Ungarish, 2007). The analytical solutions of the dam-break problem consist of an initial "slumping" stage and a subsequent "self-similar" stage (Figure C.2a; e.g., Hogg, 2006). During the slumping stage, the front moves with a constant speed and height. During this stage, an initial backward-propagating rarefaction wave arises from the rapidly removed dam, and then a wave arises from the reflection of this rarefaction wave at the back wall $x = 0$ at $t = 1$. The slumping stage continues until the front is caught by this reflection wave. After the slumping stage, the solution is asymptotic to a self-similar solution as time tends to infinity (i.e., the self-similar stage). During this stage, the velocity and height of the front decrease with time. The dependence of the solution on $\rho_{\mathrm{c}}/\rho_{\mathrm{a}}$ is clearly observed in the behavior of the flow front. When $\rho_{\mathrm{c}}/\rho_{\mathrm{a}} \sim 10^0$, the front height h_{N} is on the order of 10^{-1} during the slumping stage and in the early self-similar stage (Figure C.2a). On the other hand, when $\rho_{\mathrm{c}}/\rho_{\mathrm{a}} \sim 10^3$, h_{N} is much smaller than 10^{-1}, even from the beginning, and the front velocity u_{N} is substantially greater than u_{N} for $\rho_{\mathrm{c}}/\rho_{\mathrm{a}} \sim 10^0$ (Figure C.2b). These differences can be interpreted as follows: the momentum lost due to the resistance of the ambient fluid at the front becomes less

significant with respect to the momentum of the current as $\rho_{\rm c}/\rho_{\rm a}$ increases. We aim to numerically reproduce these features of the analytical solution below.

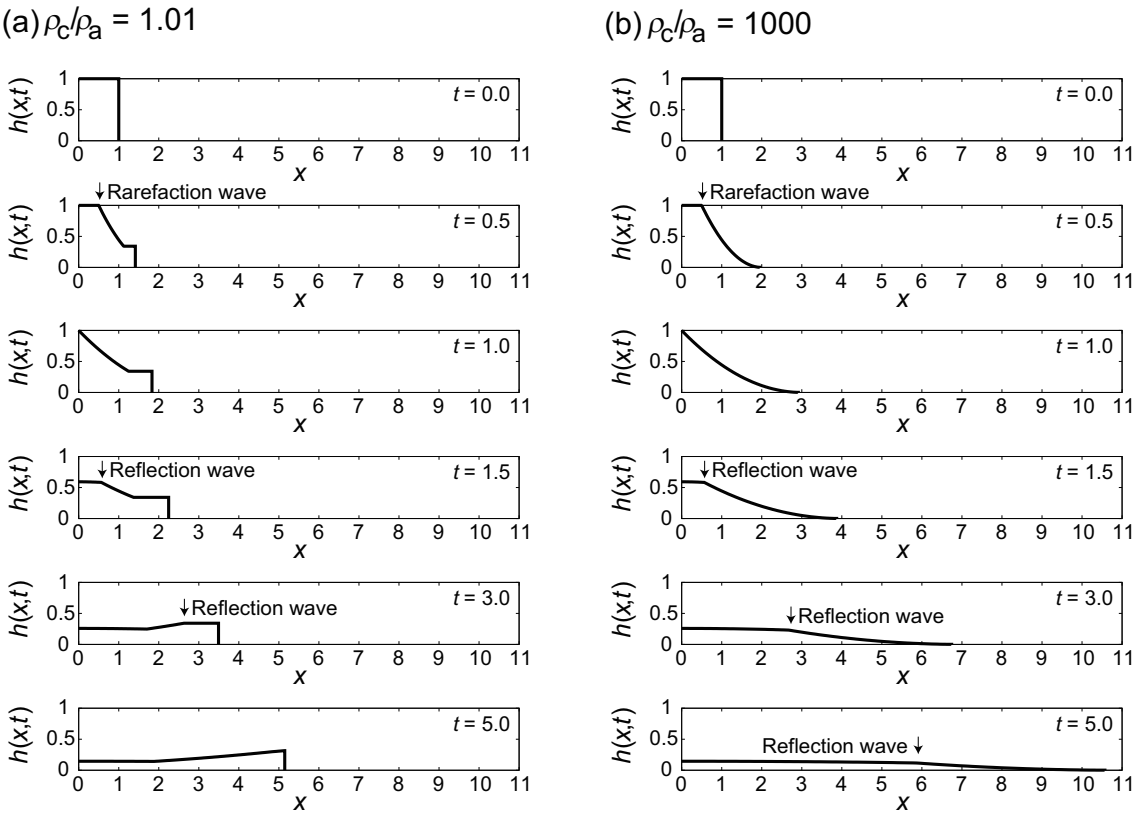

Figure C.2: Analytical solutions of $h(x,t)$ for the dam-break problem. Here, $Fr_{\rm N0} = \sqrt{2}$ (Benjamin, 1968) is used. (a) $\rho_{\rm c}/\rho_{\rm a} = 1.01$. (b) $\rho_{\rm c}/\rho_{\rm a} = 1000$. In (a), the currents at $t = 0.5$, 1.0, 1.5, and 3.0 are in the slumping stage, and the current at $t = 5.0$ is in the self-similar stage. The initial backward-propagating rarefaction wave arising from the rapidly removed dam travels toward the back wall $x = 0$ (see the profile at $t = 0.5$), reaching the wall at $t = 1.0$. Then, a wave arises from the reflection of the rarefaction wave and travels toward the front (see the profiles at $t = 1.5$ and 3.0). After the front is caught by this reflection wave, the current is in the self-similar stage (see the profile at $t = 5.0$). In (b), all the currents are in the slumping stage. In this case (i.e., $\rho_{\rm c}/\rho_{\rm a} = 1000$), the slumping stage continues until $t \sim 226$ (see Hogg (2006) for details).

C.2 Numerical methods

In this chapter, we developed a numerical method for modeling gravity currents for a wide range of $\rho_{\rm c}/\rho_{\rm a}$ by discretizing the dimensionless mass and momentum conservation equations (Eqs. (C.6) and (C.8)). As these equations are nonlinear and hyperbolic, shocks

may develop in the currents. Consequently, we used a finite volume method with shock capturing capability (e.g., Toro, 2001; LeVeque, 2002). The finite volume method updates a piecewise constant function $\boldsymbol{Q}_i^n$ that approximates the average value of the solution $\boldsymbol{q}$ in each grid cell i at time step n, using the expression

$$\boldsymbol{Q}_i^{n+1} = \boldsymbol{Q}_i^n - \frac{\Delta t}{\Delta x}(\boldsymbol{F}_{i+1/2} - \boldsymbol{F}_{i-1/2}), \tag{C.9}$$

where Δx is the constant cell length, and Δt is the time interval. $\boldsymbol{F}_{i+1/2}$, which is the intercell flux between cells i and $i+1$, is obtained by using an exact Riemann solver or an approximate Riemann solver, such as the Roe scheme (e.g., Toro, 2001; LeVeque, 2002). The time interval Δt is limited by the Courant–Friedrichs–Lewy condition (e.g., Toro, 2001; LeVeque, 2002).

As mentioned above, if we are to capture the effects of $\rho_\mathrm{c}/\rho_\mathrm{a}$, it is important to calculate the front condition (C.7) correctly. Previously, two types of numerical models have been proposed to calculate the front condition. In one, the front condition is calculated as a boundary condition at each time step (e.g., Ungarish, 2009). We refer to this model as the Boundary Condition (BC) model (Figure 3.1a). In the other, the front condition is calculated by setting a thin artificial bed ahead of the front (e.g., Toro, 2001). We refer to this as the Artificial Bed (AB) model (Figure 3.1b). In the AB model, the resistance of the ambient fluid at the flow front is modeled by the reaction of the force pushing the artificial bed at the flow front. These models will be described below.

C.2.1 Boundary Condition (BC) model

In the BC model, three quantities at the flow front (x_N, h_N, and u_N) are calculated as boundary conditions of the current from the three equations (mass and momentum conservation equations and front condition) at each time step. In the present numerical method, because we apply a fixed spatial coordinate with constant Δx, the front position $x = x_\mathrm{N}(t)$ generally does not coincide with the margins of the grid cells. We therefore

define the cell that includes the front as the front cell ($i = FC(t)$, where $FC(t)$ is an integer), and the width of the region that the current occupies in the front cell as $\Delta x_{FC}(t)$ ($0 \leq \Delta x_{FC}(t) < \Delta x$; see Figure 3.2). Using $FC(t)$ and $\Delta x_{FC}(t)$, we can write the front position as

$$x_{\mathrm{N}}(t) = (FC(t) - 1)\Delta x + \Delta x_{FC}(t). \tag{C.10}$$

The values of h_{N} and u_{N} are approximated by the values of h and u at the front cell (i.e., h_{FC} and u_{FC}).

When the kinematic condition ($\mathrm{d}x_{\mathrm{N}}/\mathrm{d}t = u_{\mathrm{N}}$) is taken into account, the discretized equations for mass and momentum conservation at the flow front are given by

$$\Delta x_{FC}^{n+1} h_{FC}^{n+1} = \Delta x_{FC}^{n} h_{FC}^{n} + \Delta t f_1 \tag{C.11}$$

and

$$\Delta x_{FC}^{n+1} (uh)_{FC}^{n+1} = \Delta x_{FC}^{n} (uh)_{FC}^{n} + \Delta t \left(f_2 - \frac{1}{2} (h_{FC}^{n+1})^2 \right), \tag{C.12}$$

respectively, where $(f_1, f_2)^T$ represents the intercell flux $\boldsymbol{F}_{FC-1/2}$. From the front condition (i.e., Eq. (C.7)) we obtain

$$\frac{(uh)_{FC}^{n+1}}{h_{FC}^{n+1}} = Fr_{\mathrm{N0}} \sqrt{\rho_{\mathrm{c}}/\rho_{\mathrm{a}}} \sqrt{h_{FC}^{n+1}}. \tag{C.13}$$

Solving these three equations analytically (e.g., using Ferrari's method for the solution of the quartic equation) or numerically (e.g., using the Newton–Raphson iteration method), we obtain h_{FC}^{n+1}, u_{FC}^{n+1}, and Δx_{FC}^{n+1}, and hence, h_{N}, u_{N}, and x_{N} at each time step.

C.2.2 Artificial Bed (AB) model

In the AB model, the conservation equations (Eqs. (C.6) and (C.8)) are numerically solved using a shock capturing method for not only the interior, but also the outside of the current by *a priori* setting a thin artificial bed ahead of the front. Through this numerical procedure, the flow front is generated as the flow following a shock formed ahead of the front without any additional calculation (see Figure 3.1b). In this model, the thickness of the artificial bed (ε in Figure 3.1b) is the parameter that controls the front condition (i.e., the values of $h_{\rm N}$ and $u_{\rm N}$ for different values of $\rho_{\rm c}/\rho_{\rm a}$; see section 10.8 in Toro (2001)).

Here, we analytically determined the relationship between ε and $\rho_{\rm c}/\rho_{\rm a}$, as well as that between $u_{\rm N}$ and ε, on the basis of the analytical solution for the slumping stage of the dam-break problem (e.g., Toro, 2001; LeVeque, 2002; Ungarish, 2009). The initial conditions are $h = 1$ and $u = 0$ in the domain $0 \leq x \leq 1$, and $h = \varepsilon$ and $u = 0$ in the domain $x > 1$, at $t = 0$. Let us consider the time evolution of the current before the rarefaction wave reaches the back wall $x = 0$ (i.e., $0 < t \leq 1$).

For hyperbolic equations such as those used in the present system (i.e., Eqs. (C.6) and (C.8)), the relationships between the variables (i.e., h and u) on the characteristics $c_{\pm} = u \pm \sqrt{h}$ are represented as follows:

$$\Gamma_{\pm} = u \pm 2\sqrt{h} = \text{const} \qquad \text{on} \quad \frac{{\rm d}x}{{\rm d}t} = c_{\pm}, \tag{C.14}$$

where $\Gamma_{\pm}$ are the "Riemann Invariants". Considering that c_{+} from the domain with one initial condition ($h = 1, u = 0$) enter the front domain ($h = h_{\rm N}$, $u = u_{\rm N}$), we can obtain

$$u_{\rm N} = 2(1 - \sqrt{h_{\rm N}}) \tag{C.15}$$

from Eq. (C.14). The equation provides the relationship between $h = h_{\rm N}$ and $u = u_{\rm N}$ inside the current.

On the other hand, when an artificial bed with $h = \varepsilon$ and $u = 0$ is set, a shock wave

traveling with speed S occurs ahead of the front. Across this shock wave, the Rankine–Hugoniot condition,

$$\boldsymbol{f}(\boldsymbol{q}_{\mathrm{R}}) - \boldsymbol{f}(\boldsymbol{q}_{\mathrm{L}}) = S(\boldsymbol{q}_{\mathrm{R}} - \boldsymbol{q}_{\mathrm{L}}) \tag{C.16}$$

should hold. Here, the subscript R denotes the state on the right side of the shock and L denotes the state on the left side. From Eq. (C.16), we obtain the state of the front domain behind the shock (i.e., the relationship between $h = h_{\mathrm{N}}$ and $u = u_{\mathrm{N}}$) as

$$u_{\mathrm{N}} = (h_{\mathrm{N}} - \varepsilon)\sqrt{\frac{1}{2}\left(\frac{h_{\mathrm{N}} + \varepsilon}{h_{\mathrm{N}}\varepsilon}\right)}, \tag{C.17}$$

and the shock speed as

$$S = \sqrt{\frac{1}{2}\frac{(h_{\mathrm{N}} + \varepsilon)h_{\mathrm{N}}}{\varepsilon}}. \tag{C.18}$$

Eliminating h_{N} from Eqs. (C.15), (C.17), and (C.18), we obtain u_{N} and S as a function of ε (Figure C.3a). Using the front condition (C.7) as well as these equations, we also obtain the relationship between the artificial bed thickness ε and the density ratio $\rho_{\mathrm{c}}/\rho_{\mathrm{a}}$ (Figure C.3b) as

$$\begin{aligned}\left(1 - \frac{2}{Fr_{\mathrm{N0}}\sqrt{\rho_{\mathrm{c}}/\rho_{\mathrm{a}}} + 2}\right)\frac{4\sqrt{2\varepsilon}}{Fr_{\mathrm{N0}}\sqrt{\rho_{\mathrm{c}}/\rho_{\mathrm{a}}} + 2} \\ = \left\{\left(\frac{2}{Fr_{\mathrm{N0}}\sqrt{\rho_{\mathrm{c}}/\rho_{\mathrm{a}}} + 2}\right)^2 - \varepsilon\right\}\sqrt{\left(\frac{2}{Fr_{\mathrm{N0}}\sqrt{\rho_{\mathrm{c}}/\rho_{\mathrm{a}}} + 2}\right)^2 + \varepsilon}.\end{aligned} \tag{C.19}$$

Note that because we use Eq. (C.15) here, these relationships (Figure C.3) are in the slumping stage.

In Figure C.3a, S is larger than the front velocity, u_{N}, because of the accumulation of the artificial bed at the flow front (see Figure 3.1b). This deviation of S from u_{N} is substantial for $\varepsilon \gtrsim 10^{-3}$. This implies that the position of the shock does not always

approximate the flow front. If we are to extract the correct position of the flow front, we must calculate an advection equation for a passive tracer concentration, ϕ ($\phi = 1$ for $0 \leq x \leq 1$, and $\phi = 0$ for $x > 1$, at $t = 0$):

$$\frac{\partial \phi}{\partial t} + u \frac{\partial \phi}{\partial x} = 0 \tag{C.20}$$

after solving the equations of fluid motion (see section 13.12 in LeVeque (2002) for details).

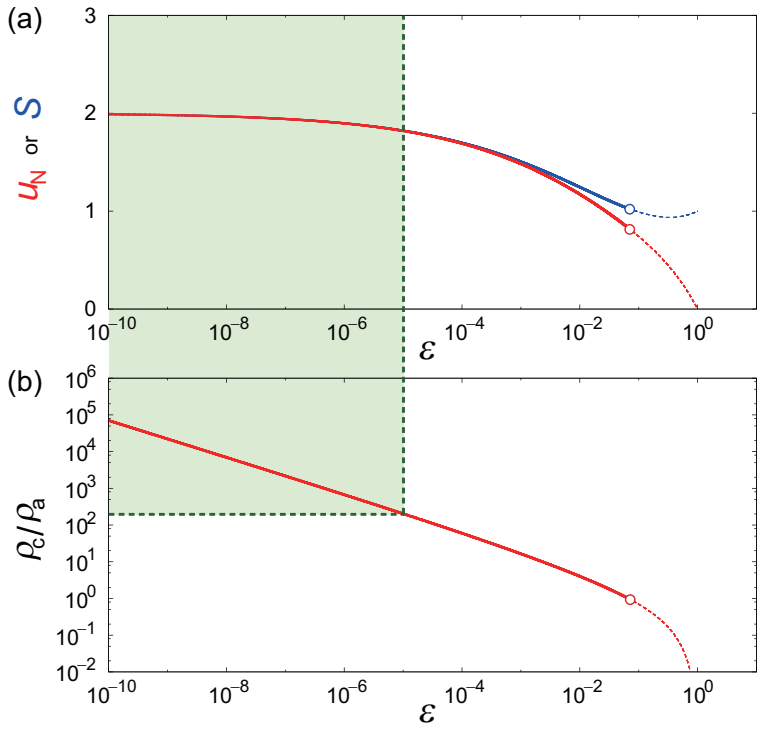

Figure C.3: Analytical solutions for the AB model during the slumping stage. (a) Front velocity $\bar{u}_{\mathrm{N}}$ (red curve) and shock speed S (blue curve), as functions of ε. (b) Relationship between ε and $\rho_{\mathrm{c}}/\rho_{\mathrm{a}}$, in which $Fr_{\mathrm{N0}} = \sqrt{2}$ (Benjamin, 1968) is used. Dashed curves represent the solutions for $\rho_{\mathrm{c}}/\rho_{\mathrm{a}} < 1$.

C.3 Comparison of analytical and numerical results

In this section, we compare the numerical results obtained from the BC and AB models with the analytical results, and assess the applicability of these models.

Figure C.4 shows the numerical results from the BC model along with the analytical results for the cases of $\rho_{\rm c}/\rho_{\rm a} = 1.01$ (a) and 1000 (b). The numerical results for $\rho_{\rm c}/\rho_{\rm a} = 1.01$ agree well with the analytical results from the early slumping stage to the late self-similar stage. The numerical results for $\rho_{\rm c}/\rho_{\rm a} = 1000$ also appear to agree with the analytical results, but the speed of the front position, $\dot{x}_{\rm N}$, shows a numerical oscillation that is not observed in the analytical result (Figure C.5a). In particular, in the initial stage ($t \lesssim 0.0002$ in Figure C.5a), $\dot{x}_{\rm N}$ tends to be overestimated. These oscillation and overestimation are caused by the assumption that the values of h_{FC} and u_{FC} are uniform across the width of the front cell Δx_{FC} in the present numerical method at first-order accuracy. For a large $\rho_{\rm c}/\rho_{\rm a}$, because $h_{\rm N}$ has a small value, the value of Δx_{FC} tends to be overestimated when a constant h_{FC} is assumed (Figure C.5b). We suggest, therefore, that the BC model is favorable for simulating gravity currents with relatively low $\rho_{\rm c}/\rho_{\rm a}$.

Figure C.6 shows the numerical results from the AB model along with the analytical results. In these calculations, the values of ε for given values of $\rho_{\rm c}/\rho_{\rm a}$ are set based on the relationship of Eq. (C.19) (see Figure C.3b). In Figure C.6b, the numerical results for $\rho_{\rm c}/\rho_{\rm a} = 1000$ ($\varepsilon = 4.58 \times 10^{-7}$) agree well with the analytical results. The numerical oscillations observed in the BC model do not occur with the AB model (Figure C.5a). In Figure C.6a, on the other hand, the numerical results for $\rho_{\rm c}/\rho_{\rm a} = 1.01$ ($\varepsilon = 6.58 \times 10^{-2}$) agree well with the analytical results only during the slumping stage ($t \lesssim 4.5$), but deviate from the analytical results during the self-similar stage ($t \gtrsim 4.5$). This agreement during the slumping stage and deviation during the self-similar stage occurs because ε is set using the analytical relationship (Eq. (C.19)) for the slumping stage of the dam-break problem. During the slumping stage, $h_{\rm N}$ and $u_{\rm N}$ are constant so that ε based on Eq. (C.19) provides the correct front condition. During the self-similar stage, on the other hand, the driving pressure, and hence $h_{\rm N}$ and $u_{\rm N}$, decrease with time; therefore, the assumed value of ε is no longer consistent with the front condition Eq. (C.7).

The good agreement in the results of the AB model for $\rho_{\rm c}/\rho_{\rm a} = 1000$ reflects the fact that the dynamics of the gravity current becomes insensitive to the front condition

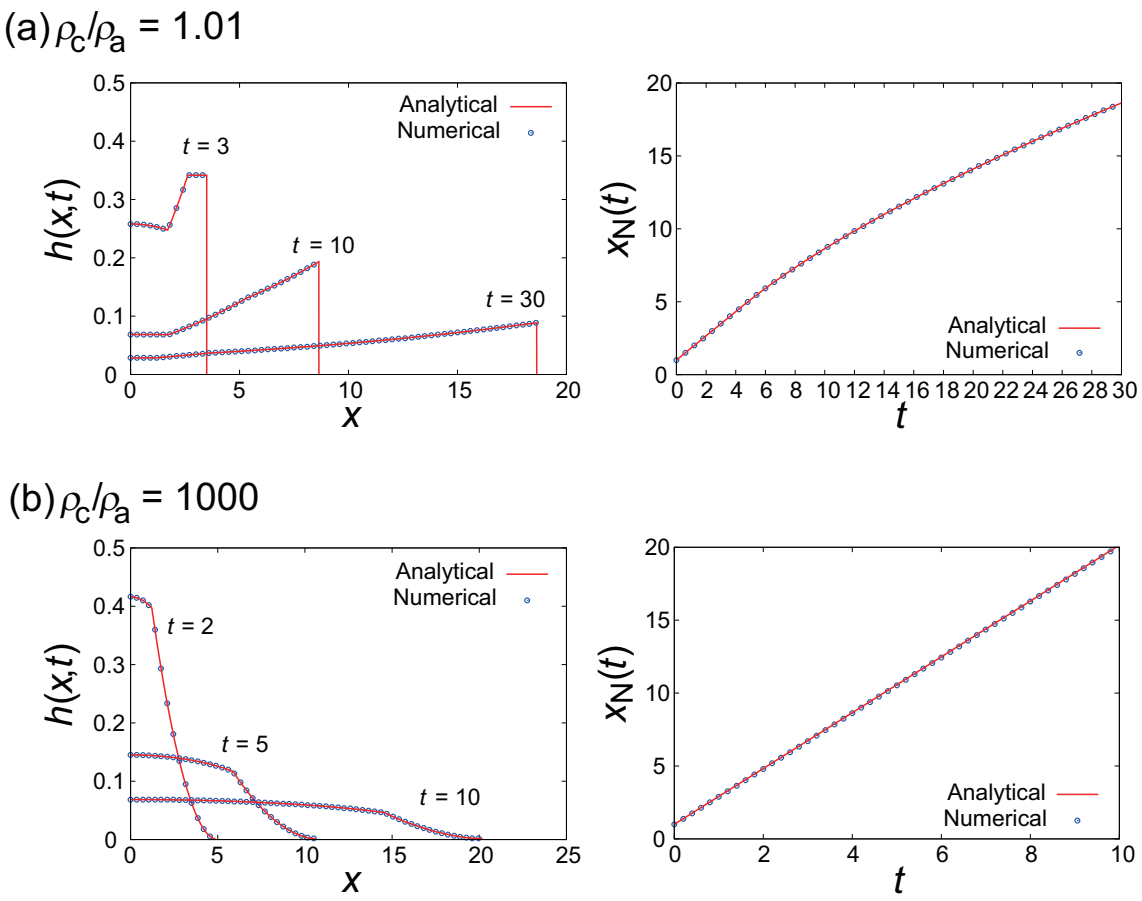

Figure C.4: Analytical results (red curves) and numerical results from the BC model (blue symbols) for $h(x,t)$ and $x_{\rm N}$. (a) $\rho_{\rm c}/\rho_{\rm a} = 1.01$. (b) $\rho_{\rm c}/\rho_{\rm a} = 1000$.

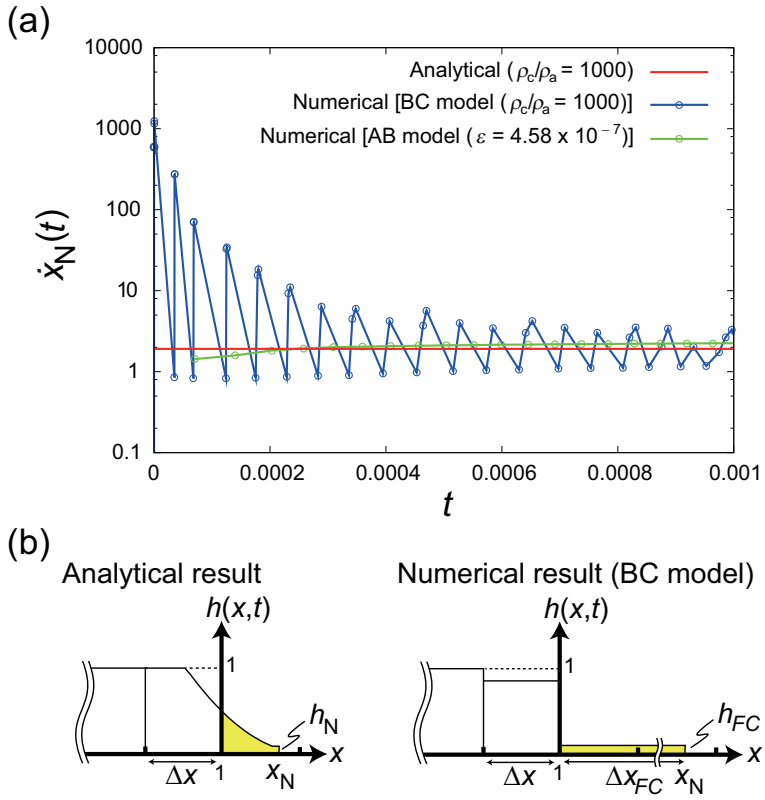

Figure C.5: Speed of the front position, $\dot{x}_{\rm N}$, in the early time steps. (a) Comparisons between the analytical result with $\rho_{\rm c}/\rho_{\rm a} = 1000$ (red line) and numerical results of the BC model with $\rho_{\rm c}/\rho_{\rm a} = 1000$ (blue symbols) and of the AB model with $\varepsilon = 4.58 \times 10^{-7}$ (green symbols). In the numerical calculations, $\Delta x = 1.0 \times 10^{-4}$. (b) Illustrations of the overestimation of $\dot{x}_{\rm N}$ by the BC model in $t \lesssim 0.0002$ in (a).

for large values of ρ_c/ρ_a. In Figure C.3b, ε approaches 0 as ρ_c/ρ_a increases. In the limit as $\rho_c/\rho_a \to \infty$ and $\varepsilon \to 0$, u_N asymptotically approaches its maximum value, 2, and h_N asymptotically approaches 0. For sufficiently small ε, the solution converges to that in the limit as $u_N \to 2$ and $h_N \to 0$, and it becomes insensitive to the value of ε (see Figure C.3a). Indeed, as shown in Figure C.6b, we can confirm that the result of the AB model with a very small ε ($\varepsilon = 1.0 \times 10^{-10}$) is indistinguishable from that for $\rho_c/\rho_a = 1000$ ($\varepsilon = 4.58 \times 10^{-7}$). According to Figure C.3, the results of the AB model for the dam-break problem are insensitive to ε when $\varepsilon \lesssim 10^{-5}$, which corresponds to $\rho_c/\rho_a \gtrsim 10^2$ (Figure C.3b). Consequently, we suggest that the AB model is favorable for simulating gravity currents with high ρ_c/ρ_a for which the dynamics of the current is insensitive to the assumed value of ε.

C.4 Applicability of the BC and AB models

Our results indicate that the BC and AB models each have their own advantages and disadvantages. The results obtained from the BC model agree well with the analytical results when $\rho_c/\rho_a \lesssim 10^2$ (Figure C.4a), whereas they show a numerical oscillation at the flow front and tend to overestimate the front speed when $\rho_c/\rho_a \gtrsim 10^2$ (Figure C.5). No such numerical oscillation nor overestimation is observed in the results from the AB model. For currents with $\rho_c/\rho_a \gtrsim 10^2$, the AB model provides good approximations of the analytical results, given a sufficiently small ε (Figures C.3 and C.6b). For currents with $\rho_c/\rho_a \lesssim 10^2$, however, the AB model may fail to reproduce the analytical results for currents where the height and speed of the front change with time (Figure C.6a). Accordingly, we propose that the BC model should be used for currents with $\rho_c/\rho_a \lesssim 10^2$ and the AB model is applicable only to currents with $\rho_c/\rho_a \gtrsim 10^2$.

Because of its simple coding and numerical stability, the AB model with an arbitrarily small ε is commonly used for simulations of gravity currents in many geophysical situations (e.g., Denlinger & Iverson, 2004; Larrieu et al., 2006; Doyle et al., 2007, 2008,

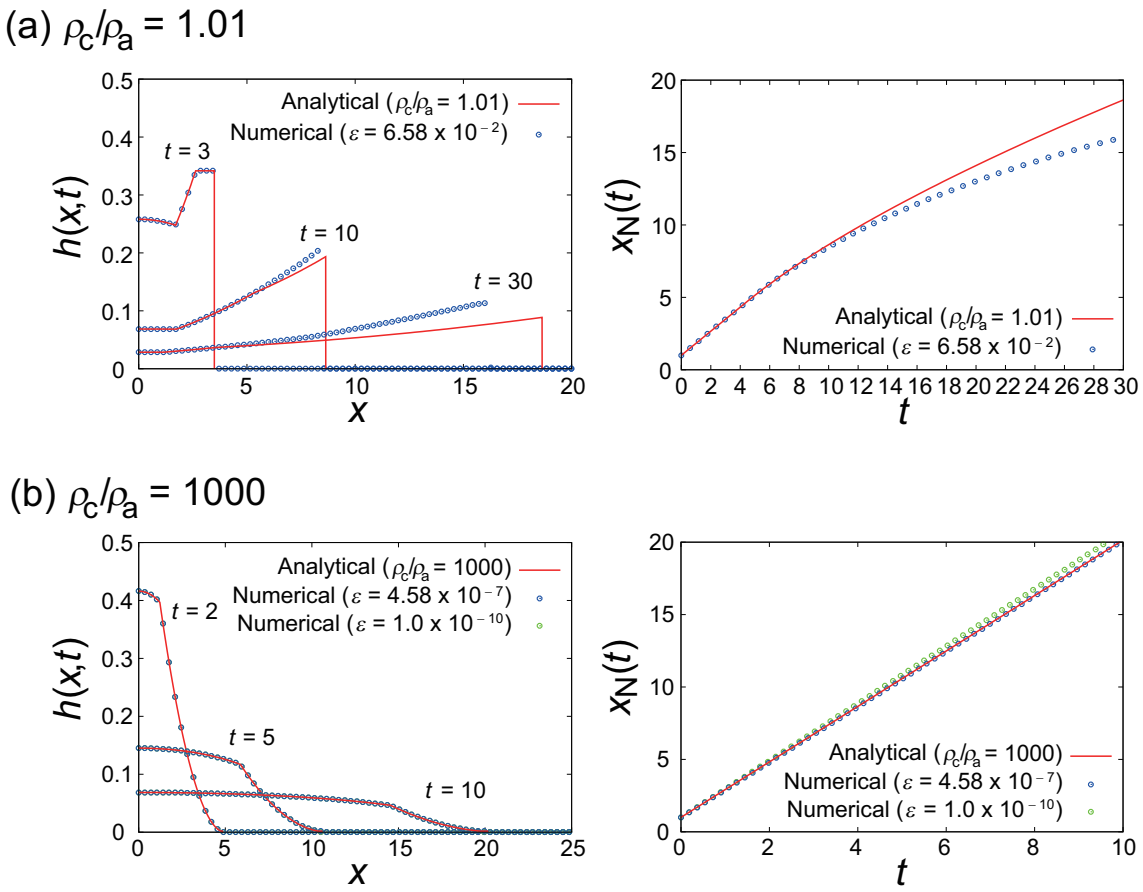

Figure C.6: Analytical results (red curves) and numerical results from the AB model (symbols) for $h(x,t)$ and x_{N}. (a) $\rho_{\mathrm{c}}/\rho_{\mathrm{a}} = 1.01$. (b) $\rho_{\mathrm{c}}/\rho_{\mathrm{a}} = 1000$. In the numerical results, blue symbols represent the numerical results given ε based on the analytical solution during the slumping stage ((a) $\varepsilon = 6.58 \times 10^{-2}$; (b) $\varepsilon = 4.58 \times 10^{-7}$). Green symbols represent the numerical results given $\varepsilon = 1.0 \times 10^{-10}$.

2011). This model would be applicable in simulating gravity currents with high values of $\rho_{\rm c}/\rho_{\rm a}$, such as debris flows (e.g., Denlinger & Iverson, 2004). However, our results suggest that it may provide inaccurate results for gravity currents with $\rho_{\rm c}/\rho_{\rm a} \lesssim 10^2$, such as turbidity currents and dilute pyroclastic density currents. Numerical results for $\rho_{\rm c}/\rho_{\rm a} = 10$ show that the problem arises mainly from the behavior of the flow front (Figure C.7). Generally, a gravity current with a relatively low value of $\rho_{\rm c}/\rho_{\rm a}$ is characterized by the formation of a large front height, which is caused by the resistance of the ambient fluid. This large front height is successfully reproduced by the BC model (Figure C.7a), while the AB model fails to capture it. The results from the AB model with $\varepsilon = 10^{-10}$ (Figure C.7b) show that the resistance at the front is too small to develop a large front height; consequently, the flow speed is substantially overestimated.

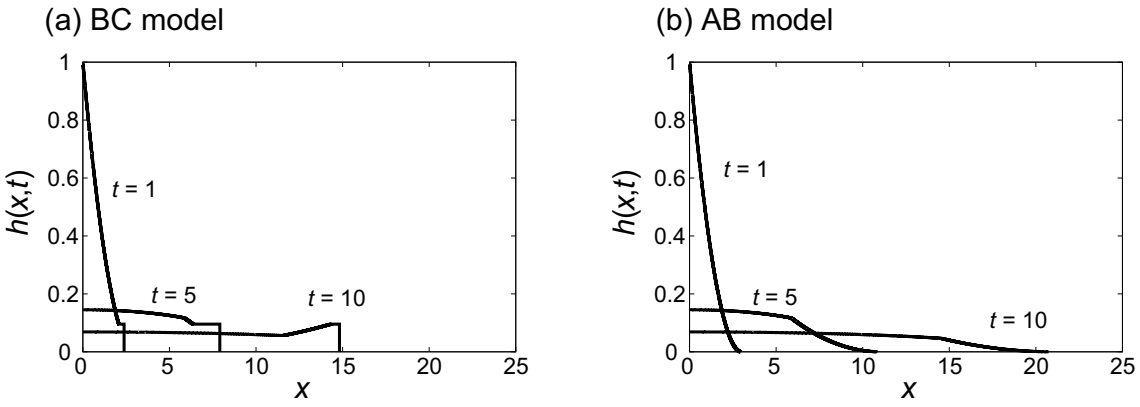

Figure C.7: Numerical results of $h(x,t)$ for $\rho_{\rm c}/\rho_{\rm a}$ = 10. (a) BC model. (b) AB model with $\varepsilon = 1.0 \times 10^{-10}$. In (b), $\rho_{\rm c}/\rho_{\rm a} = 10$ is given when the basic equations (Eqs. (C.1) and (C.2)) are non-dimensionalized using Eqs. (C.4) and (C.5).

C.5 Conclusion of this chapter

A numerical shallow-water model of simulating gravity currents for a wide range of $\rho_{\rm c}/\rho_{\rm a}$ has been proposed. In the model, the effects of varying $\rho_{\rm c}/\rho_{\rm a}$ are taken into account via the front condition. We have assessed two types of numerical models for the front condition (the Boundary Condition (BC) model and the Artificial Bed (AB) model) by comparing

their numerical results with the analytical results. The results from the BC model agree well with the analytical results when $\rho_{\rm c}/\rho_{\rm a} \lesssim 10^2$. In contrast, the AB model generates good approximations of the analytical results for $\rho_{\rm c}/\rho_{\rm a} \gtrsim 10^2$. Therefore, we found that, in two-layer models of pyroclastic density currents (PDCs), the BC model must be used for the overlying dilute part ($\rho_{\rm c}/\rho_{\rm a} = 10^0$–$10^1$) and the AB model can be used for the underlying dense part ($\rho_{\rm c}/\rho_{\rm a} = 10^2$–$10^3$).

Appendix D

Estimation of the characteristic Reynolds numbers in Eqs. (2.87) and (2.99)

In this chapter, to determine the Chézy drag coefficient of the dilute current $C_{\rm dm}$ and that of the dense current $C_{\rm db}$ on the basis of Eqs. (2.87) and (2.99), we estimate characteristic Reynolds number of the dilute current, Re_0, and that of the dense current, $Re_{\rm H0}$.

The characteristic Reynolds number of the dilute current, Re_0, is defined as

$$Re_0 \equiv \frac{\rho_0 \mathcal{U}\mathcal{H}}{\eta}, \tag{D.1}$$

where η is an effective viscosity of the dilute current, ρ_0 is a reference density of the dilute current, $\mathcal{U}$ is a characteristic velocity scale of the dilute current, and $\mathcal{H}$ is a characteristic thickness scale of the dilute current. The effective viscosity η is of the order of 1.0×10^{-6} Pa·s, because the effective viscosity of the dilute current is approximated as the viscosity of gas ($\sim 10^{-6}$ Pa·s) (cf. Iverson, 1997). The density of the dilute current at the collapsing column edge is used as the reference density (see Subsections **??** and **??**, and Section **??**). The characteristic scale of thickness $\mathcal{H}$ and that of velocity $\mathcal{U}$ are given by Eqs. (**??**) and

(**??**), respectively. They depend on the mass eruption rate at the collapsing column edge $\dot{M}_0$ (see Figure **??**). Thus, the characteristic Reynolds number Re_0 depends on the mass eruption rate $\dot{M}_0$ (Figure D.1). When the mass eruption rate $\dot{M}_0$ ranges between 10^3–10^{11} kg/s, the characteristic Reynolds number Re_0 ranges between 10^7–10^{12}.

The characteristic Reynolds number of the dense current, Re_{H0}, is defined as

$$Re_{\mathrm{H0}} \equiv \frac{\rho_{\mathrm{H}} \mathcal{U}_{\mathrm{H}} \mathcal{H}_{\mathrm{H}}}{\eta_{\mathrm{H}}}, \tag{D.2}$$

where η_{H} is the effective viscosity of the dense current, ρ_{H} is the density of the dense current, $\mathcal{U}_{\mathrm{H}}$ is a characteristic velocity scale of the dense current, and $\mathcal{H}_{\mathrm{H}}$ is a characteristic thickness scale of the dense current. We estimate the effective viscosity η_{H}, which is influenced by the presence of particles in the pore gas (cf. Iverson, 1997), using the empirical formula proposed by Thomas (1965) and given by $\eta_{\mathrm{H}} = \eta_{\mathrm{gH}}(1 + 2.5\phi_{\mathrm{sH}} + 10.05\phi_{\mathrm{sH}}^2 + 0.00273\exp(16.6\phi_{\mathrm{sH}}))$, where ϕ_{sH} is the volume fraction of solid particle in the dense current, and η_{gH} is the viscosity of the gas in the dense current and is of the order of 1.0×10^{-6} Pa·s. The characteristic velocity scale $\mathcal{U}_{\mathrm{H}}$ is given by $\mathcal{U}$, because the momentum supplied from the dilute current is the main driving force for the motion of the dense current at least initially. The characteristic thickness scale $\mathcal{H}_{\mathrm{H}}$ is defined as $\frac{n_{\mathrm{s0}}}{n_{\mathrm{sH}}} \frac{\rho_0}{\rho_{\mathrm{H}}} W_{\mathrm{s}} \mathcal{T}$. Here, n_{s0} is the mass fraction of solid particle in the dilute current at the collapsing column edge (see Subsections **??** and **??**, and Section **??**), n_{sH} is the mass fraction of solid particle in the dense current (see Subsection 2.2.2), W_{s} is the particle settling velocity of the dilute current (see Subsection 2.2.1), and $\mathcal{T}$ is the characteristic time scale (Eq. (**??**)). The characteristic scale of velocity $\mathcal{U}_{\mathrm{H}}$ (i.e., $\mathcal{U}$) and that of time $\mathcal{T}$ depend on the mass eruption rate at the collapsing column edge $\dot{M}_0$ (see Figure **??**). Thus, the characteristic Reynolds number Re_{H0} depends on the mass eruption rate $\dot{M}_0$ (Figure D.1). When the mass eruption rate $\dot{M}_0$ ranges between 10^3–10^{11} kg/s and the particle settling velocity W_{s} ranges between 0.3–3 m/s, the characteristic Reynolds number Re_{H0} ranges between 10^6–10^{10}.

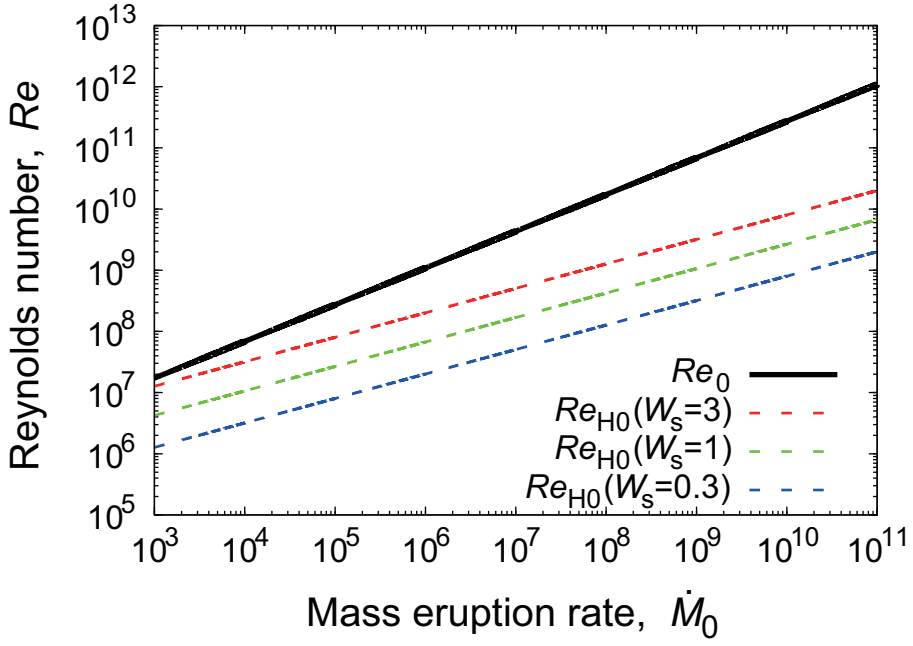

Figure D.1: The characteristic Reynolds numbers vs. the mass eruption rate $\dot{M}_0$. The solid line represents the characteristic Reynolds number of the dilute current, Re_0 (i.e., Eq. (D.1)). The dashed lines represent the characteristic Reynolds number of the dense current, Re_{H0} (i.e., Eq. (D.2)) with $W_\mathrm{s} = 0.3$ (blue), 1.0 (green), and 3.0 (red) m/s.

Appendix E

Verification of a flow-type change depending on the Richardson number at the collapsing column edge Ri_0

本章については、5 年以内に雑誌等で刊行予定のため、非公開。

Appendix F

Supplementary note concerning Bursik & Woods (1996)

Burisk & Woods (1996) investigated the dynamics of dilute PDCs, using a steady one-layer shallow-water model. In Bursik & Woods (1996), all of the equations used to close the system are not explicitly shown, and there are many misprints. Furthermore, we have found that there are two erroneous points in Bursik & Woods (1996). We correct these in this chapter.

F.1 Basic equations of the steady one-layer dilute PDC model

In this section, we show (or modify) the equations explicitly given by Bursik & Woods (1996), and give other equations to close the system. We focus on the case of the currents propagating over a horizontal ground surface (i.e., slope angle $\theta = 0^\circ$) and monodisperse particles.

F.1.1 The equations explicitly given by Bursik & Woods (1996)

In Bursik & Woods (1996), the dilute PDCs spreading both radially and restricted within one-dimensional channel are modeled as a steady highly turbulent, well-mixed, particle-laden suspension flow. The currents are composed of the solid particles, volcanic gas, and the air entrained from ambient. They are influenced by particle settling, entrainment of ambient air, and basal drag.

Bursik & Woods (1996) explicitly shows the following five equations, in which there are eight main unknown variables (bulk density $\bar{\rho}$, depth h, velocity $\bar{u}$, temperature $\bar{T}$, the mass averaged specific heat at constant pressure $\bar{C}_{\mathrm{p}}$, the mass averaged gas constant $\bar{R}$, the mass fraction of the entrained air $\bar{n}_{\mathrm{a}}$, and the mass fraction of solid particles $\bar{n}_{\mathrm{s}}$). The mass conservation equations of one-dimensional channelized current for the particles in the current is written as

$$\frac{\mathrm{d}}{\mathrm{d}x}(\bar{n}_{\mathrm{s}}\bar{\rho}\bar{u}h) = -\bar{n}_{\mathrm{s}}\bar{\rho}W_{\mathrm{s}}, \tag{F.1}$$

where W_{s} is the settling velocity of the particles from the base of the current. The mass conservation equations of one-dimensional channelized current for the bulk is written as

$$\frac{\mathrm{d}}{\mathrm{d}x}(\bar{\rho}\bar{u}h) = \rho_{\mathrm{a}}E|\bar{u}| - \bar{n}_{\mathrm{s}}\bar{\rho}W_{\mathrm{s}}, \tag{F.2}$$

where ρ_{a} is a constant density of ambient air, and E is the entrainment coefficient, given by Eq. (2.83). The momentum conservation equation of one-dimensional channelized current for the bulk is written as

$$\frac{\mathrm{d}}{\mathrm{d}x}\left(\bar{\rho}\bar{u}^2h + \frac{\bar{\rho}-\rho_{\mathrm{a}}}{2}gh^2\right) = -\bar{n}_{\mathrm{s}}\bar{\rho}\bar{u}W_{\mathrm{s}} - \tau_{\mathrm{m}}, \tag{F.3}$$

where τ_{m} is the basal drag. The source terms of this momentum conservation equation represent the momentum lost from the dilute current owing to the particle settling, and

the basal drag. The basal drag is modeled as a Chézy-type drag: $\tau_{\rm m} = C_{\rm dm}\bar{\rho}\bar{u}|\bar{u}|$, where $C_{\rm dm}$ is a Chézy drag coefficient. The energy conservation equation of one-dimensional channelized current for the bulk is written as

$$\frac{\mathrm{d}}{\mathrm{d}x}\left(\bar{\rho}\bar{C}_{\rm p}\bar{T}\bar{u}h + \frac{1}{2}\bar{\rho}\bar{u}^3 h\right) = \rho_{\rm a}E|\bar{u}|C_{\rm pa}T_{\rm a} - \bar{n}_{\rm s}\bar{\rho}W_{\rm s}C_{\rm s}\bar{T}, \tag{F.4}$$

where $\bar{p}$ is the thermodynamic pressure of the dilute current, $C_{\rm s}$ is the specific heat of the solid particles, $C_{\rm pg}$ is the specific heat of volcanic gas at constant pressure, $C_{\rm pa}$ is the specific heat of air at constant pressure, and $T_{\rm a}$ is a constant temperature of ambient air. The thermodynamic pressure $\bar{p}$ is approximated by a constant atmospheric pressure $p_{\rm a0}(\equiv \rho_{\rm a}R_{\rm a}T_{\rm a} = \text{const})$, where $R_{\rm a}$ is the gas constant of air. The source terms of this total energy conservation equation represent the thermal energy gained or lost from the dilute current owing to the entrainment of ambient air and the particle settling. The thermal equation of state is written as

$$\frac{1}{\bar{\rho}} = \frac{\bar{n}_{\rm s}}{\rho_{\rm s}} + \frac{(1-\bar{n}_{\rm s})\bar{R}\bar{T}}{\bar{p}}. \tag{F.5}$$

For radially spreading currents, the following conservation Eqs.:

$$\frac{1}{r}\frac{\mathrm{d}}{\mathrm{d}r}(\bar{n}_{\rm s}\bar{\rho}\bar{u}hr) = -\bar{n}_{\rm s}\bar{\rho}W_{\rm s} \tag{F.6}$$

$$\frac{1}{r}\frac{\mathrm{d}}{\mathrm{d}r}(\bar{\rho}\bar{u}hr) = \rho_{\rm a}E|\bar{u}| - \bar{n}_{\rm s}\bar{\rho}W_{\rm s} \tag{F.7}$$

$$\frac{1}{r}\frac{\mathrm{d}}{\mathrm{d}r}\left(\bar{\rho}\bar{u}^2 hr\right) + \frac{\mathrm{d}}{\mathrm{d}r}\left(\frac{\bar{\rho}-\rho_{\rm a}}{2}gh^2\right) = -\bar{n}_{\rm s}\bar{\rho}\bar{u}W_{\rm s} - \tau_{\rm m} \tag{F.8}$$

$$\frac{1}{r}\frac{\mathrm{d}}{\mathrm{d}r}\left(\bar{\rho}\bar{C}_{\rm p}\bar{T}\bar{u}hr + \frac{1}{2}\bar{\rho}\bar{u}^3 hr\right) = \rho_{\rm a}E|\bar{u}|C_{\rm pa}T_{\rm a} - \bar{n}_{\rm s}\bar{\rho}W_{\rm s} \tag{F.9}$$

are used instead of Eqs. (F.1)–(F.4).

F.1.2 Other equations to close the system

In order to close the system, three other equations are needed. We consider the following three equations: the mass conservation equation of one-dimensional channelized current for the entrained air

$$\frac{\mathrm{d}}{\mathrm{d}x}(\bar{n}_{\mathrm{a}}\bar{\rho}\bar{u}h) = \rho_{\mathrm{a}}E|\bar{u}|, \tag{F.10}$$

the equation of the mass averaged specific heat at constant pressure

$$\bar{C}_{\mathrm{p}} = \bar{n}_{\mathrm{s}}C_{\mathrm{s}} + \bar{n}_{\mathrm{a}}C_{\mathrm{pa}} + (1 - \bar{n}_{\mathrm{s}} - \bar{n}_{\mathrm{a}})C_{\mathrm{pg}}, \tag{F.11}$$

and the equation of the mass averaged gas constant

$$\bar{R} = \frac{\bar{n}_{\mathrm{a}}R_{\mathrm{a}} + (1 - \bar{n}_{\mathrm{s}} - \bar{n}_{\mathrm{a}})R_{\mathrm{g}}}{1 - \bar{n}_{\mathrm{s}}}, \tag{F.12}$$

where R_{g} is the gas constant of volcanic gas.

For radially spreading currents, the following conservation Eq.:

$$\frac{1}{r}\frac{\mathrm{d}}{\mathrm{d}r}(\bar{n}_{\mathrm{a}}\bar{\rho}\bar{u}hr) = \rho_{\mathrm{a}}E|\bar{u}|, \tag{F.13}$$

is used instead of Eq. (F.10).

F.2 Erroneous points in Bursik & Woods (1996)

In order to compare the numerical results of our unsteady two-layer PDC model with the results of the steady one-layer dilute PDC model of Bursik & Woods (1996), we attempted to reproduce the results of Bursik & Woods (1996). In the process, we found that there may be two erroneous points in Bursik & Woods (1996). One is that the boundary temperature at the collapsing column edge, T_0, is not correctly calculated. The other is

that the analytical solutions of the steady runout distances of the current without air entrainment are not correctly written in the text of Bursik & Woods (1996). In this section, we correct the two erroneous points.

F.2.1 The boundary temperature at the collapsing column edge, T_0

Bursik & Woods (1996) calculated the dynamics of the dilute PDCs at steady state, by giving a steady supply of the dilute current from the collapsing column edge as the boundary conditions (see Subsections **??** and **??** for the details). The temperature of the dilute current at the collapsing column edge, T_0, is obtained by conservation of heat between the erupted material of temperature $T_{\rm in}$ and the entrained air of temperature $T_{\rm a}$ (see Eq. (**??**)). We found that, in the results of Bursik & Woods (1996), the boundary temperature at the collapsing column edge, T_0, is not correctly calculated due to inverting the value of the specific heat at constant pressure of air $C_{\rm pa}$ and that of volcanic gas $C_{\rm pg}$. We show the details below.

Bursik & Woods (1996) show the figure of T_0 as a function of mass fraction of gas at the collapsing column edge ($1 - n_{\rm s0}$) on the basis of Eq. (**??**) (see the black solid curves in Figure F.1c; Figure 2b in Bursik & Woods (1996)). In the figure, it is specified that the temperatures of the erupted material $T_{\rm in} = 1200$, 1000 and 800 K are considered. On the other hand, the values of the temperature of ambient air $T_{\rm a}$, the solid particle mass fraction in the erupted material $n_{\rm s,in}$, the specific heat of solid particle $C_{\rm s}$, the specific heat at constant pressure of air $C_{\rm pa}$ and the specific heat at constant pressure of volcanic gas $C_{\rm pg}$ are not specifically shown. To reproduce Figure 2b in Bursik & Woods (1996) (i.e., the black solid curves in Figure F.1c), we give $T_{\rm a} = 273$ K and $n_{\rm s,in} = 0.97$, which is often used as typical values in Bursik & Woods (1996). We also give $C_{\rm s} = 1100$ [J/(kg $\cdot$ K)], $C_{\rm pa} = 1004$ [J/(kg $\cdot$ K)], and $C_{\rm pg} = 1810$ [J/(kg $\cdot$ K)] (e.g., Suzuki et al., 2016; Table. **??**). We substitute these values into Eq. (**??**) to obtain Figure F.1a. Figure 2b in Bursik & Woods (1996) (i.e., the black solid curves in Figure F.1c) is qualitatively

different from Figure F.1a; namely, a upward-convex curve is produced in Figure F.1a whereas a convex-downward curve is produced in Figure 2b in Bursik & Woods (1996) (i.e., the black solid curves in Figure F.1c).

We investigate the cause of the qualitative difference between Figure F.1a and Figure 2b in Bursik & Woods (1996) (i.e., the black solid curves in Figure F.1c). Because the mass fraction of solid particle in the erupted material $n_{\mathrm{s,in}}$ is constant, the increase of the mass fraction of gas at the collapsing column edge, $1 - n_{\mathrm{s0}}$, means the increase of the mass fraction of entrained air at the collapsing column edge, n_{a0} (i.e., $n_{\mathrm{a0}} = 1 - n_{\mathrm{s0}}/n_{\mathrm{s,in}}$; see Subsections **??** and **??** for the details). In Figure F.1a and Figure 2b in Bursik & Woods (1996) (i.e., the black solid curves in Figure F.1c), the boundary temperature at the collapsing column edge, T_0, agrees with the temperatures of the erupted material, T_{in}, when the mass fraction of gas at the collapsing column edge, $1 - n_{\mathrm{s0}}$, is the most smallest (i.e., $n_{\mathrm{a0}} = 0$). Because we give C_{pa} smaller than C_{pg} and C_{s}, n_{a0} should be remarkably large to significantly cool the mixture at the collapsing column edge. Accordingly, the upward-convex curve in Figure F.1a is consistent with physical intuition. In fact, the results inverting the value of the specific heat at constant pressure of air C_{pa} and that of volcanic gas C_{pg} (Figure F.1b) agree well with Figure 2b in Bursik & Woods (1996) (see Figure F.1c). We also mathematically proved that Eq. (**??**) as a function of mass fraction of gas at the collapsing column edge ($1 - n_{\mathrm{s0}}$) must produce a upward-convex curve in the case of $C_{\mathrm{pa}} < C_{\mathrm{pg}}$ and $C_{\mathrm{pa}} < C_{\mathrm{s}}$ (the details are not presented here). Thus, the boundary temperature at the collapsing column edge, T_0, may not correctly calculated due to inverting the value of the specific heat at constant pressure of air C_{pa} and that of volcanic gas C_{pg}, in Figure 2b of Bursik & Woods (1996) (i.e., the black solid curves in Figure F.1c).

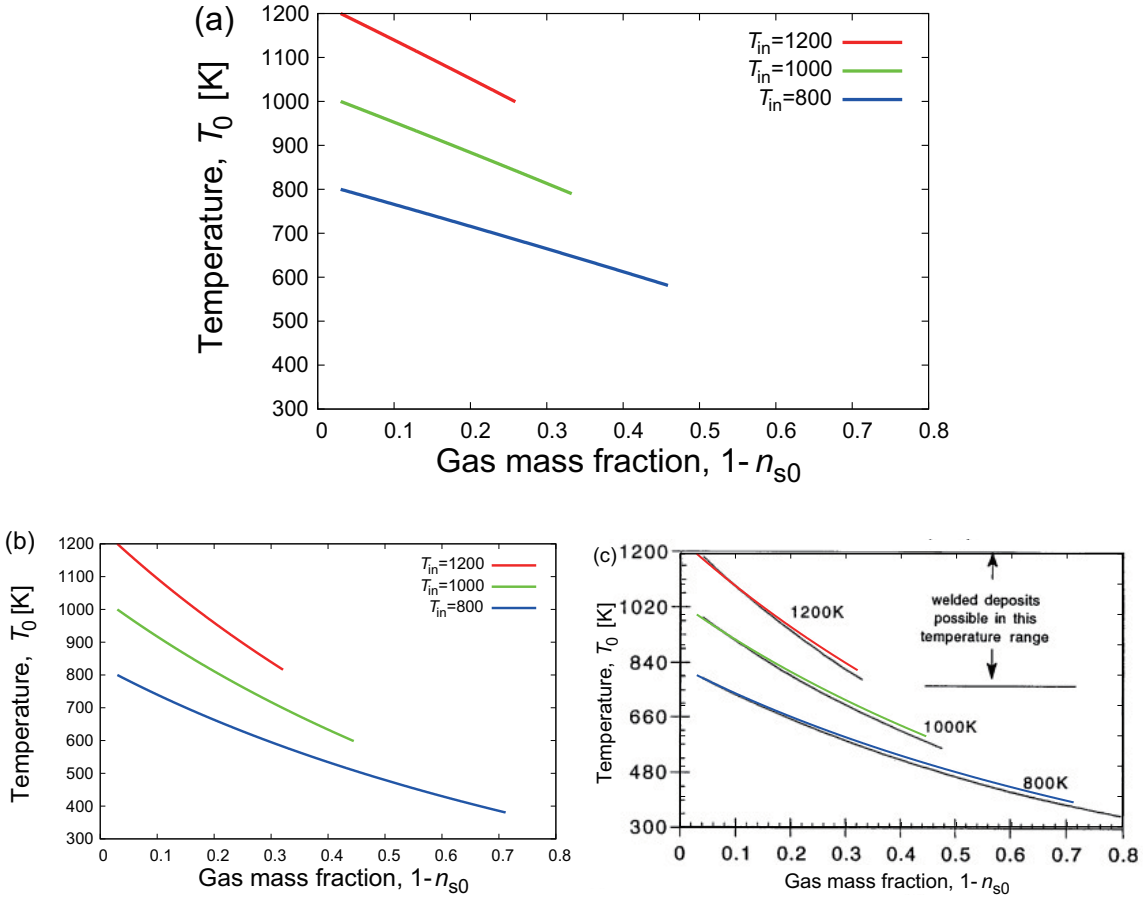

Figure F.1: The boundary temperature at the collapsing column edge, T_0, as a function of the gas mass fraction in the current at the collapsing column edge ($1 - n_{s0}$). The solid particle mass fraction in the erupted material $n_{s,in} = 0.97$; the temperature of the erupted material $T_{in} = 800$ K (blue), 1000 K (green), 1200 K (red). (a) the values of C_{pa} and C_{pg} are correctly given (see Table **??**); (b) the values of C_{pa} and C_{pg} are inverted; (c) (b) is superposed on Figure 2b of Bursik & Woods (1996).

F.2.2 Analytical solutions of steady runout distance without entrainment effect

Bursik & Woods (1996) approximately derived analytical solutions of the steady runout distance of the steady dilute PDCs without air entrainment. We found that the analytical solutions are not correctly written in Bursik & Woods (1996). We show the details below.

Radially spreading currents

We derive the analytical solution of the steady runout distance of the radially spreading dilute PDCs without air entrainment. Then, we compare the analytical solution derived by us with that written in Bursik & Woods (1996).

Assuming that the rate of entrainment of ambient air is negligible, the volume flux of the current $\dot{V}(\equiv 2\pi\bar{u}hr)$, the temperature of the current $\bar{T}$ and the gas constant of the current $\bar{R}$ remain approximately constant along the length of the current (i.e., $\dot{V} = \dot{V}_0 \equiv 2\pi u_0 h_0 r_0; \bar{T} = T_0; \bar{R} = R_0$). Then, the particle mass conservation Eq. (F.6) may be reduced to

$$\begin{aligned} & \frac{\mathrm{d}}{\mathrm{d}r}(\bar{n}_\mathrm{s}\bar{\rho}) = -\bar{n}_\mathrm{s}\bar{\rho}\frac{2\pi W_\mathrm{s}}{\dot{V}_0}r \\ \therefore \quad & \frac{\mathrm{d}(\bar{n}_\mathrm{s}\bar{\rho})}{\bar{n}_\mathrm{s}\bar{\rho}} = -\frac{2\pi W_\mathrm{s}}{\dot{V}_0}r\ \mathrm{d}r. \end{aligned} \tag{F.14}$$

This is integrated from the collapsing column edge $r = r_0$ to yield

$$\begin{aligned} & \int_{n_{\mathrm{s}0}\rho_0}^{\bar{n}_\mathrm{s}\bar{\rho}} \frac{\mathrm{d}(\bar{n}'_\mathrm{s}\bar{\rho}')}{\bar{n}'_\mathrm{s}\bar{\rho}'} = -\int_{r_0}^{r} \frac{2\pi W_\mathrm{s}}{\dot{V}_0}r'\ \mathrm{d}r' \\ \therefore \quad & \ln\left[\frac{\bar{n}_\mathrm{s}\bar{\rho}}{n_{\mathrm{s}0}\rho_0}\right] = -\int_{r_0}^{r} \frac{2\pi W_\mathrm{s}}{\dot{V}_0}r'\ \mathrm{d}r'. \end{aligned} \tag{F.15}$$

Assuming that W_s remains approximately constant with distance from the collapsing col-

umn edge, Eq. (F.15) is reduced to

$$\ln\left[\frac{\bar{n}_{\rm s}\bar{\rho}}{n_{\rm s0}\rho_0}\right] = -\frac{\pi W_{\rm s}}{\dot{V}_0}(r^2 - r_0^2). \tag{F.16}$$

The bulk density $\bar{\rho}$ is expressed in

$$\begin{aligned}\bar{\rho} &= \left[\frac{\bar{n}_{\rm s}}{\rho_{\rm s}} + \frac{(1-\bar{n}_{\rm s})R_0T_0}{\bar{p}}\right]^{-1} \qquad (\because \text{ Eq. (F.5)}) \\ &\approx \frac{\bar{p}}{(1-\bar{n}_{\rm s})R_0T_0} \qquad (\because\ \bar{n}_{\rm s}/\rho_{\rm s} \ll (1-\bar{n}_{\rm s})R_0T_0/\bar{p}).\end{aligned} \tag{F.17}$$

Substituting Eq. (F.17) into Eq. (F.16), we obtain

$$\begin{aligned}&\ln\left[\frac{\bar{n}_{\rm s}/(1-\bar{n}_{\rm s})}{n_{\rm s0}/(1-n_{\rm s0})}\right] = -\frac{\pi W_{\rm s}}{\dot{V}_0}(r^2 - r_0^2) \\ \therefore\quad &\frac{\bar{n}_{\rm s}/(1-\bar{n}_{\rm s})}{n_{\rm s0}/(1-n_{\rm s0})} = \exp\left[-\frac{\pi W_{\rm s}}{\dot{V}_0}(r^2 - r_0^2)\right] \\ \therefore\quad &\frac{\bar{n}_{\rm s}}{1-\bar{n}_{\rm s}} = \frac{n_{\rm s0}}{1-n_{\rm s0}}\exp\left[-\frac{\pi W_{\rm s}}{\dot{V}_0}(r^2 - r_0^2)\right].\end{aligned} \tag{F.18}$$

Because $\bar{\rho} = \rho_{\rm a}$ at the steady runout distance r_∞, we may express the gas mass fraction at the steady runout distance in

$$1 - \bar{n}_{\rm s\infty} = \frac{R_{\rm a}T_{\rm a}}{R_0T_0} \qquad (\because\ \bar{p} = \rho_{\rm a}R_{\rm a}T_{\rm a}) \tag{F.19}$$

by using Eq. (F.17), whereas $1 - \bar{n}_{\rm s\infty} = T_{\rm a}/T_0$ is written in Bursik & Woods (1996) (see the next paragraph for the details). Substituting Eq. (F.19) into Eq. (F.18), we can obtain

the steady runout distance r_∞ as

$$
\begin{aligned}
& \frac{R_0 T_0}{R_\mathrm{a} T_\mathrm{a}} \left(1 - \frac{R_\mathrm{a} T_\mathrm{a}}{R_0 T_0} \right) = \frac{n_{\mathrm{s}0}}{1 - n_{\mathrm{s}0}} \exp \left[- \frac{\pi W_\mathrm{s}}{\dot{V}_0} (r_\infty^2 - r_0^2) \right] \\
\therefore \quad & \frac{R_0 T_0 - R_\mathrm{a} T_\mathrm{a}}{R_\mathrm{a} T_\mathrm{a}} = \frac{n_{\mathrm{s}0}}{1 - n_{\mathrm{s}0}} \exp \left[- \frac{\pi W_\mathrm{s}}{\dot{V}_0} (r_\infty^2 - r_0^2) \right] \\
\therefore \quad & \frac{(R_0 T_0 - R_\mathrm{a} T_\mathrm{a})(1 - n_{\mathrm{s}0})}{R_\mathrm{a} T_\mathrm{a} n_{\mathrm{s}0}} = \exp \left[- \frac{\pi W_\mathrm{s}}{\dot{V}_0} (r_\infty^2 - r_0^2) \right] \\
\therefore \quad & \ln \left[\frac{R_\mathrm{a} T_\mathrm{a} n_{\mathrm{s}0}}{(R_0 T_0 - R_\mathrm{a} T_\mathrm{a})(1 - n_{\mathrm{s}0})} \right] = \frac{\pi W_\mathrm{s}}{\dot{V}_0} (r_\infty^2 - r_0^2) \\
\therefore \quad & r_\infty = \sqrt{r_0^2 + \frac{\dot{V}_0}{\pi W_\mathrm{s}} \ln \left[\frac{R_\mathrm{a} T_\mathrm{a} n_{\mathrm{s}0}}{(R_0 T_0 - R_\mathrm{a} T_\mathrm{a})(1 - n_{\mathrm{s}0})} \right]} \\
\therefore \quad & r_\infty = \sqrt{r_0^2 + \frac{\dot{M}_0}{\pi \rho_0 W_\mathrm{s}} \ln \left[\frac{R_\mathrm{a} T_\mathrm{a} n_{\mathrm{s}0}}{(R_0 T_0 - R_\mathrm{a} T_\mathrm{a})(1 - n_{\mathrm{s}0})} \right]}. \qquad \text{(F.20)}
\end{aligned}
$$

In the text of Bursik & Woods (1996), the gas mass fraction at the steady runout distance

$$
1 - \bar{n}_{\mathrm{s}\infty} = \frac{T_\mathrm{a}}{T_0} \qquad \text{(F.21)}
$$

is used instead of Eq. (F.19). Accordingly, in the text of Bursik & Woods (1996), the steady runout distance r_∞ is expressed in

$$
\begin{aligned}
r_\infty &= \sqrt{r_0^2 + \frac{\dot{V}_0}{\pi W_\mathrm{s}} \ln \left[\frac{T_\mathrm{a} n_{\mathrm{s}0}}{(T_0 - T_\mathrm{a})(1 - n_{\mathrm{s}0})} \right]} \\
&= \sqrt{r_0^2 + \frac{\dot{M}_0}{\pi \rho_0 W_\mathrm{s}} \ln \left[\frac{T_\mathrm{a} n_{\mathrm{s}0}}{(T_0 - T_\mathrm{a})(1 - n_{\mathrm{s}0})} \right]}. \qquad \text{(F.22)}
\end{aligned}
$$

Next, we reproduce Figure 3b in Bursik & Woods (1996) (see the black curves in Figure F.2d) by using Eq. (F.20) or Eq. (F.22). This figure shows the steady runout distances as a function of mass fraction of gas at the collapsing column edge ($1 - n_{\mathrm{s}0}$). Bursik & Woods (1996) are thought to use the correct Eq. (F.20) or the incorrect Eq. (F.22) to describe Figure 3b in Bursik & Woods (1996) (i.e., the black curves in Figure

F.2d). Furthermore, in this figure, the boundary temperature at the collapsing column edge, T_0, may be erroneously calculated due to inverting the value of the specific heat at constant pressure of air $C_{\rm pa}$ and that of volcanic gas $C_{\rm pg}$ (see Subsection F.2.1 for the details). Thus, we show the results of the following three cases: (1) the correct Eq. (F.20) is used and the values of $C_{\rm pa}$ and $C_{\rm pg}$ are correctly given (Figure F.2a); (2) the correct Eq. (F.20) is used and the values of $C_{\rm pa}$ and $C_{\rm pg}$ are inverted (Figure F.2b); (3) the incorrect Eq. (F.22) is used and the values of $C_{\rm pa}$ and $C_{\rm pg}$ are inverted (Figure F.2c). Then, we compare these results with Figure 3b of Bursik & Woods (1996) (Figures F.2d and e).

Figure F.2d and e shows that Figure 3b of Bursik & Woods (1996) agrees much better with the results of case (2) than with the results of case (3). This means that, although the incorrect Eq. (F.22) is written in the text of Bursik & Woods (1996), the correct Eq. (F.20) may be used in Figure 3b of Bursik & Woods (1996). And, Figure F.2a and d shows that Figure 3b of Bursik & Woods (1996) agrees much better with the results of case (2) than with the results of case (1). This means that the boundary temperature at the collapsing column edge, T_0, may be erroneously calculated due to inverting the value of the specific heat at constant pressure of air $C_{\rm pa}$ and that of volcanic gas $C_{\rm pg}$ in Figure 3b of Bursik & Woods (1996).

One-dimensional channelized currents

We derive the analytical solution of the steady runout distance of the one-dimensional channelized dilute PDCs without air entrainment. Assuming that the rate of entrainment of ambient air is negligible, the volume flux of the current $\dot{V}(\equiv \bar{u}hy_0)$, the temperature of the current $\bar{T}$ and the gas constant of the current $\bar{R}$ remain approximately constant along the length of the current (i.e., $\dot{V} = \dot{V}_0 \equiv u_0 h_0 y_0; \bar{T} = T_0; \bar{R} = R_0$). Here, y_0 is the

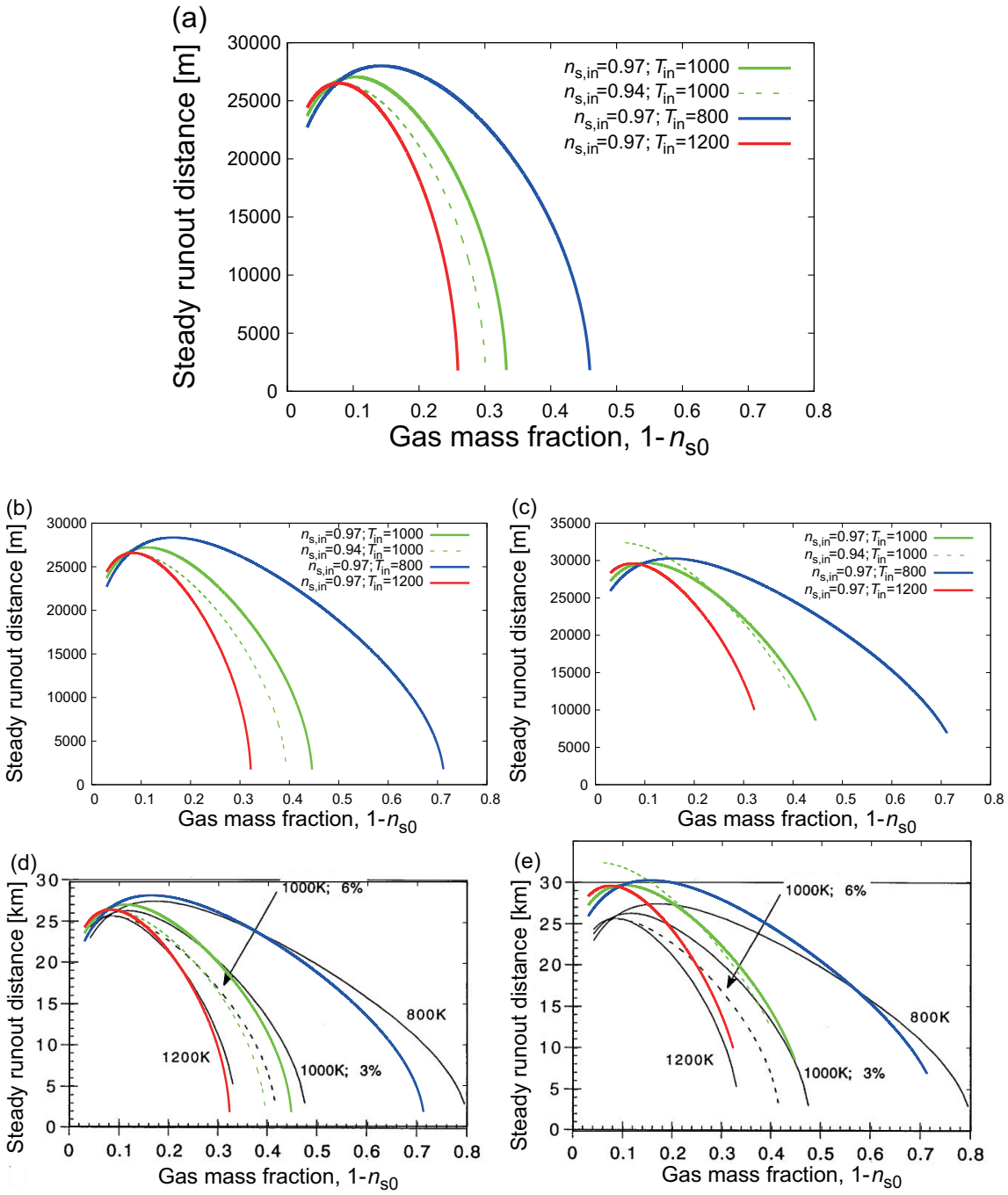

Figure F.2: Steady runout distances as a function of the gas mass fraction in the current at the collapsing column edge $(1 - n_{s0})$. The mass eruption rate at the collapsing column edge $\rho_0 u_0 h_0 r_0 = 10^9$ kg/s; particle settling velocity $W_s = 1$ m/s; the distance of the collapsing column edge $r_0 = 1$ km; the temperature of the erupted material $T_{in} = 800$ K (blue), 1000 K (green), 1200 K (red); the solid particle mass fraction in the erupted material $n_{s,in} = 0.97$ (solid curves), 0.94 (dashed curve). (a) the correct Eq. (F.20) is used and the values of C_{pa} and C_{pg} are correctly given (see Table **??**); (b) the correct Eq. (F.20) is used and the values of C_{pa} and C_{pg} are inverted; (c) the incorrect Eq. (F.22) is used and the values of C_{pa} and C_{pg} are inverted; (d) (b) is superposed on Figure 3b in Bursik & Woods (1996); (e) (c) is superposed on Figure 3b in Bursik & Woods (1996).

channel width. Then, the particle mass conservation Eq. (F.1) may be reduced to

$$\begin{aligned} & \frac{\mathrm{d}}{\mathrm{d}x}(\bar{n}_{\mathrm{s}}\bar{\rho}) = -\bar{n}_{\mathrm{s}}\bar{\rho}\frac{W_{\mathrm{s}}}{\dot{V}_0}y_0 \\ \therefore \quad & \frac{\mathrm{d}(\bar{n}_{\mathrm{s}}\bar{\rho})}{\bar{n}_{\mathrm{s}}\bar{\rho}} = -\frac{W_{\mathrm{s}}}{\dot{V}_0}y_0\ \mathrm{d}x. \end{aligned} \tag{F.23}$$

This is integrated from the collapsing column edge $x = x_0$ to yield

$$\begin{aligned} & \int_{n_{\mathrm{s}0}\rho_0}^{\bar{n}_{\mathrm{s}}\bar{\rho}} \frac{\mathrm{d}(\bar{n}'_{\mathrm{s}}\bar{\rho}')}{\bar{n}'_{\mathrm{s}}\bar{\rho}'} = -\int_{x_0}^{x} \frac{W_{\mathrm{s}}}{\dot{V}_0}y_0\ \mathrm{d}x' \\ \therefore \quad & \ln\left[\frac{\bar{n}_{\mathrm{s}}\bar{\rho}}{n_{\mathrm{s}0}\rho_0}\right] = -\int_{x_0}^{x} \frac{W_{\mathrm{s}}}{\dot{V}_0}y_0\ \mathrm{d}x'. \end{aligned} \tag{F.24}$$

Assuming that W_{s} remains approximately constant with distance from the collapsing column edge, Eq. (F.24) is reduced to

$$\ln\left[\frac{\bar{n}_{\mathrm{s}}\bar{\rho}}{n_{\mathrm{s}0}\rho_0}\right] = -\frac{W_{\mathrm{s}}}{\dot{V}_0}y_0(x - x_0). \tag{F.25}$$

The bulk density $\bar{\rho}$ is expressed in

$$\begin{aligned} \bar{\rho} &= \left[\frac{\bar{n}_{\mathrm{s}}}{\rho_{\mathrm{s}}} + \frac{(1-\bar{n}_{\mathrm{s}})R_0T_0}{\bar{p}}\right]^{-1} \qquad (\because \text{ Eq. (F.5)}) \\ &\approx \frac{\bar{p}}{(1-\bar{n}_{\mathrm{s}})R_0T_0} \qquad (\because\ \bar{n}_{\mathrm{s}}/\rho_{\mathrm{s}} \ll (1-\bar{n}_{\mathrm{s}})R_0T_0/\bar{p}). \end{aligned} \tag{F.26}$$

Substituting Eq. (F.26) into Eq. (F.25), we obtain

$$\begin{aligned} & \ln\left[\frac{\bar{n}_{\mathrm{s}}/(1-\bar{n}_{\mathrm{s}})}{n_{\mathrm{s}0}/(1-n_{\mathrm{s}0})}\right] = -\frac{W_{\mathrm{s}}}{\dot{V}_0}y_0(x - x_0) \\ \therefore \quad & \frac{\bar{n}_{\mathrm{s}}/(1-\bar{n}_{\mathrm{s}})}{n_{\mathrm{s}0}/(1-n_{\mathrm{s}0})} = \exp\left[-\frac{W_{\mathrm{s}}}{\dot{V}_0}y_0(x - x_0)\right] \\ \therefore \quad & \frac{\bar{n}_{\mathrm{s}}}{1-\bar{n}_{\mathrm{s}}} = \frac{n_{\mathrm{s}0}}{1-n_{\mathrm{s}0}}\exp\left[-\frac{W_{\mathrm{s}}}{\dot{V}_0}y_0(x - x_0)\right]. \end{aligned} \tag{F.27}$$

Because $\bar{\rho} = \rho_{\mathrm{a}}$ at the steady runout distance x_∞, we may express the gas mass fraction at the steady runout distance in

$$1 - \bar{n}_{\mathrm{s}\infty} = \frac{R_{\mathrm{a}} T_{\mathrm{a}}}{R_0 T_0} \qquad (\because\ \bar{p} = \rho_{\mathrm{a}} R_{\mathrm{a}} T_{\mathrm{a}}) \tag{F.28}$$

by using Eq. (F.26), whereas $1 - \bar{n}_{\mathrm{s}\infty} = T_{\mathrm{a}}/T_0$ is used in the text of Bursik & Woods (1996) (see the next paragraph for the details). Substituting Eq. (F.28) into Eq. (F.27), we can obtain the steady runout distance x_∞ as

$$\begin{aligned}
& \frac{R_0 T_0}{R_{\mathrm{a}} T_{\mathrm{a}}} \left(1 - \frac{R_{\mathrm{a}} T_{\mathrm{a}}}{R_0 T_0} \right) = \frac{n_{\mathrm{s}0}}{1 - n_{\mathrm{s}0}} \exp \left[-\frac{W_{\mathrm{s}}}{\dot{V}_0} y_0 (x_\infty - x_0) \right] \\
\therefore \quad & \frac{R_0 T_0 - R_{\mathrm{a}} T_{\mathrm{a}}}{R_{\mathrm{a}} T_{\mathrm{a}}} = \frac{n_{\mathrm{s}0}}{1 - n_{\mathrm{s}0}} \exp \left[-\frac{W_{\mathrm{s}}}{\dot{V}_0} y_0 (x_\infty - x_0) \right] \\
\therefore \quad & \frac{(R_0 T_0 - R_{\mathrm{a}} T_{\mathrm{a}})(1 - n_{\mathrm{s}0})}{R_{\mathrm{a}} T_{\mathrm{a}} n_{\mathrm{s}0}} = \exp \left[-\frac{W_{\mathrm{s}}}{\dot{V}_0} y_0 (x_\infty - x_0) \right] \\
\therefore \quad & \ln \left[\frac{R_{\mathrm{a}} T_{\mathrm{a}} n_{\mathrm{s}0}}{(R_0 T_0 - R_{\mathrm{a}} T_{\mathrm{a}})(1 - n_{\mathrm{s}0})} \right] = \frac{W_{\mathrm{s}}}{\dot{V}_0} y_0 (x_\infty - x_0) \\
\therefore \quad & x_\infty = x_0 + \frac{\dot{V}_0}{y_0 W_{\mathrm{s}}} \ln \left[\frac{R_{\mathrm{a}} T_{\mathrm{a}} n_{\mathrm{s}0}}{(R_0 T_0 - R_{\mathrm{a}} T_{\mathrm{a}})(1 - n_{\mathrm{s}0})} \right] \\
\therefore \quad & x_\infty = x_0 + \frac{\dot{M}_0}{\rho_0 y_0 W_{\mathrm{s}}} \ln \left[\frac{R_{\mathrm{a}} T_{\mathrm{a}} n_{\mathrm{s}0}}{(R_0 T_0 - R_{\mathrm{a}} T_{\mathrm{a}})(1 - n_{\mathrm{s}0})} \right].
\end{aligned} \tag{F.29}$$

In the text of Bursik & Woods (1996), the gas mass fraction at the steady runout distance

$$1 - \bar{n}_{\mathrm{s}\infty} = \frac{T_{\mathrm{a}}}{T_0} \tag{F.30}$$

is used instead of Eq. (F.28). Accordingly, in the text of Bursik & Woods (1996), the steady runout distance x_∞ is expressed in

$$\begin{aligned}
x_\infty &= x_0 + \frac{\dot{V}_0}{y_0 W_{\mathrm{s}}} \ln \left[\frac{T_{\mathrm{a}} n_{\mathrm{s}0}}{(T_0 - T_{\mathrm{a}})(1 - n_{\mathrm{s}0})} \right] \\
&= x_0 + \frac{\dot{M}_0}{\rho_0 y_0 W_{\mathrm{s}}} \ln \left[\frac{T_{\mathrm{a}} n_{\mathrm{s}0}}{(T_0 - T_{\mathrm{a}})(1 - n_{\mathrm{s}0})} \right].
\end{aligned} \tag{F.31}$$

Acknowledgements

In the first place, I would like to thank Prof. Takehiro KOYAGUCHI for his valuable supports and thoughtful and helpful suggestions during this study. I also would like to thank Assistant Prof. Yujiro SUZUKI for his thoughtful and helpful suggestions.

I acknowledge members and former members of our laboratory, Dr. Atsushi NAKAO, Dr. Koji KIYOSUGI, Mr. Satoshi INAGAWA, Mr. Naoya MATSUO, Mr. Yuto INAGAKI, Mr. Kai TAKEDA, and Mr. Kentaro KOYAMA, for their encouragement, help, and useful comments. I also like to thank Prof. Hiroaki KOMURO for leading me to the world of pyroclastic density current.

The constructive reviews by Associate Prof. Fukashi MAENO, Associate Prof. Takahiro HATANO, Prof. Toshiyuki HIBIYA, and Prof. Setsuya NAKADA have improved this manuscript and are acknowledged.

Finally, I would like to thank my friends for their much encouragement. I express my sincere gratitude to my families for their supports.

References

[1] Allen, J. R. L. (1984). *Sedimentary structures: their character and physical basis*. *Developments in Sedimentology* 30. Elsevier, Amsterdam.

[2] Allen, S. R., & Cas, R. A. F. (1998). Rhyolitic fallout and pyroclastic density current deposits from a phreatoplinian eruption in the eastern Aegean Sea, Greece. *J. Volcanol. Geotherm. Res.*, **86**(1), 219–251.

[3] Andrews, B. J. (2014). Dispersal and air entrainment in unconfined dilute pyroclastic density currents. *Bull. Volcanol.*, **76**(9), 1–14.

[4] Andrews, B. J., & Manga, M. (2011). Effects of topography on pyroclastic density current runout and formation of coignimbrites. *Geology*, **39**(12), 1099–1102.

[5] Andrews, B. J., & Manga, M. (2012). Experimental study of turbulence, sedimentation, and coignimbrite mass partitioning in dilute pyroclastic density currents. *J. Volcanol. Geotherm. Res.*, **225**, 30–44.

[6] Bardot, L., & McClelland, E. (2000). The reliability of emplacement temperature estimates using palaeomagnetic methods: A case study from Santorini, Greece. *Geophys. J. Int.*, **143**(1), 39–51.

[7] Benjamin, T. B. (1968). Gravity currents and related phenomena. *J. Fluid Mech.*, **31**(02), 209–248.

[8] Bonnecaze, R. T., Huppert, H. E., & Lister, J. R. (1993). Particle-driven gravity currents. *J. Fluid Mech*, **250**, 339–369.

[9] Branney, M. J., & Kokelaar, B. P. (1997). Giant bed from a sustained catastrophic density current flowing over topography: Acatlan ignimbrite, Mexico. *Geology*, **25**(2), 115–118.

[10] Branney, M. J., & Kokelaar, B. P. (2002). *Pyroclastic density currents and the sedimentation of ignimbrites*. Memoirs 27. Geological Society, London.

[11] Branney, M. J., & Kokelaar, B. P. (1992). A reappraisal of ignimbrite emplacement: Progressive aggradation and changes from particulate to non-particulate flow during emplacement of high-grade ignimbrite. *Bull. Volcanol.*, **54**(6), 504–520.

[12] Breard, E. C. P., & Lube, G. (2017). Inside pyroclastic density currents uncovering the enigmatic flow structure and transport behaviour in large-scale experiments. *Earth Planet. Sci. Lett.*, **458**, 22–36.

[13] Breard, E. C. P., Lube, G., Jones, J. R., Dufek, J., Cronin, S. J., Valentine, G. A., & Moebis, A. (2016). Coupling of turbulent and non-turbulent flow regimes within pyroclastic density currents. *Nat. Geosci.*, **9**(10), 767–771.

[14] Brown, R. J., & Andrews, G. D. (2015). Deposits of Pyroclastic Density Currents. In: Sigurdsson, H. (Ed.), *The Encyclopedia of Volcanoes* (Second edition), Academic Press, Amsterdam, pp. 631–648.

[15] Brown, R. J., & Branney, M. J. (2004). Event-stratigraphy of a caldera-forming ignimbrite eruption on Tenerife: The 273 ka Poris Formation. *Bull. Volcanol.*, **66**(5), 392–416.

[16] Brown, R. J., & Branney, M. J. (2013). Internal flow variations and diachronous sedimentation within extensive, sustained, density-stratified pyroclastic density currents flowing down gentle slopes, as revealed by the internal architectures of ignimbrites on Tenerife. *Bull. Volcanol.*, **75**(7), 727.

[17] Burgisser, A., & Bergantz, G. W. (2002). Reconciling pyroclastic flow and surge: The multiphase physics of pyroclastic density currents. *Earth Planet. Sci. Lett.*, **202**(2), 405–418.

[18] Bursik, M. I., & Woods, A. W. (1991). Buoyant, superbuoyant and collapsing eruption columns. *J. Volcanol. Geotherm. Res.*, **45**(3), 347–350.

[19] Bursik, M. I., & Woods, A. W. (1996). The dynamics and thermodynamics of large ash flows. *Bull. Volcanol.*, **58**(2–3), 175–193.

[20] Calder, E. S., Sparks, R. S. J., & Woods, A. W. (1997). Dynamics of co-ignimbrite plumes generated from pyroclastic flows of Mount St. Helens (7 August 1980). *Bull. Volcanol.*, **58**(6), 432–440.

[21] Cao, Z., Pender, G., Wallis, S., & Carling, P. (2004). Computational dam-break hydraulics over erodible sediment bed. *J. Hydraul Res.*, **130**(7), 689–703.

[22] Carey, S. N., Sigurdsson, H., Gardner, J., & Criswell, W. (1990). Variations in column height and magma discharge during the May 18, 1980 eruption of Mount St. Helens. *J. Volcanol. Geotherm. Res.*, **43**(1–4), 99–112.

[23] Cas, R. A. F., Wright, H. M. N., Folkes, C. B., Lesti, C., Porreca, M., Giordano, G., & Viramonte, J. G. (2011). The flow dynamics of an extremely large volume pyroclastic flow, the 2.08-Ma Cerro Galán ignimbrite, NW Argentina, and comparison with other flow types. *Bull. Volcanol.*, **73**(10), 1583–1609.

[24] Cas, R. A. F., & Wright, J. V. (1987). *Volcanic successions: modern and ancient*, Chapman & Hall, London.

[25] Cheong, C., Choi, J., Sohn, Y., Kim, J., & Jeong, G. (2007). Optical dating of hydromagmatic volcanoes on the southwestern coast of Jeju Island, Korea. *Quat. Geochronol.*, **2**(1–4), 266–271.

[26] Costa, A., Smith, V. C., Macedonio, G., & Matthews, N. E. (2014). The magnitude and impact of the Youngest Toba Tuff super-eruption. *Front. Earth Sci.*, **2**, 16.

[27] Dade, W. B. (2003). The emplacement of low-aspect ratio ignimbrites by turbulent parent flows. *J. Geophys. Res.*, **108**, 2211.

[28] Dade, W. B., & Huppert, H. E. (1996). Emplacement of the Taupo ignimbrite by a dilute turbulent flow. *Nature*, **381**(6582), 509–512.

[29] De Rita, D., Giordano, G., Esposito, A., Fabbri, M., & Rodani, S. (2002). Large volume phreatomagmatic ignimbrites from the Colli Albani volcano (Middle Pleistocene, Italy). *J. Volcanol. Geotherm. Res.*, **118**(1), 77–98.

[30] Dellino, P., Mele, D., Bonasia, R., Braia, G., La Volpe, L., & Sulpizio, R. (2005). The analysis of the influence of pumice shape on its terminal velocity. *Geophys. Res. Lett.*, **32**, L21306.

[31] Denlinger, R. P., & Iverson, R. M. (2004). Granular avalanches across irregular three-dimensional terrain: 1. Theory and computation. *J. Geophys. Res.*, **109**, F01014.

[32] Doyle, E. E., Hogg, A. J., Mader, H. M., & Sparks, R. S. J. (2008). Modeling dense pyroclastic basal flows from collapsing columns. *Geophys. Res. Lett.*, **35**, L04305.

[33] Doyle, E. E., Hogg, A. J., Mader, H. M., & Sparks, R. S. J. (2010). A two-layer model for the evolution and propagation of dense and dilute regions of pyroclastic currents. *J. Volcanol. Geotherm. Res.*, **190**(3), 365–378.

[34] Doyle, E. E., Hogg, A. J., & Mader, H. M. (2011). A two-layer approach to modelling the transformation of dilute pyroclastic currents into dense pyroclastic flows. *Proc. R. Soc. A.*, **467**(2129) 1348–1371.

[35] Doyle, E. E., Huppert, H. E., Lube, G., Mader, H. M., & Sparks, R. S. J. (2007). Static and flowing regions in granular collapses down channels: Insights from a sedimenting shallow water model. *Phys. Fluids*, **19**(10), 106601–106616.

[36] Druitt, T. H. (1996). Turbulent times at Taupo. *Nature*, **381**, 476–477.

[37] Druitt, T. H. (1998). Pyroclastic density currents. In: Gilbert, J. S., & Sparks, R. S. J. (Eds.), *The Physics of Explosive Volcanic Eruptions*. Geol. Soc. London Spec. Pub., pp.145–182.

[38] Druitt, T. H., Avard, G., Bruni, G., Lettieri, P., & Maez, F. (2007). Gas retention in fine-grained pyroclastic flow materials at high temperatures. *Bull. Volcanol.*, **69**(8), 881–901.

[39] Druitt, T. H., Calder, E. S., Cole, P. D., Hoblitt, R. P., Loughlin, S. C., Norton, G. E., Ritchie, L. J., Sparks, R. S. J., & Voight, B. (2002). Small-volume, highly mobile pyroclastic flows formed by rapid sedimentation from pyroclastic surges at Soufrière Hills Volcano, Montserrat: An important volcanic hazard. In: Druitt, T. H., & Kokelaar, B. P. (Eds.), *The Eruption of Soufrière Hills Volcano, Montserrat, From 1995 to 1999*, Mem. Geol. Soc. London, **21**, 263–280.

[40] Druitt, T. H., & Sparks, R. S. J. (1982). A proximal ignimbrite breccia facies on Santorini, Greece. *J. Volcanol. Geotherm. Res.*, **13**(1–2), 147–171.

[41] Dufek, J. (2016). The fluid mechanics of pyroclastic density currents. *Ann. Rev. Fluid Mech.*, **48**, 459–485.

[42] Dufek, J., Esposti Ongaro, T., & Roche, O. (2015). Pyroclastic density currents: Processes and models. In: Sigurdsson, H. (Ed.), *The Encyclopedia of Volcanoes* (Second edition), Academic Press, Amsterdam, pp. 617–629.

[43] Ellison, T., & Turner, J. (1959). Turbulent entrainment in stratified flows. *J. Fluid Mech.*, **6**(3), 423–448.

[44] Fierstein, J., & Nathenson, M. (1992). Another look at the calculation of fallout tephra volumes. *Bull. Volcanol.*, **54**(2), 156–167.

[45] Fisher, R. V. (1966). Mechanism of deposition from pyroclastic flows. *Am. J. Sci.*, **264**(5), 350–363.

[46] Fisher, R. V. (1979). Models for pyroclastic surges and pyroclastic flows. *J. Volcanol. Geotherm. Res.*, **6**(3–4), 305–318.

[47] Fisher, R. V., Orsi, G., Ort, M., & Heiken, G. (1993). Mobility of a large-volume pyroclastic flow-emplacement of the campanian ignimbrite, italy. *J. Volcanol. Geotherm. Res.*, **56**(3), 205–220.

[48] Fisher, R. V. (1980). Ignimbrite veneer deposits or pyroclastic surge deposits? *Nature*, **286**, 912.

[49] Fisher, R. V., & Schmincke, H. (1984). *Pyroclastic rocks*, 472 pp. Springer, Berlin.

[50] Freundt, A., & Schmincke, H. (1985). Lithic-enriched segregation bodies in pyroclastic flow deposits of Laacher See Volcano (East Eifel, Germany). *J. Volcanol. Geotherm. Res.*, **25**(3), 193–224.

[51] Fujii, T., & Nakada, S. (1999). The 15 September 1991 pyroclastic flows at Unzen Volcano (Japan): A flow model for associated ash-cloud surges. *J. Volcanol. Geotherm. Res.*, **89**(1), 159–172.

[52] Giordano, G., & Doronzo, D. M. (2017). Sedimentation and mobility of PDCs: A reappraisal of ignimbrites' aspect ratio. *Sci. Rep.*, **7**(4444), 1–7.

[53] Girolami, L., Druitt, T. H., & Roche, O. (2015). Towards a quantitative understanding of pyroclastic flows: Effects of expansion on the dynamics of laboratory fluidized granular flows. *J. Volcanol. Geotherm. Res.*, **296**, 31–39.

[54] Girolami, L., Druitt, T. H., Roche, O., & Khrabrykh, Z. (2008). Propagation and hindered settling of laboratory ash flows. *J. Geophys. Res.*, **113**, B02202.

[55] Girolami, L., Roche, O., Druitt, T. H., & Corpetti, T. (2010). Particle velocity fields and depositional processes in laboratory ash flows, with implications for the sedimentation of dense pyroclastic flows. *Bull. Volcanol.*, **72**(6), 747–759.

[56] Gray, J. M. N. T., & Kokelaar, B. P. (2010). Large particle segregation, transport and accumulation in granular free-surface flows. *J. Fluid Mech.*, **652**, 105–137.

[57] Griggs, R. F. (1922). *The valley of ten thousand smokes National geographic society*. National Geographic Society, Washington DC.

[58] Gueugneau, V., Kelfoun, K., Roche, O., & Chupin, L. (2017). Effects of pore pressure in pyroclastic flows: Numerical simulation and experimental validation. *Geophys. Res. Lett.*, **44**(5), 2194–2202.

[59] Hager, W. (1988). Abflussformeln für turbulente strömungen. *Wasserwirtschaft* **78**, 79–84.

[60] Heiken, G., & McCoy, F. (1984). Caldera development during the Minoan eruption, Thira, Cyclades, Greece. *J. Geophys. Res.*, **89**(B10), 8441–8462.

[61] Hildreth, W. (1983). The compositionally zoned eruption of 1912 in the Valley of Ten Thousand Smokes, Katmai National Park, Alaska. *J. Volcanol. Geotherm. Res.*, **18**(1–4), 1–56.

[62] Hildreth, W., & Fierstein, J. (2012). The Novarupta-Katmai Eruption of 1912—Largest Eruption of the Twentieth Century: Centennial Perspectives. *USGS Prof. Paper*, **1791**, pp. 259.

[63] Hoblitt, R. P. (1986). Observations of the eruptions of July 22 and August 7 1980 at Mount St. Helens, Washington. *USGS Prof. Paper*, **1335**, 1–44.

[64] Hogg, A. J. (2006). Lock-release gravity currents and dam-break flows. *J. Fluid Mech.*, **569**, 61–87.

[65] Hogg, A. J., & Pritchard, D. (2004). The effects of hydraulic resistance on dam-break and other shallow inertial flows. *J. Fluid Mech.*, **501**, 179–212.

[66] Huppert, H. E., & Simpson, J. E. (1980). The slumping of gravity currents. *J. Fluid Mech.*, **99**(04), 785–799.

[67] Huppert, H. E., Turner, J. S., Carey, S. N., Stephen, R., Sparks, R. S. J., & Hallworth, M. A. (1986). A laboratory simulation of pyroclastic flows down slopes. *J. Volcanol. Geotherm. Res.*, **30**(3-4), 179–199.

[68] Ishimine, Y. (2005). Numerical study of pyroclastic surges. *J. Volcanol. Geotherm. Res.*, **139**(1), 33–57.

[69] Iverson, R. M. (1997). The physics of debris flows. *Rev. Geophys.*, **35**(3), 245–296.

[70] Johnson, C. G., & Hogg, A. J. (2013). Entraining gravity currents. *J. Fluid Mech.*, **731**, 477–508.

[71] Kelfoun, K., & Druitt, T. H. (2005). Numerical modeling of the emplacement of Socompa rock avalanche, Chile. *J. Geophys. Res.*, **110**, B12202.

[72] Kelfoun, K. (2011). Suitability of simple rheological laws for the numerical simulation of dense pyroclastic flows and long-runout volcanic avalanches. *J. Geophys. Res.*, **116**, B08209.

[73] Kelfoun, K. (2017). A two-layer depth-averaged model for both the dilute and the concentrated parts of pyroclastic currents. *J. Geophys. Res.*, **122**, doi:10.1002/2017JB014013.

[74] Kelfoun, K., Gueugneau, V., Komorowski, J., Aisyah, N., Cholik, N., & Merciecca, C. (2017). Simulation of block-and-ash flows and ash-cloud surges of the

2010 eruption of Merapi volcano with a two-layer model. *J. Geophys. Res.*, **122**, doi:10.1002/2017JB013981.

[75] Kelfoun, K., Samaniego, P., Palacios, P., & Barba, D. (2009). Testing the suitability of frictional behaviour for pyroclastic flow simulation by comparison with a well-constrained eruption at Tungurahua volcano (Ecuador). *Bull. Volcanol.*, **71**(9), 1057–1075.

[76] Koyaguchi, T., & Ohno, M. (2001). Reconstruction of eruption column dynamics on the basis of grain size of tephra fall deposits: 1. Methods. *J. Geophys. Res.*, **106**(B4), 6499–6512.

[77] Koyaguchi, T., & Ohno, M. (2001). Reconstruction of eruption column dynamics on the basis of grain size of tephra fall deposits: 2. Application to the Pinatubo 1991 eruption. *J. Geophys. Res.*, **106**(B4), 6513–6533.

[78] Koyaguchi, T., & Woods, A. W. (1996). On the formation of eruption columns following explosive mixing of magma and surface-water. *J. Geophys. Res.*, **101**(B3), 5561–5574.

[79] Larrieu, E., Staron, L., & Hinch, E. (2006). Raining into shallow water as a description of the collapse of a column of grains. *J. Fluid Mech.*, **554**, 259–270.

[80] Lesti, C., Porreca, M., Giordano, G., Mattei, M., Cas, R. A. F., Wright, H. M. N., Folkes, C. B., Viramonte, J. (2011). High-temperature emplacement of the Cerro Galán and Toconquis Group ignimbrites (Puna plateau, NW Argentina) determined by TRM analyses. *Bull. Volcanol.*, **73**(10), 1535–1565.

[81] LeVeque, R. J. (2002). *Finite volume methods for hyperbolic problems*. Cambridge University Press.

[82] Li, J., Cao, Z., Hu, K., Pender, G., & Liu, Q. (2017). A depth-averaged two-phase model for debris flows over erodible beds. *Earth Surf. Process. Landforms*, doi: 10.1002/esp.4283.

[83] Lindsay, J., De Silva, S., Trumbull, R., Emmermann, R., & Wemmer, K. (2001). La Pacana caldera, N. Chile: A re-evaluation of the stratigraphy and volcanology of one of the world's largest resurgent calderas. *J. Volcanol. Geotherm. Res.*, **106**(1), 145–173.

[84] Lube, G., Cronin, S. J., Platz, T., Freundt, A., Procter, J. N., Henderson, C., & Sheridan, M. F. (2007). Flow and deposition of pyroclastic granular flows: A type example from the 1975 Ngauruhoe eruption, New Zealand. *J. Volcanol. Geotherm. Res.*, **161**(3), 165–186.

[85] Machida, H., & Arai, F. (1976). A wide spread volcanic ash — discovery of Aira-Tn ash and its significance. *Kagaku*, **46**, 339–347.

[86] Machida, H., & Arai, F. (1978). Akahoya ash — a Holocene widespread tephra erupted from the Kikai caldera, South Kyushu, Japan. *Quat. Res.*, **17**, 143–163.

[87] Marino, B., Thomas, L., & Linden, P. (2005). The front condition for gravity currents. *J. Fluid Mech.*, **536**, 49–78.

[88] McClelland, E. A., & Druitt, T. H. (1989). Palaeomagnetic estimates of emplacement temperatures of pyroclastic deposits on Santorini, Greece. *Bull. Volcanol.*, **51**(1), 16–27.

[89] Miller, T. P., & Smith, R. L. (1977). Spectacular mobility of ash flows around Aniakchak and Fisher calderas, Alaska. *Geology*, **5**(3), 173–176.

[90] Mitani, N. K., Matuttis, H.-G., & Kadono, T. (2004). Density and size segregation in deposits of pyroclastic flow. *Geophys. Res. Lett.*, **31**(15), L15606.

[91] Orsi, G., D'Antonio, M., de Vita, S., & Gallo, G. (1992). The Neapolitan Yellow Tuff, a large-magnitude trachytic phreatoplinian eruption: Eruptive dynamics, magma withdrawal and caldera collapse. *J. Volcanol. Geotherm. Res.*, **53**(1), 275–287.

[92] Parker, G., Garcia, M., Fukushima, Y., & Yu, W. (1987). Experiments on turbidity currents over an erodible bed. *J. Hydraul Res.*, **25**(1), 123–147.

[93] Patra, A. K., Bauer, A., Nichita, C., Pitman, E. B., Sheridan, M., Bursik, M. I., Rupp, B., Webber, A., Stinton, A., Namikawa, L. (2005). Parallel adaptive numerical simulation of dry avalanches over natural terrain. *J. Volcanol. Geotherm. Res.*, **139**(1), 1–21.

[94] Richardson, J., & Zaki, W. (1954). Fluidization and sedimentation: Part I. *Trans. Inst. Chem. Eng.*, **32**, 38–58.

[95] Roche, O. (2012). Depositional processes and gas pore pressure in pyroclastic flows: An experimental perspective. *Bull. Volcanol.*, **74**(8), 1807–1820.

[96] Roche, O., Buesch, D. C., & Valentine, G. A. (2016). Slow-moving and far-travelled dense pyroclastic flows during the Peach Spring super-eruption. *Nat. Comm.*, **7**, 10890.

[97] Roche, O., Montserrat, S., Niño, Y., & Tamburrino, A. (2008). Experimental observations of water-like behavior of initially fluidized, dam break granular flows and their relevance for the propagation of ash-rich pyroclastic flows. *J. Geophys. Res.*, **113**, B12203.

[98] Roche, O., Montserrat, S., Niño, Y., & Tamburrino, A. (2010). Pore fluid pressure and internal kinematics of gravitational laboratory air-particle flows: Insights into the emplacement dynamics of pyroclastic flows. *J. Geophys. Res.*, **115**, B09206.

[99] Roche, O., Niño, Y., Mangeney, A., Brand, B., Pollock, N., & Valentine, G. (2013). Dynamic pore-pressure variations induce substrate erosion by pyroclastic flows. *Geology*, **41**(10), 1107–1110.

[100] Roche, O., Phillips, J., & Kelfoun, K. (2013). *Pyroclastic density currents*. In: Fagents, S. A., Gregg, T. K. P., Lopes, R. M. C. (Eds.), *Modeling Volcanic Processes: The Physics and Mathematics of Volcanism*, Cambridge University Press, pp. 203–229.

[101] Rottman, J. W., & Simpson, J. E. (1983). Gravity currents produced by instantaneous releases of a heavy fluid in a rectangular channel. *J. Fluid Mech.*, **135**, 95–110.

[102] Rowley, P. (1981). Pyroclastic-flow deposits. The 1980 eruptions of Mount St. Helens, Washington. *USGS Prof. Paper*, **1250**, 489–512.

[103] Schumacher, R., & Mues-Schumacher, U. (1997). The pre-ignimbrite (phreato) plinian and phreatomagmatic phases of the Akdag-Zelve ignimbrite eruption in Central Anatolia, Turkey. *J. Volcanol. Geotherm. Res.*, **78**(1–2), 139–153.

[104] Shimizu, H. A., Koyaguchi, T., & Suzuki, Y. J. (2017). A numerical shallow-water model for gravity currents for a wide range of density differences. *Prog. Earth Planet. Sci.*, **4**(1), 8.

[105] Sigurdsson, H., & Carey, S. N. (1989). Plinian and co-ignimbrite tephra fall from the. *Bull. Volcanol.*, **51**(4), 243–270.

[106] Smith, R. L. (1960). Ash flows. *Geol. Soc. Amer. Bull.*, **71**(6), 795–841.

[107] Sohn, Y. K., & Chough, S. K. (1989). Depositional processes of the Suwolbong tuff ring, Cheju Island (Korea). *Sedimentology*, **36**(5), 837–855.

[108] Sparks, R. S. J. (1976). Grain size variations in ignimbrites and implications for the transport of pyroclastic flows. *Sedimentology*, **23**(2), 147–188.

[109] Sparks, R. S. J., Bonnecaze, R. T., Huppert, H. E., Lister, J. R., Hallworth, M. A., Mader, H., & Phillips, J. (1993). Sediment-laden gravity currents with reversing buoyancy. *Earth Planet. Sci. Lett.*, **114**(2–3), 243–257.

[110] Sparks, R. S. J., Bursik, M. I., Carey, S. N., Gilbert, J., Glaze, L. S., Sigurdsson, H., & Woods, A. W. (1997). *Volcanic plumes*. Wiley.

[111] Sparks, R. S. J., Self, S., & Walker, G. P. (1973). Products of ignimbrite eruptions. *Geology*, **1**(3), 115–118.

[112] Sparks, R. S. J., & Walker, G. P. (1973). The ground surge deposit: A third type of pyroclastic rock. *Nature*, **241**(107), 62–64.

[113] Sparks, R. S. J., & Walker, G. P. (1977). The significance of vitric-enriched air-fall ashes associated with crystal-enriched ignimbrites. *J. Volcanol. Geotherm. Res.*, **2**(4), 329–341.

[114] Staron, L., & Phillips, J. (2014). Segregation time-scale in bi-disperse granular flows. *Phys. Fluids*, **26**(3), 033302.

[115] Sulpizio, R., Dellino, P., Doronzo, D., & Sarocchi, D. (2014). Pyroclastic density currents: State of the art and perspectives. *J. Volcanol. Geotherm. Res.*, **283**, 36–65.

[116] Suzuki, Y. J., Costa, A., & Koyaguchi, T. (2016). On the relationship between eruption intensity and volcanic plume height: Insights from three-dimensional numerical simulations. *J. Volcanol. Geotherm. Res.*, **326**, 120–126.

[117] Suzuki, Y. J., Koyaguchi, T., Ogawa, M., & Hachisu, I. (2005). A numerical study of turbulent mixing in eruption clouds using a three-dimensional fluid dynamics model. *J. Geophys. Res.*, **110**, B08201.

[118] Thomas, D. G. (1965). Transport characteristics of suspension: VIII. A note on the viscosity of newtonian suspensions of uniform spherical particles. *J. Colloid. Sci.*, **20**(3), 267–277.

[119] Toro, E. F. (2001). *Shock-capturing methods for free-surface shallow flows*. Wiley.

[120] Trolese, M., Giordano, G., Cifelli, F., Winkler, A., & Mattei, M. (2017). Forced transport of thermal energy in magmatic and phreatomagmatic large volume ignimbrites: Paleomagnetic evidence from the Colli Albani volcano, Italy. *Earth Planet. Sci. Lett.*, **478**, 179–191.

[121] Ungarish, M. (2007). A shallow-water model for high-reynolds-number gravity currents for a wide range of density differences and fractional depths. *J. Fluid Mech.*, **579**, 373–382.

[122] Ungarish, M. (2009). *An introduction to gravity currents and intrusions*. CRC Press.

[123] Valentine, G. A. (1987). Stratified flow in pyroclastic surges. *Bull. Volcanol.*, **49**(4), 616–630.

[124] Valentine, G. A., Buesch, D. C., & Fisher, R. V. (1990). Reply to Wilson and Self's comments on: Basal layered deposits of the Peach Springs Tuff, northwestern Arizona, USA. *Bull. Volcanol.*, **52**(7), 565–569.

[125] Valentine, G. A., & Fisher, R. V. (1986). Origin of layer 1 deposits in ignimbrites. *Geology*, **14**(2), 146–148.

[126] Voight, B., & Davis, M. (2000). Emplacement temperatures of the November 22, 1994 nuée ardente deposits, Merapi Volcano, Java. *J. Volcanol. Geotherm. Res.*, **100**(1), 371–377.

[127] Walker, G. P. (1983). Ignimbrite types and ignimbrite problems. *J. Volcanol. Geotherm. Res.*, **17**(1–4), 65–88.

[128] Walker, G. P. (1985). Origin of coarse lithic breccias near ignimbrite source vents. *J. Volcanol. Geotherm. Res.*, **25**(1–2), 157–171.

[129] Walker, G. P., Self, S., & Froggatt, P. (1981). The ground layer of the Taupo ignimbrite: A striking example of sedimentation from a pyroclastic flow. *J. Volcanol. Geotherm. Res.*, **10**(1–3), 1–11.

[130] Walker, G. P., Wilson, C., & Froggatt, P. (1980). Fines-depleted ignimbrite in New Zealand—The product of a turbulent pyroclastic flow. *Geology*, **8**(5), 245–249.

[131] Walker, G. P., Wilson, C., & Froggatt, P. (1981). An ignimbrite veneer deposit: The trail-marker of a pyroclastic flow. *J. Volcanol. Geotherm. Res.*, **9**(4), 409–421.

[132] Wilson, C. (1980). The role of fluidization in the emplacement of pyroclastic claws: An experimental approach. *J. Volcanol. Geotherm. Res.*, **8**(2–4), 231–249.

[133] Wilson, C. (1985). The Taupo eruption, New Zealand. II. The Taupo ignimbrite. *Philos. Trans. R. Soc. Lond. Ser.A, Math. Phys. Sci.*, **314**(1529), 229–310.

[134] Wilson, C. (1986). Pyroclastic flows and ignimbrites. *Sci. Prog. Oxf.*, **70**, 172–201.

[135] Wilson, C. (1997). Scientific correspondence regarding Dade and Huppert (1996). *Nature*, **385**, 306–308.

[136] Wilson, C., & Walker, G. P. (1982). Ignimbrite depositional facies: The anatomy of a pyroclastic flow. *J. Geol. Soc. Lond.*, **139**(5), 581–592.

[137] Wilson, C., & Walker, G. P. (1985). The Taupo eruption, New Zealand. I. General aspects. *Philos. Trans. R. Soc. Lond. Ser.A, Math. Phys. Sci.*, **314**(1529), 199–228.

[138] Wilson, C., & Walker, G. P. (1981). Violence in pyroclastic flow eruptions. *Tephra studies*, Springer, pp. 441–448.

[139] Wohletz, K. H., & Sheridan, M. F. (1979). A model of pyroclastic surge. *Geol. Soc. Am. Spec. Pap.*, **180**, 177–194.

[140] Wohletz, K., McGetchin, T., Sandford, M., & Jones, E. (1984). Hydrodynamic aspects of caldera-forming eruptions: Numerical models. *J. Geophys. Res.*, **89**(B10), 8269–8285.

[141] Woods, A. W., & Bursik, M. I. (1991). Particle fallout, thermal disequilibrium and volcanic plumes. *Bull. Volcanol.*, **53**(7), 559–570.

[142] Woods, A. W., & Kienle, J. (1994). The dynamics and thermodynamics of volcanic clouds: Theory and observations from the April 15 and April 21, 1990 eruptions of Redoubt Volcano, Alaska. *J. Volcanol. Geotherm. Res.*, **62**(1–4), 273–299.

[143] Wright, J. V., & Walker, G. P. (1981). Eruption, transport and deposition of ignimbrite: A case study from Mexico. *J. Volcanol. Geotherm. Res.*, **9**(2–3), 111–131.